Towards Structural Health Monitoring of Gossamer Structures Using Conductive Polymer Nanocomposite Sensors

Mohammed Rabius Sunny

Dissertation submitted to the Faculty of the

Virginia Polytechnic Institute and State University

in partial fulfillment of the requirements for the degree of

Doctor of Philosophy

in

Aerospace Engineering

Rakesh K. Kapania, Ph.D., Chair

Mayuresh J. Patil, Ph.D.

Michael K. Philen, Ph.D.

Romesh C. Batra, Ph.D.

Jeffrey T. Borggaard, Ph.D.

June 25, 2010

Blacksburg, Virginia

(ABSTRACT)

The aim of this research is to calibrate conductive polymer nanocomposite materials for large strain sensing and develop a structural health monitoring algorithm for gossamer structures by using nanocomposites as strain sensors. Any health monitoring system works on the principle of sensing the response (strain, acceleration etc.) of the structure to an external excitation and analyzing the response to find out the location and the extent of the damage in the structure. A sensor network, a mathematical model of the structure, and a damage detection algorithm are necessary components of a structural health monitoring system. In normal operating conditions, a gossamer structure can experience normal strain as high as 50%. But presently available sensors can measure strain up to 10% only, as traditional strain sensor materials do not show low elastic modulus and high electrical conductivity simultaneously. Conductive polymer nanocomposite which can be stretched like rubber (up to 200%) and has high electrical conductivity (sheet resistance 100 Ohm/sq.) can be a possible large strain sensor material. But these materials show hysteresis and relaxation in the variation of electrical properties with mechanical strain. It makes the calibration of these materials difficult. We have carried out experiments on conductive polymer nanocomposite sensors to study the variation of electrical resistance with time dependent strain. Two mathematical models, based on the modified fractional calculus and the Preisach approaches, have been developed to model the variation of electrical resistance with strain in a conductive polymer. After that, a compensator based on a modified Preisach model has been developed. The compensator removes the effect of hysteresis and relaxation from the output (electrical resistance) obtained from the conductive polymer nanocomposite sensor. This helps in calibrating the material for its use in large strain sensing. Efficiency of

both the mathematical models and the compensator has been shown by comparison of their results with the experimental data. A prestressed square membrane has been considered as an example structure for structural health monitoring. Finite element analysis using ABAQUS has been carried out to determine the response of the membrane to an uniform transverse dynamic pressure for different damage conditions. A neuro-fuzzy system has been designed to solve the inverse problem of detecting damages in the structure from the strain history sensed at different points of the structure by a sensor that may have a significant hysteresis. Damage feature index vector determined by wavelet analysis of the strain history at different points of the structure are taken by the neuro-fuzzy system as input. The neuro-fuzzy system detects the location and extent of the damage from the damage feature index vector by using some fuzzy rules. Rules associated with the fuzzy system are determined by a neural network training algorithm using a training dataset, containing a set of known input and output (damage feature index vectors, location and extent of damage for different damage conditions). This model is validated by using the sets of input-output other than those which were used to train the neural network.

ACKNOWLEDGEMENT

I would like to express my deepest gratitude to my advisor Prof. Rakesh K. Kapania. The role of his help and guidance is beyond any measure. His invaluable advice always helped me in finding out solutions of any problem I encountered while carrying out my research. He has always been a source of inspiration for me. In my professional life, his contribution is immeasurable.

Sincere gratitude is extended to my committee members Prof. Michale K. Philen, Prof. Mayuresh J. Patil, Prof. Romesh C. Batra and Prof. Jeffrey T. Borggaard. Value of the time and effort expended by each member is immeasurable. I am very thankful to Prof. Cornel Sultan for serving as the examiner during my PhD preliminary examination. Sincere gratitude goes to Prof. Roop Mahajan, Director of the Institute for Critical Technology and Applied Science at Virginia Tech for funding our research.

I am thankful to my colleagues Pankaj Joshi, Raymond Singh, Wesley Slemp, Jason Twedt, Karen Scott, Dr. Sameer Mulani with whom I used to meet frequently for interaction both at professional and personal level. It was very nice to have such a close and wonderful research group.

I am very indebted to my friends Kaushik Das, Naresh K. Budhavaram, Prathyusha Kolkonda,

Pranitha Parimi, Abhranil Maiti, Chaitanya Chopra, Vedvyas Duggirala, Sachi Chander Nekkanti, Jaydeep Chawdhury, Sharmistha Mitra, and Neeta Jain. Most of them were my colleagues at Association for India's Development (AID), Blacksburg, a student organization which I have been serving for the last four years. Apart from our weekly AID meetings, we used to get together to go for dinner, play tennis etc. This made my stay at Blacksburg very enjoyable. I met Ms. Alice Rennals in a gathering of international students at Squires Students Center at Virginia Tech. I am very grateful to her for her affection and care for last four years.

I would like to express sincere gratitude to my sister-in-law Deena Khan, brother-in-law Syed Makhmour Mazahir and niece Sarah Syed at Blacksburg for their love and affection.

This journey would not have been completed without constant support from my family members. I owe special gratitude to my father Abdus Sattar, mother Ruba Begam, younger brother Mohammed Mehboob Rabbani in India for their unconditional love, support and encouragement throughout my life. I got married to my wife Tila Khan, a PhD candidate in the department of Department of Biomedical Sciences and Pathobiology at Virginia Tech, in July, 2009. I am truly blessed with her love, support and care.

This dissertation is dedicated to my grand parents Late Khalil Ahmed, Sirin Ahmed, Late Abdul Mannan, Late Saira Khatun, Abdus Salam and Karima Salam for their sacrifices throughout their life which has a very big role in making this journey possible.

Contents

1 Introduction **1**

1.1 Gossamer Structures 1

1.2 Large Strain Sensor 2

1.3 Mathematical Models for Hysteresis and Relaxation 4

1.4 Compensation of Hysteresis and Relaxation 7

1.5 Damage Detection in Structures 9

1.6 Overview of the Present Research 16

2 Strain-Resistance Experimental Data **19**

2.1 Observations 20

3 Fractional Calculus Modeling **26**

3.1 Fractional Calculus Operators and Their Properties 26

3.2 Development of Fractional Calculus Model 30

3.2.1 Model-1: (Combined Fractional Derivative and Integer Order Integral Model) . . . 31

3.2.2 Model-2: (Fractional Integral Model) . . . 33

3.3 Results From Error-Minimization . . . 35

3.4 Discussion . . . 35

4 Preisach Model **44**

4.1 The Preisach Model . . . 44

4.1.1 Modification of the Hysteresis Operator . . . 47

4.1.2 Addition of a Dynamic Operator . . . 51

4.2 Identification of Parameters . . . 53

4.3 Results and Discussion . . . 55

5 Compensator for Sensor Hysteresis and Relaxation **63**

5.1 Everett Integral and Everett Surface . . . 64

5.2 Everett Surface Using Both Modified Presiach Hysteresis Operator and Dynamic Relaxation Operator . . . 66

5.3 Forward Calculation Using Everett Surface . . . 68

5.4 Compensation . . . 70

5.5 Results and Discussion . . . 71

6 Neuro-fuzzy System **73**

6.1 Fuzzy Logic System 74

6.1.1 Fuzzy Set 74

6.1.2 Membership Function 74

6.1.3 Fuzzy Rules 75

6.1.4 Defuzzification 77

6.1.5 Structure of a Fuzzy Logic System 78

6.2 Artificial Neural Networks 78

6.2.1 Structure of a Neural Network 79

6.2.2 Training of Neural Network 80

6.3 Neuro-fuzzy System 82

7 Damage Detection in a Prestressed Membrane Using a Neuro-Fuzzy System **86**

7.1 Description of the Structure 87

7.2 Finite Element Analysis of the Structure 87

7.3 Results of the Finite Element Analysis 90

7.4 Wavelet Based Damage Feature Index 91

7.4.1 Wavelets 93

7.4.2 Continuous wavelet transform 94

7.4.3 Wavelet Packet Analysis 94

7.4.4 Definition of a Damage Feature Index 96

7.5 Input and Output 97

7.6 Implementation of the Neuro-fuzzy System 101

7.7 Results and Discussion 103

8 Summary and Conclusions **115**

List of Figures

1.1 Gossamer Structures 3

1.2 Schematic View of the Proposed Health Monitoring System for Gossamer Structures 18

2.1 Experimental Setup for Dataset-1 and Dataset-2 21

2.2 Experimental Setup for Dataset-3 22

2.3 Applied Strain 23

2.4 Resistance vs. Strain (Dataset-1) 24

2.5 Resistance vs. Time (Dataset-1) 24

2.6 Resistance vs. Strain (Dataset-2) 25

2.7 Resistance vs. Strain (Dataset-3) 25

3.1 Derivative and Integral of Order 0.5 29

3.2 Resistance vs. Strain for Dataset-1 37

3.3 Resistance vs. Time for Dataset-1 38

3.4 Resistance vs. Strain for Dataset-2 39

3.5 Resistance vs. Strain for Dataset-3 40

4.1 Hysteresis Operator ($\gamma_{\alpha,\beta}(u)$) in Preisach model 47

4.2 Preisach-Mayergoyz Space at Different Stages of the First Cycle 48

4.3 Variation of Output with Input at Different Stages of the First Cycle 49

4.4 Proposed Modified Hysteresis Operator 52

4.5 Preisach-Mayergoyz Space at Different Stages of the First Cycle 57

4.6 Variation of Output with Input at Different Stages of the First Cycle 58

4.7 PM Space Divided into Bins 59

4.8 Comparison of the Results from the Model with the Experimental Result (Dataset-1) 60

4.9 Comparison of the Results from the Model with the Experimental Result (Dataset-2) 61

4.10 Comparison of the Results from the Model with the Experimental Result (Dataset-3) 62

5.1 Variation of Input with Time 65

5.2 PM Space at Different Time Instants 66

5.3 Everett Surface 67

5.4 Cyclic Input and Residual Part of Output After Compensating for the Relaxation 69

5.5 Comparison of the Results Obtained from Mathematical Model with the Experimental Data 71

6.1 Fuzzy Sets and Membership Functions 75

6.2 Degree of Similarity Vs. Distance 77

6.3 Structure of a Fuzzy Logic System 79

6.4 Structure of a Single Layered Neural Network 81

6.5 Neurofuzzy System 84

7.1 Prestressed Membrane Under Study 88

7.2 16 Zones in the Prestressed Membrane 89

7.3 Finite Element Meshes for the Prestressed Membrane 89

7.4 Variation of the Transverse Displacement at (0.3m, 0.3m) in the Membrane with 40% Damage at Zone-1 91

7.5 Variation of the Transverse Displacement at (0.3m, 0.3m) in the Membrane with 40% Damage at Zone-1 92

7.6 Variation of the Normal Strain Along the Y Direction at (0.3m, 0.3m) in the Undamaged Membrane 92

7.7 Wavelet Packet Tree 96

7.8 Haar Wavelet 99

7.9 Scaling function for the 'Haar' Wavelet 100

7.10 Multiresolution Analysis of the Strain History at (0.2m, 0.2m) in the Damaged Membrane 101

7.11 Multiresolution Analysis of the Strain History at (0.2m, 0.2m) in the Undamaged Membrane 102

7.12 Sensor Locations and Damage Zones in the Membrane 103

7.13 Fuzzy Sets for Damage 104

7.14 A Neurofuzzy System 105

7.15 Comparison of Predicted Damage with Actual Damage Obtained After First Training Without Noise 106

7.16 Comparison of Predicted Damage with Actual Damage Obtained After First Training With Noise 107

7.17 Comparison of Predicted Damage with Actual Damage Obtained After Second Training Without Noise 108

7.18 Comparison of Predicted Damage with Actual Damage Obtained After Second Training With Noise 109

List of Tables

3.1 Values of the Parameters and Errors in Different Models (N=3, M=6) 41

3.2 Values of the Parameters and Errors in Different Models (N=5, M=8) 42

4.1 Error and CPU Time Corresponding to Different Values of M and P 55

7.1 Comparison of Predicted Damage with Actual Damage Obtained After First Training Without Noise 110

7.2 Comparison of Predicted Damage with Actual Damage Obtained After First Training With Noise 111

7.3 Damage Cases in the Reference Set for Second Training 112

7.4 Comparison of Predicted Damage with Actual Damage Obtained After Second Training Without Noise 113

7.5 Comparison of Predicted Damage with Actual Damage Obtained After Second Training With Noise 114

Chapter 1

Introduction

1.1 Gossamer Structures

Gossamer structures refer to inflatables or any other ultra light weight structures. Examples include solar arrays, inflatable space antennas, space habitats etc. Highly flexible membrane or shell-like elements are main components of such structures. The US National Aeronautics and Space Administration (NASA) launched its first expandable satellite ECHO in 1998. NASA began to look at inflatable structures to house astronauts in transit to Mars as well as a habitat once they were on the surface. In 2006 Bigelow Aerospace launched a subscale inflatable demonstrator called Genesis I. Figure 1.1a shows an inflatable Mars rover solar array prototype developed by ILC Dover for the Jet Propulsion laboratory (JPL). This solar array prototype is a working, full scale inflatable solar array for rover application [1]. An ultra light weight space habitat TransHab developed by NASA to support a six members crew for a long duration stay in space is shown in Fig. 1.1c. Outer part of the structure

is made of multi-layered shell. Inflation by air or a gas causes a pre-tension in inflatable structures and keeps them in the desired shape and stiffness. In case of other membrane type structures, the pretension is applied by pulling the structure at some strategic points. The roof of the Denver international airport is an example of such structures. The main advantage associated with the gossamer structures is their high strength and stiffness to mass ratios. These structures have a minimal need for on site construction materials. Virtually all of the assembly mechanism is inherent to the structure [1].

One of the major problems with gossamer structures is their vulnerability to structural damages such as cracks, wrinkles (in case of single thin walled structures) and delaminations (in case of multi-layered walls) etc. affecting their serviceability and safety. This necessitates the development of an efficient structural health monitoring system for such structures.

1.2 Large Strain Sensor

In normal operating conditions, a ultra light weight, highly flexible structure can experience normal strain as high as 50%. But presently available sensors can measure strain upto 10% only. Standard foil resistive gage can measure strain of up to 2.5% or less. Strain sensors made of the piezoceramic material, lead zirconium titanate(PZT) can measure up to $1-2\%$. Polyvinylidene fluoride (PVDF) is a relatively flexible material with piezoelectric properties. It can be used to measure strain up to 10%. Conductive polymer nanocomposite materials have low elastic modulus (10MPa), high electric conductivity (sheet resistance is 0.1 to 1 $/sq.$) and can be stretched up to 200%. A review on sensors for gossamer structures can be found in [2]. Calibration of conductive polymer nanocomposite materials as a large

(a) Solar Array Prototype

(b) Inflatable Space Antenna

(c) Inflatable Space Habitat

Figure 1.1: Gossamer Structures

strain sensor is one of the goals of our research. But phenomena of both the hysteresis and relaxation in the variation of electrical resistance with strain in these materials posses a significant challenge in the calibration of these materials.

1.3 Mathematical Models for Hysteresis and Relaxation

Hysteresis represents a property of systems that show dependence on input history applied to it *i.e.* output at any time instant depends on the input applied to the system both at the present time as well as the previous history; consequently same instantaneous value of the input can give different outputs depending on the entire input history. Variation of the output with cyclic input in a system with hysteresis gives rise to a loop, called 'hysteresis loop'. Hysteretic phenomena are encountered in various branches of engineering, such as magnetic hysteresis, electrical hysteresis, ferroelectric hysteresis, electron beam hysteresis, adsorption hysteresis etc. Viscoelastic behavior of composite laminates [3, 4] and rheological behavior of polymers [5] are other well known examples of hysteretic behavior. Some studies on unsteady behavior of conductive polymers can be found in [6, 7, 8]. Knite et al. [7] investigated the use of electrically conductive polymer composites as large-size flexible pressure and stretch sensors for detecting dangerous deformations and vibrations of vehicle components. They studied the change of resistance with strain at different concentrations of carbon nano-particles in the conductive polymer composites and proposed a description of the microstructure providing extremely strong tenso-resistive and piezo-resistive effects. Rekhviashvili [8] developed an elementary theory of electrical conduction using the fractional equation of motion. It was shown that current fluctuations in a polymer have a spectral characteristic of the flicker type.

Different mathematical models have been developed, depending on the type of hysteretic behavior, and successfully applied in these fields. Hysteresis models are either physics

based or empirical. Physics based models, being mainly microscopic and semi-microscopic, involve application of an energy principle and thermodynamic, electromagnetic or other laws depending on the behavior at the grain level [9]. The main disadvantage of such models is the requirement of a large number of material parameters. As our goal was to develop a mathematical model for the calibration of large strain sensor, we were more interested in empirical models that require less number of parameters and are suitable for practical applications, such as structural health monitoring of gossamer structures. We first reviewed in detail two of the several existing hysteresis models, namely the Preisach and the fractional calculus approaches.

Fractional derivatives were first discussed in 1695 by l'Hospital in a letter to Leibniz [10, 11]. Later on, researchers including Euler [12], Lacroix [13], Hardy [14], and Osler [15] made significant contributions to the theory of fractional calculus. This approach has proven to be very effective in modeling the dynamic behavior of different kinds, especially of viscoelastic materials showing hysteresis coupled with relaxation. Nutting [16] observed that stress relaxation could be modeled by fractional powers of time. This can be viewed as the progenitor of the fractional calculus approach of modeling the viscoelastic behavior [17]. Gemat's [18] observation on stiffness and damping properties of viscoelastic materials to be proportional to the fractional powers of frequency was another motivating factor behind this.

The basic principle behind this type of modeling is to express the relation of time dependent output with the time dependent input by an equation involving fractional differential and integral operators. By minimizing the sum of the square of difference between the output obtained from the experiment and the output predicted by the model at the data points, the

values of different parameters (order of derivatives, integrals, coefficients multiplied with the derivatives and integrals) are determined. Scott-Blair and Reiner [19], Belavine *et al.* [20] applied fractional derivatives in the field of rheology and electro-chemistry, respectively. Bagley and Torvik [21, 22] showed the use of fractional derivatives to model viscoelastic behavior. Thermodynamic constraints, based on a nonnegative rate of energy dissipation and nonnegative internal work were used for the selection of material parameters. They claimed that mathematical models obtained by following this approach are accurate over several decades of material property values. de Espindola, da Silva and Lopes [23] proposed a model based on 4 unknowns in the fractional differential equation to identify different mechanical properties of a viscoelastic material. They defined a complex transmissibility function in the frequency domain. Unknown material parameters were determined by minimizing the sum of the square of the values of transmissibility at different frequencies. Horr and Schmidt [24] modeled frequency dependent damping characteristics of viscoelastic material using fractional derivatives. Davis *et al.* [25] used fractional derivative to determine constitutive properties of brain parenchyma. They used fractional Zener model with four unknowns and obtained relaxation and creep properties of the material.

Preisach [26] in 1935 developed the well-known model to represent path-dependent behavior of magnetic materials based on some plausible hypothesis concerning the physical mechanisms of magnetism. In this model, the output from a system with hysteresis is considered as a weighted combination of the outputs from a number of elementary hysteresis operators. Everett and Whitton [27] independently invented and developed the model for adsorption hysteresis. Later on, several modifications have been proposed to take care of the dependence of the output on the rate of the input, stabilization of the hysteresis loop etc. Cornejo

and Missell [28] used Preisach model to model nanocrystalline magnets. Roshko and Huo [29] characterized the irreversible response of a ferromagnet pervoskite ($SrRuO_3$) with a Curie temperature of 160K. Vandenbossche, Dupr and Melkebeek [30] investigated the application of magnetic hysteresis measurement combined with the Preisach model for the evaluation of fatigue damage progression. Determination of the weight function and very high computation time are major problems in using Preisach model [31]. Schiffer and Ivanyi [31] showed the use of wavelets to solve these problems. The weight functions were derived for some operators and two-dimensional wavelet average interpolation transform was applied to interpolate the function for other operators. Yunhe *et al.* [32] represented system outputs and Preisach function by wavelet approximation. A dynamic rate-dependent Preisach model can be found in the book by Mayergoyz [33].

1.4 Compensation of Hysteresis and Relaxation

A system Γ_2 is called the compensator (or inverse) of a system Γ_1 if, for any initial state of the system Γ_1, there is a state of the system Γ_2 such that, starting from these states, the series connection of the two systems gives the identity transformation independent of their order [34]. In case of a sensor with nonlinearities, a compensator is placed in series with the sensor to remove the effect of nonlinearities present in the sensor from the sensed data to facilitate its calibration.

Everett integral and Everett surface based algorithms, as discussed in Chapter 7 subsequently, are very common among the different compensation algorithms for Preisach hysteresis. Natalea, Velardib and Visonec [34] proposed identification and compensation of

the hysteretic behavior of a Terfenol-D magnetostrictive actuator. Everett integrals and the Preisach distribution function were analytically reconstructed by using both a fuzzy approximator and a feed-forward neural network. Due to the filtering capabilities of the neuro-fuzzy interpolators smoothing of the measured data was not required. Using the Everett integrals and the Preisach distribution function, hysteresis compensator was developed. Davino *et al.* [36] proposed an Everett surface based fast compensation algorithm for real time control of magnetostrictive actuators. They provided the Everett function through a matrix, implementing its uniformly spaced samples. The problem of finding the value of input from the output was solved simply by inspecting a lookup table according to some rules that were presented in their paper. Cavallo *et al.* [37] generalized the approach of Davino *et al.* [36] to develop the compensator for systems where output depends on more than one input variable. For example, in micro-positioning tasks using ferro-magnetic materials, output force can be a function of magnetic field and the pre-stress.

Galinaitis and Rogers *et al.* [38] proposed a bivariate Preisach model for compensation of hysteresis. Their model was based upon the idea of finding a Preisach distribution function for which a closed-form formula for the inverse operator can be obtained. They proposed two easily invertible models. The first model treats the Preisach distribution to be a function of two variables. This function has a value zero outside of the second quadrant of the Preisach plane which causes the loops to exhibit a pronounced saturation effect. The second model considers the Preisach distribution to be a function with one free variable. This model shows comparatively less saturation effect. After that, they derived the Preisach distribution functions which give the inverse of the above two models. Tan, Venkataraman and Krishnaprasad [39] proposed a closest match algorithm for hysteresis compensation. In

this method, the Preisach plane is discretized into a finite number of grids. The algorithm aims to determine the input whose output matches the desired output most closely among all possible inputs. Since the Preisach plane is discretized, the input can only take values from a finite set. Viswamurthy and Ganguli [9] used the closest match algorithm for hysteresis compensation in a piezoelectric actuator for helicopter vibration control.

Most of the presently available compensators are based on classical Preisach model and they are effective in time independent static hysteresis. Research on a compensator for piezoelectric actuators with consideration to both time independent hysteresis and time dependent creep can be found in the works by Janocha *et al.* [40], Changhai *et al.* [41]. But literature on compensation of dynamic hysteresis is rather weak to the best of our knowledge.

1.5 Damage Detection in Structures

Structural health monitoring systems are developed to detect damages in a structure in a non destructive way. In a structural health monitoring system, response of the structure to an external excitation is analyzed to detect the damages. Vibration based methods, ultrasonic technique, acoustic emission method etc. are different techniques used in structural health monitoring. Vibration based techniques use frequencies, mode shapes, frequency response functions (FRF) as indicator of damage.

In wave mechanics based approach to structural health monitoring, the structure is given a high frequency excitation by vibration of ultrasonic wave. When a propagating wave encounters a crack, delamination or any other type of discontinuity, a part of the wave is

reflected and a part of the wave is transmitted by the crack. This results in a difference in the response (strain history, acceleration history etc.) of the damaged structure from that of a healthy structure. So, the response of the structure is used for damage detection. Acoustic emission, another such technique, is based on the principle of sensing the stress wave emitted due to the propagation of a crack. Developing a good correlation between the response of the structure and the damage status is very important for health monitoring. So, a mathematical model is built to simulate the behavior of the structure. The simulation is run for different damage conditions of the structure. Response of the structure with different types of damage obtained from the simulation is used to relate the damage status with the response of the structure using different pattern recognition techniques.

One core issue of the global vibration based damage assessment methods is to seek some damage indices that are sensitive to structural damage [42]. Mode shape and mode shape curvatures were previously used by many researchers as damage indices [43, 44, 45]. Requirement of a large number of sensors for accurate determination of the mode shapes is one of the major disadvantages associated with the mode shape based methods. According to Farrar and Jauregui [46, 47], standard modal parameters such as natural frequencies and mode shapes are poor indicators of damage and have higher statistical variability. Many existing vibration based approaches for damage detection require the modal properties with the aid of the traditional Fourier transform [48]. Researchers including Loewke *et. al.* [49], Raghavan and Cesnik [50] and Pawar, Reddy and Ganguli [51] have successfully used Fourier transform for structural damage detection. However, there are a few inherent characteristics of the Fourier transform that might affect the accuracy of damage identification. Fourier transform is a data reduction process which sometimes leads to the loss of damage

information. Damage is typically a local phenomenon which tends to be captured by higher frequency modes. These higher frequencies normally are closely spaced but poorly excited. All these factors add difficulty to the implementation of the Fourier transform-based damage detection techniques [48, 42].

Recently, researchers have shown great interest in using the wavelet decomposition of structural response for damage detection. Wavelets were first applied in geophysics to analyze data from seismic surveys, which are used in oil and mineral exploration, to get pictures of layering in the surface rock [52]. In wavelet analysis, a signal is decomposed using shifted and scaled versions of a short duration wave, called the wavelet basis. Generally, the wavelet basis functions have highier energy density than the sinusoidal basis functions used in Fourier transform. Hence, wavelets require fewer coefficients than the sinusoidal basis functions in Fourier transform to describe a signal. The main advantage gained by using wavelets in signal analysis is the ability to perform local analysis of a signal, i.e. to zoom on any interval of time or space. Wavelet analysis is thus capable of revealing some hidden aspects of the data that other signal analysis techniques fail to detect. This property is particularly important for damage detection applications [42]. A possible drawback of the traditional wavelet transform is that the frequency resolution is quite poor in the high frequency region. Wavelet packet transform which is an extension of the wavelet transform makes it possible to combine the different levels of decomposition in order to achieve the optimum time-frequency representation of the original signal [42, 53].

Law *et. al.* [42] used a wavelet packet based sensitivity method to determine damage in simply supported concrete beam. Measured response signals (acceleration and strain histories) from the structure were first decomposed into wavelet packet components. Components

that contain much of the structural system information were identified, and their energy and sensitivity to local damage were calculated. The proposed method was also shown both analytically and numerically not to be sensitive to the measurement noise. Sun and Chang [48] used wavelet packet transform of the response (acceleration history) of a three span continuous bridge for damage detection. Measured acceleration signals were first decomposed into component signals using the wavelet packet transform. Selected component energies were used as inputs to an artificial neural network for damage assessment. The wavelet packet transform based component energies extracted were proven to be good indicators that can reveal the health of a structure.

Yam, Yan and Jiang [54] showed the use of wavelet packet transform in crack detection for polyvinyl chloride (PVC) sandwich plates. At first, the structural response (voltage in piezoelectric sensors) was decomposed into various components using the wavelet packet transform. Damage feature proxy vectors were defined using the ratios of the energies of the different response components in a damaged structure with those in an undamaged structure. Using the damage feature proxy vectors for different damage conditions, an artificial neural network was trained to detect damage from the damage feature proxy vectors of an structure with unknown damage status.

Soft computing methods like neural network, genetic algorithm, fuzzy logic system etc. are used for relating damage indices with the damage status of the structure. Artificial neural network is an information processing tool inspired by the structure of biological nervous systems. It is composed of a large number of interconnected processing elements. The neurons and the interconnections are associated with biases and weights. By using a set of input and output data the biases and weights in the neural network are adjusted to form a

map between input and output. This is called *training the network* and the set of input is called a *training set*. Advantages of this technique include self organization i.e. its ability to create its own organization or representation of the information received during learning, real time operation and the fact that some of the capabilities of the network are retained even with major network malfunction. Its disadvantages are that it requires a large amount of computer time for training and a slight tuning in the network is difficult when there are small modifications in the model.

Genetic algorithms are search algorithms developed using the principle of natural population genetics to evolve solutions to optimization problems. Genetic algorithm based damage detection algorithms works on the principle of minimizing the difference between the measurements obtained from analytical or numerical model and the experimental model. Genetic algorithms are time consuming. So, they are not suitable for online monitoring. Fuzzy logic systems address the uncertainties by linguistic reasoning. Fuzzy logic based structural health monitoring systems can be tuned using human experience based knowledge when sufficient data is not available. Fuzzy logic systems have a very simple mathematical concept. They can be developed even with a small number of data sets and have the advantage of adding more functionality without starting from scratch. However, fuzzy logic does not have the capability of learning from data and being a manual process, it is time consuming. Now-a-days researchers are developing different soft computing methods by hybridizing different techniques like fuzzy logic, genetic algorithm, neural network etc. to use the relative advantages of these techniques.

Kim and Kapania [55] showed the use of artificial neural network (ANN) to solve inverse problem in different engineering fields. Inverse problems investigated were damage detection

in structures, detection of an anomaly in light-weight diffusion medium, such as human tissue using optical imaging, and structural optimization of fiber optic sensor design. They used principal component analysis and orthogonal arrays to reduce the size of the input needed to train the neural network. Chakraborty [56] used ANN to determine the shape, size and location of delaminations in fiber reinforced plastic composite laminates. He used natural frequencies as the indicative parameter. Mahapatra *et al.* [57] proposed the use of a reduction-prediction network combined with an independent component analysis to quantify the damage due to transverse matrix cracking in multilayer composite laminate beam using an acoustic wave. They used a spectral finite element model for the beam. A micromechanics model for damage was incorporated in it. Spectral data generated by the model was used to train the network. Yam, Yan and Jiang [54] proposed a vibration response based approach using ANN for damage detection in composite structure. Vibration response of the structure was decomposed using wavelet packet analysis and a damage feature proxy was constructed using the wavelet packets. The damage feature proxy was used as indicative parameter.

Oberholster and Heyns [58] used ANN to develop an online health monitoring scheme for axial flow fan blades. Global blade mode shapes and their corresponding frequencies were identified using stationary experimental modal analysis. They showed the possibility of using classifying damage for several fan blades by using ANN with online vibration measurements from sensors not necessarily installed on the damaged blades themselves. Liang and Hwu [59] proposed an algorithm for online identification of holes and cracks in composite structures using ANN. Static strains were used as the indicative parameter. Rao, Srinivas and Murthy [60] used GA to determine the location and extent of damage in structure.

Dynamic residual vectors obtained by introducing a simulated experimental data into the eigenproblem were used to derive a global error. By using that error, the damage parameters were determined.

Nag, Mahapatra and Gopalakrishnan [61] proposed a GA based method for identification of delamination in composite structures. Response of the damaged structure in the frequency domain was calculated using a spectral finite element model. Sensitivities of the objective function with respect to different damage parameters was studied. Yang, Liu and Lam [62] used an integral strain measured by fiber optics for detection of three-dimensional crack in plates and shells. The square of the difference of the integral strain in a plate with an actual crack and in a plate with a trial crack was used as the objective function. By minimizing the objective function using micro GA, the location and the size of the crack were obtained. Sawyer and Rao [63] proposed a fuzzy logic based method for structural fault detection scheme. Structural response for different damage conditions were calculated using finite element method and the fuzzy association of the responses with the damage conditions were determined by supervised learning. They gave some numerical examples to show the advantage of using the fuzzy logic based system in noisy and uncertain conditions. Soh and Bhalla [64] proposed a fuzzy probability based damage model based on the extracted equivalent stiffness to evaluate the extent of damage using the impedance data. This enabled the calibration of the piezo-impedance transducers in terms of damage severity which could serve as a practical empirical phenomenological damage model for quantitatively estimating the damage severity in concrete.

Ramu and Johnson [65] integrated fuzzy logic system with artificial neural network for damage detection. The advantages of using this integrated method was that it needs no

additional efforts at the training level, but it can be used against fuzzy input by the end user with the integration of the vertex method module. Pawar and Ganguli [66] developed a genetic fuzzy system by hybridizing the best features of fuzzy logic and genetic algorithm to detect damage from noise contaminated measurements. Using the changes in structural measurements between the damaged and undamaged blade a fuzzy system was generated and the rule-base and membership functions were optimized by genetic algorithm. They showed that genetic fuzzy system (GFS) shows excellent robustness with noisy data, missing measurements and degrades gradually in the presence of faulty sensors/measurements. Furthermore, the GFS can be developed in an automated manner resulting in an optimal solution to the inverse problem of structural health monitoring.

1.6 Overview of the Present Research

This work is an investigation into the feasibility of developing a health monitoring system for gossamer structures using conductive polymer nanocomposites as strain sensors. Finding a large strain sensor is one of the major problems in structural health monitoring of gossamers structures as mentioned in Section 1.2. Conductive polymers having suitable electrical and mechanical properties can be a possible large strain sensor material. At first, we performed conductivity test on a conductive polymer sample to study its variation of electrical resistance with strain and observed the hysteresis and relaxation phenomena in it. The anti-clockwise hysteresis loop formed by the variation of electrical resistance with strain in our sample was found to move upward with number of cycles and to relax when the input strain is kept constant. The hysteresis loop depends on the rate of the application

also. Developing a proper mathematical model for this variation was necessary to calibrate conductive polymers as the sensor. But the fractional calculus approach in its traditional form did not lend its application to our data readily. We developed two models based on some modifications of fractional calculus approach. The existing rate-dependent Preisach model considers the relaxation parameters to be dependent upon the parameters controlling the static hysteresis. This increases computational complexity in the compensation of hysteresis and relaxation. Here, we proposed a modified dynamic Preisach model which considers the static hysteresis and relaxation to be independent phenomenon. After that a hysteresis compensator was developed by using the modified Preisach model to calibrate conductive polymers as a strain sensor. Next, we wanted to investigate the issues needed to be resolved before the application of this sensor for structural health monitoring of inflatable structures. We have taken a square prestressed membrane as an example structure. We carried out finite element analysis of the membrane using ABAQUS to find out its response to an uniform transverse dynamic pressure for different damage conditions.

Next, a neuro-fuzzy system was developed by hybridizing fuzzy logic with a neural network to detect the location and extent of damages in the structure from the strain history at a few selected points in the membrane. The neuro-fuzzy system uses some fuzzy rules to detect the damages in the structure from the damage feature proxies defined by using the strain history at different sensor locations. This model was validated by using an input-output dataset on which the system has not been trained. Practically, the output from the compensator can have high frequency noise of low magnitude, as the behavior of the sensor material may still have some uncertainty associated with it. Fuzzy logic based systems can account for these uncertainties by using linguistic reasoning, which is more robust to

uncertainty than pure numerical reasoning. Efficiency of this trained neuro-fuzzy system was checked by adding artificial noise to the simulated output of a structure with known damage status and using that noisy output for damage detection by the neuro-fuzzy system. Figure 1.2 shows the schematic view of our proposed health monitoring system.

Chapter 3 describes the experiment carried out in conductive polymer noanocomposites. Chapter 4 and Chapter 5 describe modified fractional calculus and modified Preisach approaches respectively to model the variation of electrical resistance with strain in conductive polymers. We propose a compensator based on the modified Preisach approach in Chapter 6. Chapter 7 proposes a neuro-fuzzy system. Chapter 8 shows the use of the neuro-fuzzy system in detecting the damages in a square membrane using the response obtained from the conductive polymer nanocomposite sensors fitted to the membrane.

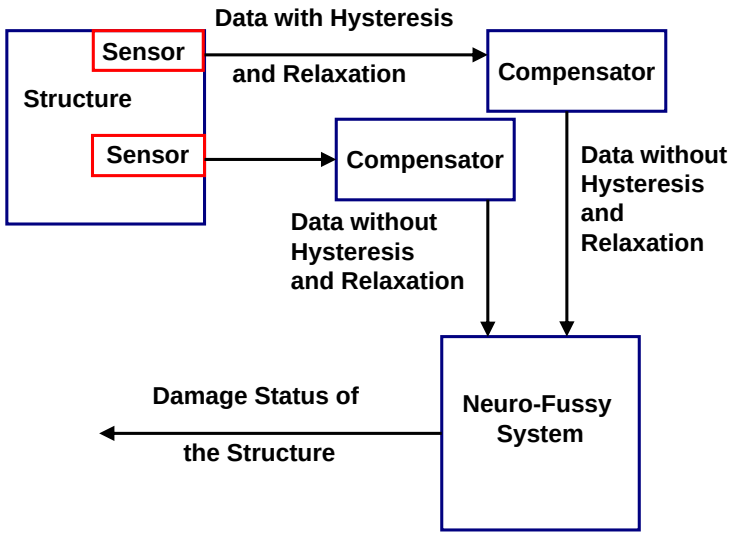

Figure 1.2: Schematic View of the Proposed Health Monitoring System for Gossamer Structures

Chapter 2

Strain-Resistance Experimental Data

Conductivity tests were carried out on a conductive polymer sensor to study the variation of its electrical resistance with strain. Experimental setup used for this test is shown in Fig. 2.1. For first two sets of experiments, a linear stage (NLS4-10-25 by Newmark Systems Inc.) was used to apply time dependent strain to the sensor. The top clamp of the linear stage is fixed. The bottom clamp can move and apply strain to the material at a desired rate. Movement of the bottom clamp can be controlled by 'IMS Lynx Terminal', a software provided by Intelligent Motion Systems Inc. This helps us to apply strain to the material at a desired rate. In the third set of experiments, a universal testing machine (eXpert 7603 by ADMET Inc.) was used instead of the linear stage. The universal testing machine has a fixed bottom clamp and movable top clamp (Fig. 2.2). The movement of the top clamp is controlled by MTESTQuattro, a software provided by ADMET Inc. The two ends of the sample close to the clamps are connected to a 46-range digital multi-meter with interface to a computer through serial port (RS-232). The multi-meter shows the resistance of the portion

of the material between the connected ends. Readings of the multi-meter are stored in a computer through a program 'Meterview 1.0', provided by Radioshack. Using this setup, a time dependent strain can be applied to the sample and its resistance can be measured at different time instants at different strain levels.

Time dependent cyclic strain input as shown in Fig. 2.3a with strain rate of $0.15\%/sec$ was applied to the system and time-dependent resistance was measured. Change in output resistance with input strain and time is shown in Fig. 2.4 and Fig. 2.5 respectively. Output obtained from the experiment contained high frequency noise which was removed by using a low-pass filter to smooth the experimentally obtained curve. In Fig. 2.4a and Fig. 2.5 unfiltered and smoothed (filtered) data have been presented. Smoothed data obtained after performing two sets of experiments has been shown to ensure the repeatability of the experiment. Smoothed data obtained from first experiment has been used later on for developing mathematical model. Let us term this dataset as Dataset-1. After this the material was allowed to relax and another experiment was performed by applying a strain as shown in Fig. 2.3b with a higher strain rate ($0.3\%/sec$). Results obtained from this experiment are shown in Fig. 2.6. Let us call it Dataset-2. Input strain applied in the third set of experiment is shown Fig. 2.3b. Fig. 2.7 shows the result obtained from this. Let us term it Dataset-3.

2.1 Observations

1. Figures 2.4, 2.6 and 2.7 show that electrical resistance when plotted against strain gives rise to an anti-clockwise hysteresis loop.

2. Width of the loop does not necessarily remain constant with number of cycles.

3. The loop moves upward with number of cycles.

4. The width of the hysteresis changes for same type of cyclic input with different strain rates.

5. Figure 2.4b shows that when the input is kept constant the value of resistance relaxes.

Conductivity test performed on conductive polymer nanocomposite sample has been described. Phenomena of hysteresis and relaxation in the variation of electrical resistance with strain has been observed. We have developed two mathematical models based on modified fractional calculus and modified Preisach approaches. These models will be described in the following two chapters.

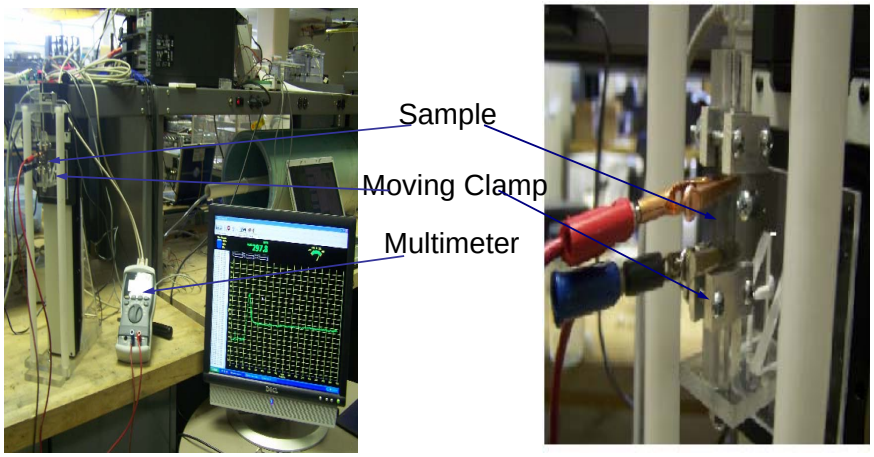

Figure 2.1: Experimental Setup for Dataset-1 and Dataset-2

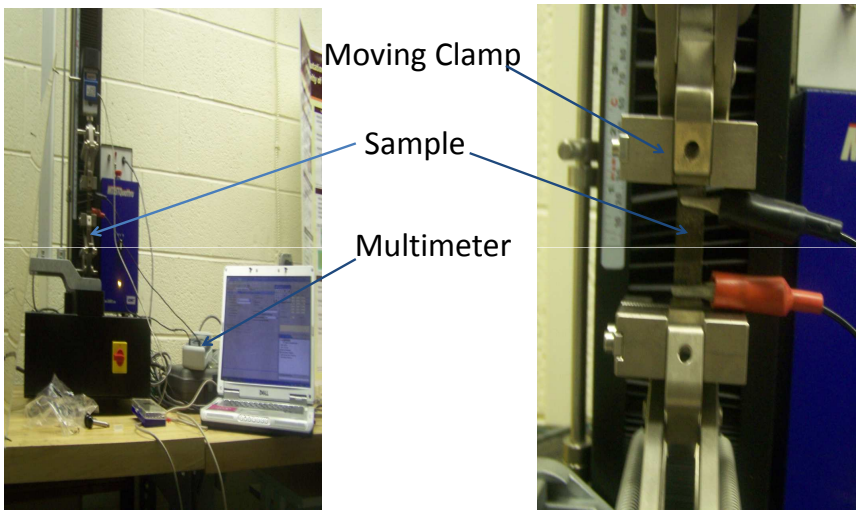

Figure 2.2: Experimental Setup for Dataset-3

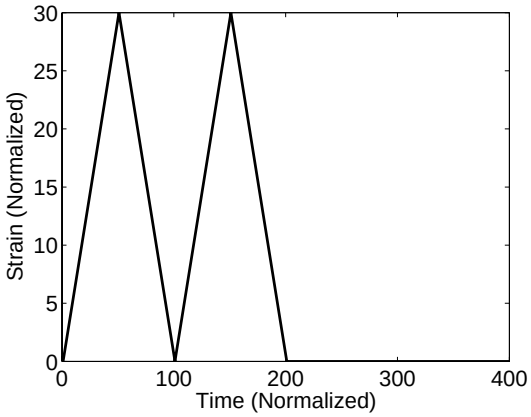

(a) Strain vs. Time (Dataset-1)

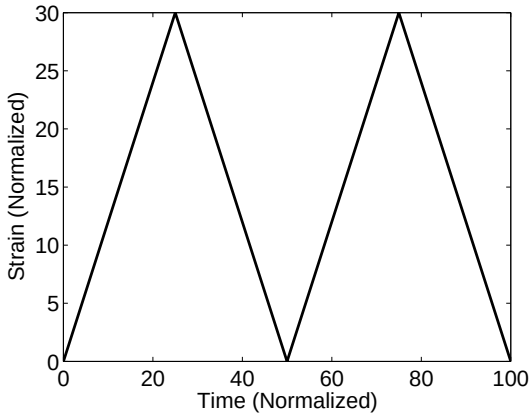

(b) Strain vs. Time (Dataset-2)

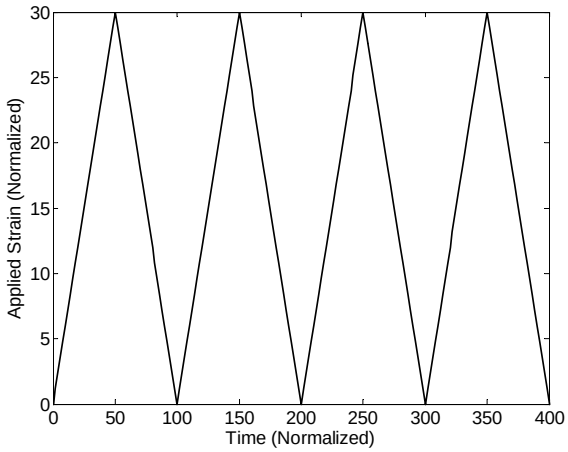

(c) Strain vs. Time (Dataset-2)

Figure 2.3: Applied Strain

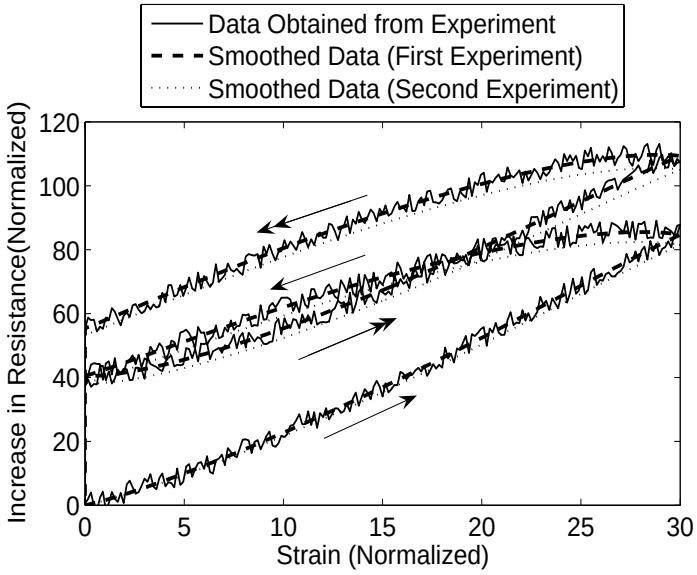

Figure 2.4: Resistance vs. Strain (Dataset-1)

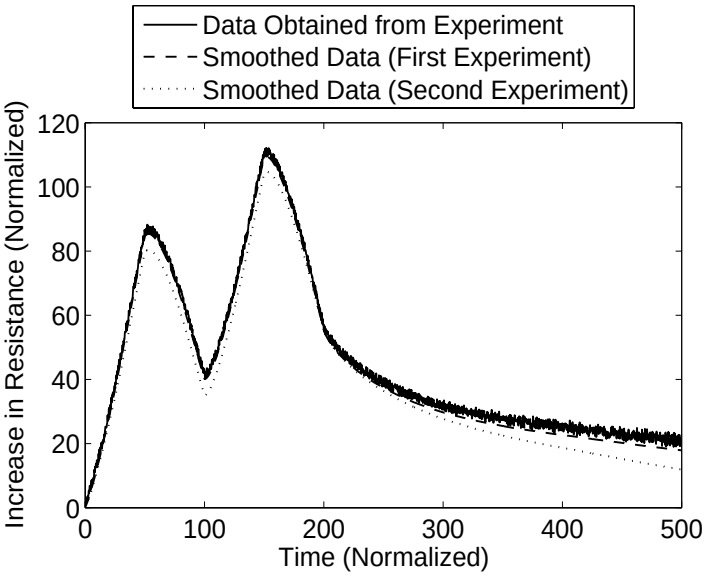

Figure 2.5: Resistance vs. Time (Dataset-1)

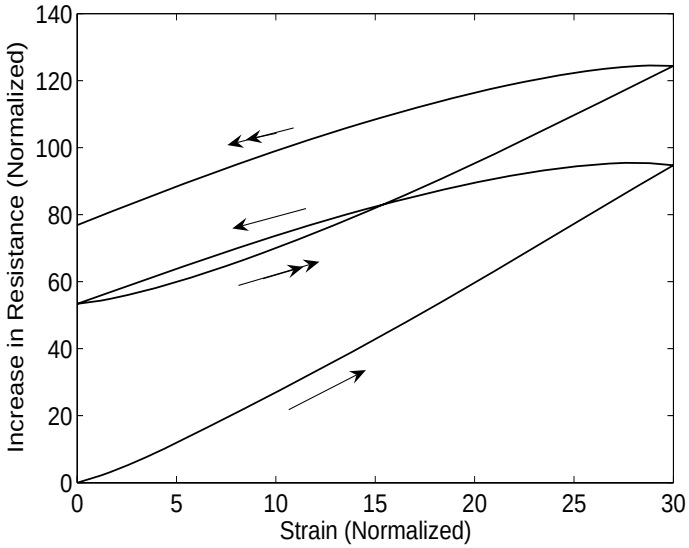

Figure 2.6: Resistance vs. Strain (Dataset-2)

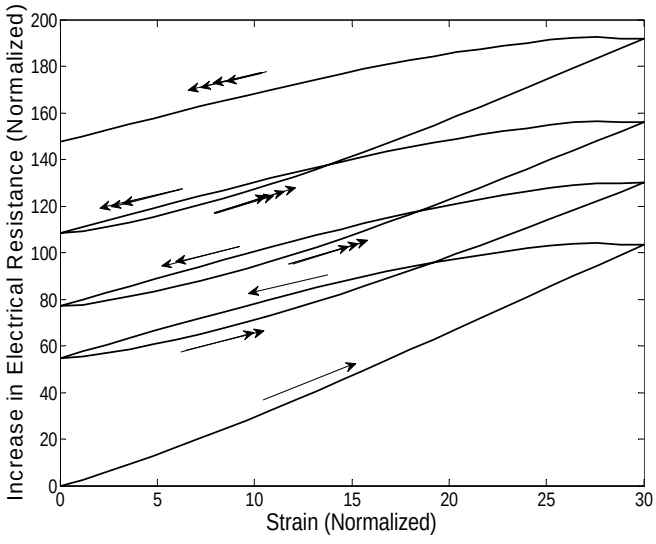

Figure 2.7: Resistance vs. Strain (Dataset-3)

Chapter 3

Fractional Calculus Modeling

This chapter proposes two mathematical models developed by some modifications made to the fractional calculus approach to model the variation of electrical resistance with strain in conductive polymer nanocomposites. A brief introduction to fractional calculus is first given. Behavior of different functions operated by fractional calculus operators are next discussed. Then the two models are described. Results of these models are compared with the experimental results.

3.1 Fractional Calculus Operators and Their Properties

Fractional calculus allows the definition of derivative and integral of generalized order. This often helps in creating a compact representation of a system. Fractional derivative D^a and fractional integral J^a of a function $u(t)$ can be defined as

$$D^a(u(t)) = \frac{1}{\Gamma(1-a)} \frac{d}{dt} \int_0^t \frac{u(\tau)}{(t-\tau)^a} d\tau \tag{3.1}$$

$$J^a(u(t)) = \frac{1}{\Gamma(1+a)} \frac{d}{dt} \int_0^t \frac{u(\tau)}{(t-\tau)^{-a}} d\tau \tag{3.2}$$

Here, Γ is the gamma function and $0 < a < 1$. Fractional derivatives and integrals at time t_m can be calculated numerically by using the following expressions [10, 67]

$$D^a(u(t)) = \frac{\Delta t^{-a}}{\Gamma(2-a)} \left[\frac{(1-a)}{m^a} u_0 + \sum_{j=0}^{m-1} \left((j+1)^{(1-a)} - j^{(1-a)} \right) (u_{m-j} - u_{m-j-1}) \right] \tag{3.3}$$

$$J^a(u(t)) = \frac{\Delta t^{a}}{\Gamma(2+a)} \left[\frac{(1+a)}{m^{-a}} u_0 + \sum_{j=0}^{m-1} \left((j+1)^{(1+a)} - j^{(1+a)} \right) (u_{m-j} - u_{m-j-1}) \right] \tag{3.4}$$

where $u_j = u(j\Delta t)$. The time interval $[0, t_m]$ is divided into m equally spaced sections of size Δt.

In the frequency domain, the Fourier transform of $u(t)$ and its derivatives and integrals of order a are related by Eq.(3.5) and Eq.(3.6) respectively.

$$G_D(\omega) = (i\omega)^a U(\omega) \tag{3.5}$$

$$G_J(\omega) = (i\omega)^{-a} U(\omega) \tag{3.6}$$

where $U(\omega)$, $G_D(\omega)$ and $G_J(\omega)$ denotes the Fourier Transform of $u(t)$, its derivative and integral.

Derivatives and integrals of a pure sinusoidal functions can be characterized by a phase shift and modulation of amplitude, depending on frequency of the sinusoidal function and order of derivatives and integrals as shown in the following equations

$$D^a\left(Sin\left(\omega t\right)\right) = \omega^a Sin\left(\omega t + \frac{\pi a}{2}\right) + \frac{\left(\omega t\right)^{-1-a}}{\omega\Gamma\left(-a\right)} - \frac{\left(\omega t\right)^{-3-a}}{\omega^3\Gamma\left(-a-2\right)} + ... \tag{3.7}$$

$$D^a\left(Cos\left(\omega t\right)\right) = \omega^a Cos\left(\omega t + \frac{\pi a}{2}\right) + \frac{\left(\omega t\right)^{-2-a}}{\omega^2\Gamma\left(-a-1\right)} - \frac{\left(\omega t\right)^{-4-a}}{\omega^4\Gamma\left(-a-3\right)} + ... \tag{3.8}$$

$$J^a\left(Sin\left(\omega t\right)\right) = \omega^{-a} Sin\left(\omega t - \frac{\pi a}{2}\right) + \frac{\left(\omega t\right)^{-1+a}}{\omega\Gamma\left(a\right)} - \frac{\left(\omega t\right)^{-3+a}}{\omega^3\Gamma\left(a-2\right)} + ... \tag{3.9}$$

$$J^a\left(Cos\left(\omega t\right)\right) = \omega^{-a} Cos\left(\omega t - \frac{\pi a}{2}\right) + \frac{\left(\omega t\right)^{-2+a}}{\omega^2\Gamma\left(a-1\right)} - \frac{\left(\omega t\right)^{-4+a}}{\omega^4\Gamma\left(a-3\right)} + ... \tag{3.10}$$

The first term in both Eqs. (3.7) and (3.8) shows a forward phase shifting of the periodic function being operated by the differential operator by an amount $\frac{\pi a}{2}$, where a is the order of the derivative. When the derivative of the periodic function is plotted against the actual periodic function, it gives rise to a clockwise hysteresis loop due to this forward phase shift as shown in Fig. 3.1a. Similarly, the first term in both Eqs. (3.9) and (3.10) show a backward phase shifting of the periodic function being operated by the integral operator by an amount $\frac{\pi a}{2}$, where a is the order of the integral. When the integral of the periodic function is plotted

against the actual periodic function it gives rise to an anticlockwise hysteresis loop due to this backward phase shift as shown in Fig. 3.1b.

A constant function x_0 decays sharply while operated by fractional derivatives and increases with time on being operated by fractional integrals as shown in Eqs. (3.11) and (3.12)

$$D^a(x_0) = \frac{x_0 t^{-a}}{\Gamma(1-a)} \tag{3.11}$$

$$J^a(x_0) = \frac{x_0 t^{a}}{\Gamma(1+a)} \tag{3.12}$$

Hence, under the operation of a fractional differential operator the non harmonic component of a function dies out shortly and its harmonic components gives rise to closed loop clockwise hysteresis and on the other hand the same function shows an anti-clockwise hysteresis with hysteresis loop moving upward with number of cycles when it is operated by a fractional integral operator.

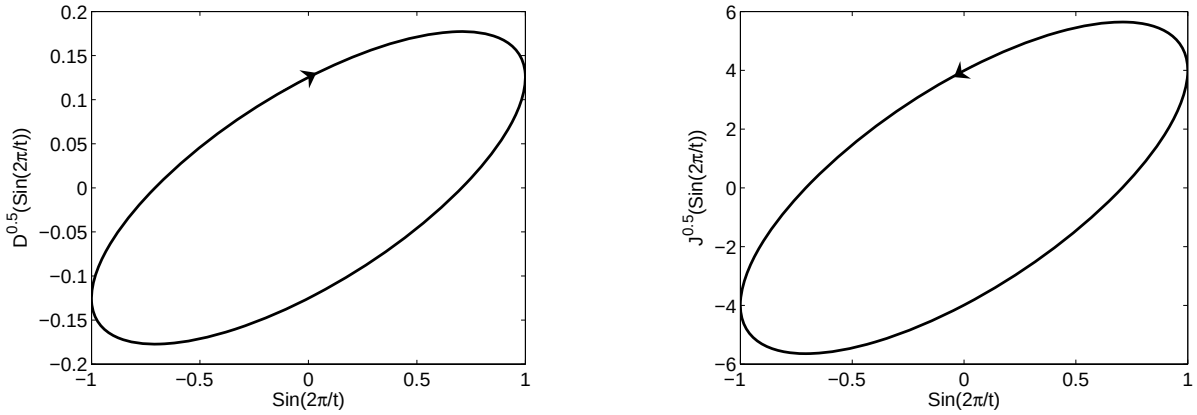

(a) $D^{0.5}(Sin(2\pi/t))$ vs. $Sin(2\pi/t)$ (b) $J^{0.5}(Sin(2\pi/t))$ vs. $Sin(2\pi/t)$

Figure 3.1: Derivative and Integral of Order 0.5

3.2 Development of Fractional Calculus Model

The main features of the hysteresis in the resistance-strain behavior of conductive polymer are the following:

1. The anticlockwise hysteresis loop moves upwards with number of cycles and the width of the hysteresis loop does not necessarily remain constant.

2. When the strain is kept at a constant level the value of the resistance is observed to relax.

Based on these observations and the discussion in the previous section two models are developed in this study to model these features. These models are based upon representing the output resistance as a combination of different fractional order derivatives and integrals with some modifications. In these models, an error function e_m has been defined:

$$e_m = R_{ex}(t_m) - R(t_m) \tag{3.13}$$

$R_{ex}(t_m)$ is the value of the resistance obtained from experiment at $t = t_m$ and $R(t_m)$ is the resistance obtained form the mathematical model. Then considering all the data points in the interval $[t_0, t_n]$, error e has been defined. Error e is minimized for all the models to find the unknown parameters associated with these models. Error minimizations were accomplished using the function 'fmincon' in the optimization toolbox of MATLAB.

$$e = \sum_{m=0}^{n} (R_{ex}(t_m) - R(t_m))^2 \tag{3.14}$$

3.2.1 Model-1: (Combined Fractional Derivative and Integer Order Integral Model)

In this model, a change in resistance $R(t)$ due to applied strain $\epsilon(t)$, has been assumed to be a combination of a linear function of strain, a fractional order derivatives of strain, with each frequency component shifted backward and an integer order integral of different powers of strain, multiplied by an exponentially decaying function. It can be written as

$$R\left(t\right) = C_0\epsilon\left(t\right) + \sum_{k=1}^{N} C_k D_{Ph}^{a_k}(\epsilon(t)) + \sum_{l=1}^{M-N} C_{l+N} \int_0^t e^{-p_l(t-\tau)} \epsilon\left(\tau\right)^{q_l} d\tau \tag{3.15}$$

$D_{Ph}^{a_k}$ is derivative of order a_k with phase of the each frequency component of derivative shifted by $\pi b_k/2$, where $b_k < 0$. If $\epsilon(t)$ can be written in terms of its Fourier components as $\epsilon(t) = \sum_{i=0}^{N} x_i Cos(\omega_i t) + \sum_{i=N+1}^{2N} x_i Sin(\omega_{i-N} t)$, $D_{Ph}^{a_k}$ can be defined as

$$D_{Ph}^{a_k}\left(\epsilon\left(t\right)\right) = D^{a_k}\left(\epsilon_{Ph}\left(t\right)\right) \tag{3.16}$$

where $\epsilon_{Ph}(t)$ is given by the following equation

$$\epsilon_{Ph}(t) = \sum_{i=1}^{N} x_i Sin(\omega_i t + \frac{\pi b_k}{2}) + \sum_{i=N+1}^{2N} x_i Cos(\omega_{i-N} t + \frac{\pi b_k}{2}) \tag{3.17}$$

In the frequency domain, the Fourier transform of $\epsilon_{Ph}(t)$ and $G_{D_{Ph}^{a_k}}(t)$ can be related to the Fourier transform of $\epsilon(t)$ as:

$$\epsilon_{Ph}\left(\omega\right) = i^{b_k}\epsilon(\omega) \tag{3.18}$$

$$G_{D_{Ph}^{a_k}}(\omega) = \omega^{a_k} i^{(a_k+b_k)} \epsilon(\omega) \tag{3.19}$$

The phase shifted fractional order derivatives of $\epsilon(t)$ impart the anticlockwise hysteretic nature to the variation of $R(t)$ with $\epsilon(t)$. The terms in $\sum_{l=1}^{M-N} C_{l+M} \int_0^t e^{-p_l(t-\tau)} \epsilon(\tau)^{q_l} d\tau$ are functions of strain which keep increasing with time at a decaying rate for positive values of the strain. These terms are used to take care of the property of the material which causes its hysteresis loop to move upward with the number of cycles of applied strain.

By using the numerical scheme in Eq. (3.3) for fractional derivative and the trapezoidal rule for integer order integral, instantaneous value of the resistance can be calculated at any time instant t_m as:

$$R(t_m) = R_1(t_m) + R_2(t_m) \tag{3.20}$$

where $R_1(t_m) = C_0 \epsilon(t_m) + \sum_{k=1}^{N} \frac{C_k \Delta t^{-a_k}}{\Gamma(2-a_k)} \left[\frac{(1-a_k)}{m^{(a_k)}} \epsilon_{Ph}(t_0) + \right.$

$\left. \sum_{j=0}^{m-1} \left((j+1)^{(1-a_k)} - j^{(1-a_k)} \right) \left(\epsilon_{Ph}(t_{m-j}) - \epsilon_{Ph}(t_{m-j-1}) \right) \right]$

and $R_2(t_m) = \sum_{l=1}^{M-N} \frac{C_{l+M}}{2} \left(e^{-p_l(t_m - t_0)} \epsilon(t_0) + 2 \sum_{j=0}^{m-1} e^{-p_l(t_m - t_j)} \epsilon(t_j) + \epsilon(t_m) \right) \Delta t$

Here, $t_0 = 0$. $\epsilon_{Ph}(\omega)$ can be calculated by using Eq. (3.17) after obtaining $\epsilon(\omega)$ by performing Fast Fourier Transform (FFT) of $\epsilon(t)$. Then by the Inverse Fourier Transform (IFFT) of $\epsilon_{Ph}(\omega)$, $\epsilon_{Ph}(t)$ can be obtained. $\epsilon_{Ph}(t)$ depends on the unknown parameters b_k. Unknown parameters involved in Eq. (3.20) are $C_k(k = 0, N)$, $a_k(k = 1, M)$, $b_k(k = 1, M)$, $p_k(k = 1, N - M)$, $q_k(k = 1, N - M)$. These parameters have been determined by minimizing e in Eq. (3.14), where $R(t_m)$ is given by Eq. (3.20). The constraints used are $0 < a_k(k = 1, M) < 1$ and $b_k(k = 1, M) < 0$.

3.2.2 Model-2: (Fractional Integral Model)

In this model, the change in resistance has been taken as a combination of the changes in resistance caused by the instantaneous strain $\epsilon(t)$ and its different fractional order integrals. So, the governing equation for this model is

$$R(t) = C_0\epsilon(t) + \sum_{k=1}^{M} C_k J^{a_k}(\epsilon(t)) \tag{3.21}$$

Using the numerical scheme described in Eq. (3.4), it can be written as:

$$R(t_m) = C_0\epsilon\left(t_m\right) + \sum_{k=1}^{M} \frac{C_k \Delta t^{a_k}}{\Gamma\left(2+a_k\right)} \left[\frac{\left(1+a_k\right)}{m^{(-a_k)}} \epsilon\left(t_0\right) + \sum_{j=0}^{m-1} \left(\left(j+1\right)^{(1+a_k)} - j^{(1+a_k)} \right) \left(\epsilon\left(t_{m-j}\right) - \epsilon\left(t_{m-j-1}\right) \right) \right] \tag{3.22}$$

Hence, in sub-model-1, the unknown parameters $C_k(k = 0, M)$, $a_k(k = 1, M)$ were found out by minimizing the error defined in Eq. (3.14), after substituting $R(t_m)$ from Eq. (3.22). Constraints used in the minimization are $0 < a_k(k = 1, M) < 1$.

Sub-model-2 involves some modification of Eq. (3.21). In the frequency domain, Eq. (3.21) can be defined as:

$$R(\omega_j) = C_0\epsilon(\omega_j) + \sum_{k=1}^{M} C_k (i\omega_j)^{-a_k}(\epsilon(\omega_j)) \tag{3.23}$$

According to the discussion in Section 3.1, multiplication of i^{-a_k} with each Fourier component of strain causes a phase shift and imparts a hysteretic nature in the resistance-

strain variation and multiplication of ω^{-a_k} with each Fourier component of strain causes the resistance-strain variation to be dependent on the rate of the application of strain. Sub-model 2 aims to take care of these two effects independently. Hence, Eq. (3.21) was modified as:

$$R(\omega_j) = C_0\epsilon(\omega_j) + \sum_{k=1}^{M} C_k(i\omega_j)^{-a_k} i^{b_k}\epsilon(\omega_j) \tag{3.24}$$

In time domain, Eq. (3.24) can be written as:

$$R(t) = C_0\epsilon(t) + \sum_{k=1}^{M} C_k J_{Ph}^{a_k}(\epsilon(t)) \tag{3.25}$$

where $J_{Ph}^{a_k}(\epsilon(t)) = J^{a_k}(\epsilon_{Ph}(t))$, where $\epsilon_{Ph}(t)$ can be calculated following the procedure described in model-1.

Value of resistance at each data point can be calculated by the following equation

$$R(t_m) = C_0\epsilon\left(t_m\right) + \sum_{k=1}^{M} \frac{C_k \Delta t^{a_k}}{\Gamma\left(2+a_k\right)} \left[\frac{(1+a_k)}{m^{(-a_k)}} \epsilon_{Ph}\left(t_0\right) \right. \tag{3.26}$$

$$\left. + \sum_{j=0}^{m-1} \left((j+1)^{(1+a_k)} - j^{(1+a_k)} \right) \left(\epsilon_{Ph}\left(t_{m-j}\right) - \epsilon_{Ph}\left(t_{m-j-1}\right) \right) \right] \tag{3.27}$$

In this sub-model, $R(t_m)$ has been used substituted in Eq. (3.14) from Eq. (3.27). By minimizing e with constraints $0 < a_k(k = 1, M) < 1$ and $-1 < b_k(k = 1, M) < 1$, unknown parameters $C_k(k = 0, M)$, $a_k(k = 1, M)$, $b_k(k = 1, M)$ have been determined.

3.3 Results From Error-Minimization

Unknown parameters associated with different models have been estimated by minimizing the sum of the squares of errors e in the time interval [0,200] seconds (considering the cyclic variation of resistance with cyclic strain only) of Dataset-1. Parameter estimation was done by assuming N=3 and M=6 and by assuming N=5 and M=8 to observe the improvement of results with an increase in the number of unknown parameters. Using these parameters, the output resistance due to the type of input in Dataset-1 has been determined and its variation with strain and time has been shown from 0 to 400 seconds in Figs. 3.2 and 3.3b respectively. Tables 1 and 2 show the unknown parameters obtained from the error-minimization. Using the parameters in Tables 1 and 2, the variation of electrical resistance for input in dataset-2 was determined. Results are shown in Fig. 3.4. Tables 1 and 2 show percentage of difference in different models using various number of parameters. The difference was calculated using the expression $\frac{100\sqrt{\sum_{i=0}^{n}|R_{ex}(t_i)-R_(t_i)|}}{\sum_{i=1}^{n}|R_{ex}(t_i)|}\%$. After that, error minimization was done using the data corresponding to first two cycles ([0,200] seconds) of dataset-3. Using the paramters obtained from this, variation of electrical resistance with strain was obtained as shown in Fig. 3.5.

3.4 Discussion

Comparison with experimental Dataset-1 shows that all the models are appropriate enough to simulate the path dependent behavior of these materials for that strain rate. An increase in the number of terms involving both fractional derivative or fractional integral results in improvement of result. Results from all the models with N=5 and M=8 (for model-1

and model-3) show a quite satisfactory match with the experimental result with very little differences.

Parameters determined by minimizing the error in the time interval [0,200] seconds of Dataset-1 predict the relaxation in the time interval [200,400] seconds accurately as shown in Figs. 3.3. However, the model involving fractional integral (model-2) is more accurate as compared to the one involving fractional derivative (model-1). Including the effects of phase shift and rate dependence independently (submodel-2 of model-2) imparts a greater flexibility to this model. But comparison with experimental Dataset 2 obtained by applying time dependent strain with higher strain rate shows that sub-model-1 of model-2 is not robust enough to take care of input rate dependence. In Fig. 3.5, it can be observed that, parameters obtained by minimizing the error in first two cycles predict the output in the second two cycles efficiently in case of model-1 and submodel-2 of model-2. Submodel-1 of model-2 fails to prove its efficiency here. Hence, model-1, sub-model-2 of model-2 are more applicable to our data. Sub-model-2 of model-2 matches the experimental results at different strain rates with the minimum error.

In model-1, the C_0 is the coefficient multiplied with the strain, $C_k(k = 1, M)$ are coefficients multiplied with derivative of strain of order $a_k(k = 1, M)$ with phase of each frequency component shifted backward by $\pi b_k/2(k = 1, M)$

In sub-model-1 of model-1, constant C_0 is the coefficient multiplied with the strain, $C_k(k = 1, M)$ are coefficients multiplied with derivative of strain of order $a_k(k = 1, M)$ with phase of each frequency component shifted backward by $\pi b_k/2(k = 1, M)$

Two mathematical models developed using a modified fractional calculus approach to model

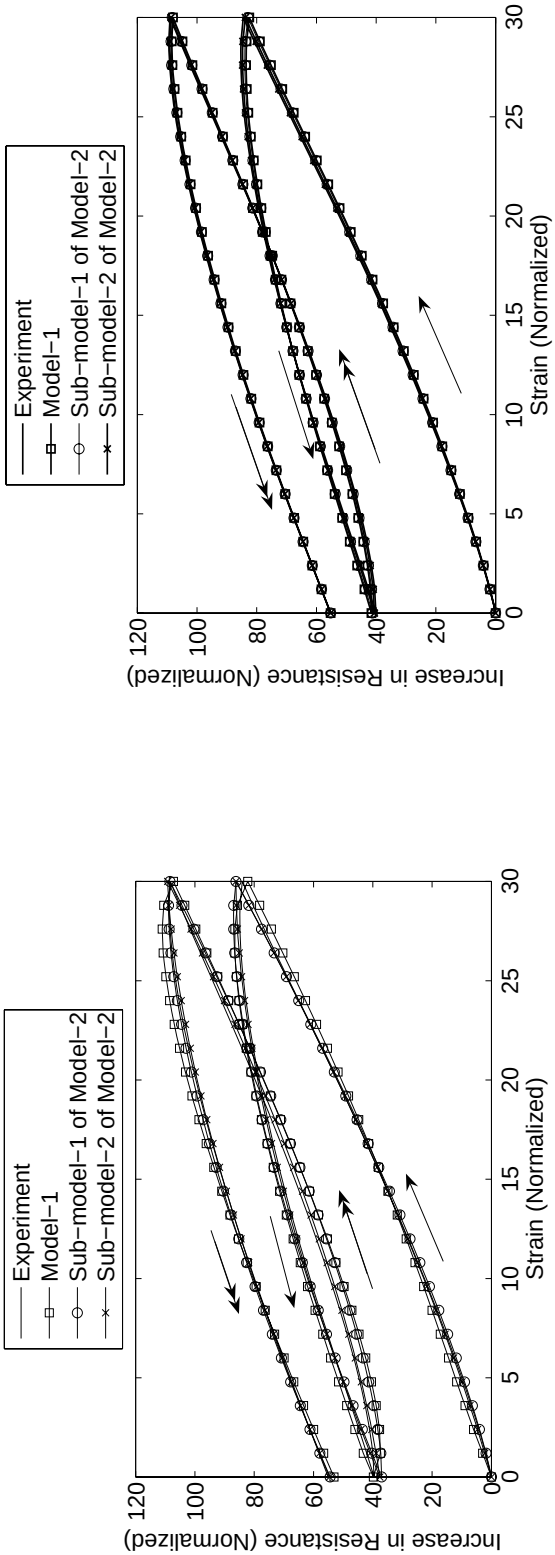

(a) M=3, N=6

(b) M=5, N=8

Figure 3.2: Resistance vs. Strain for Dataset-1

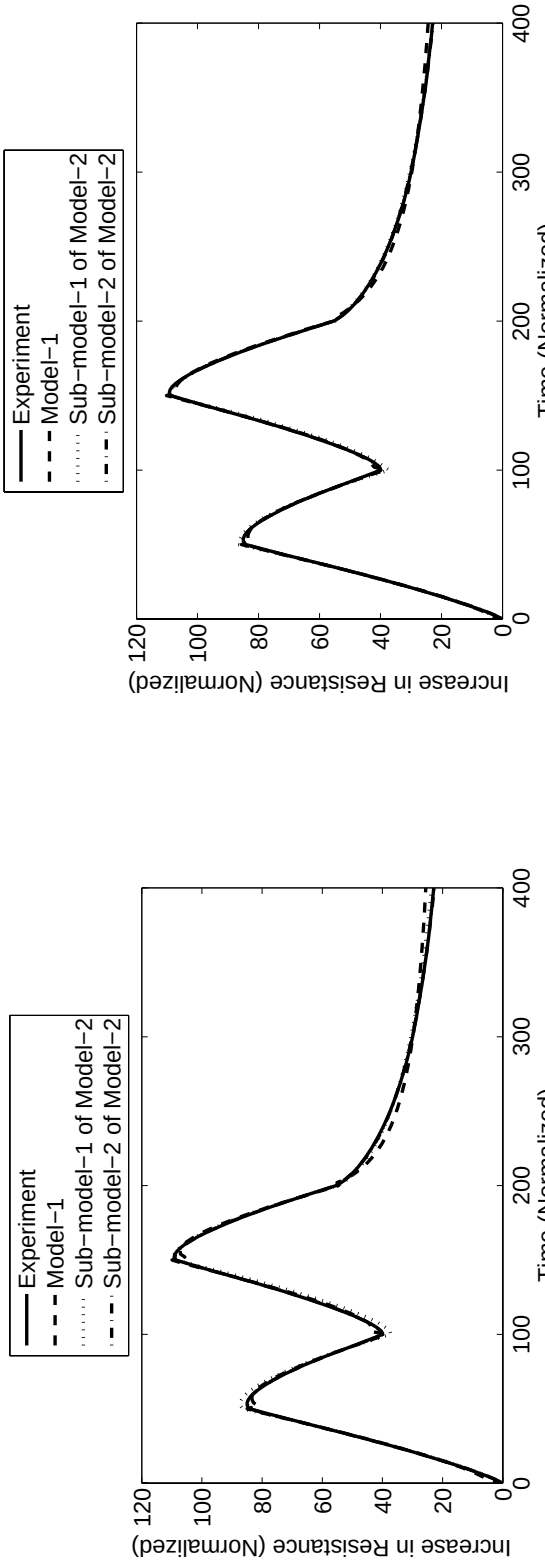

(a) M=3, N=6

(b) M=5, N=8

Figure 3.3: Resistance vs. Time for Dataset-1

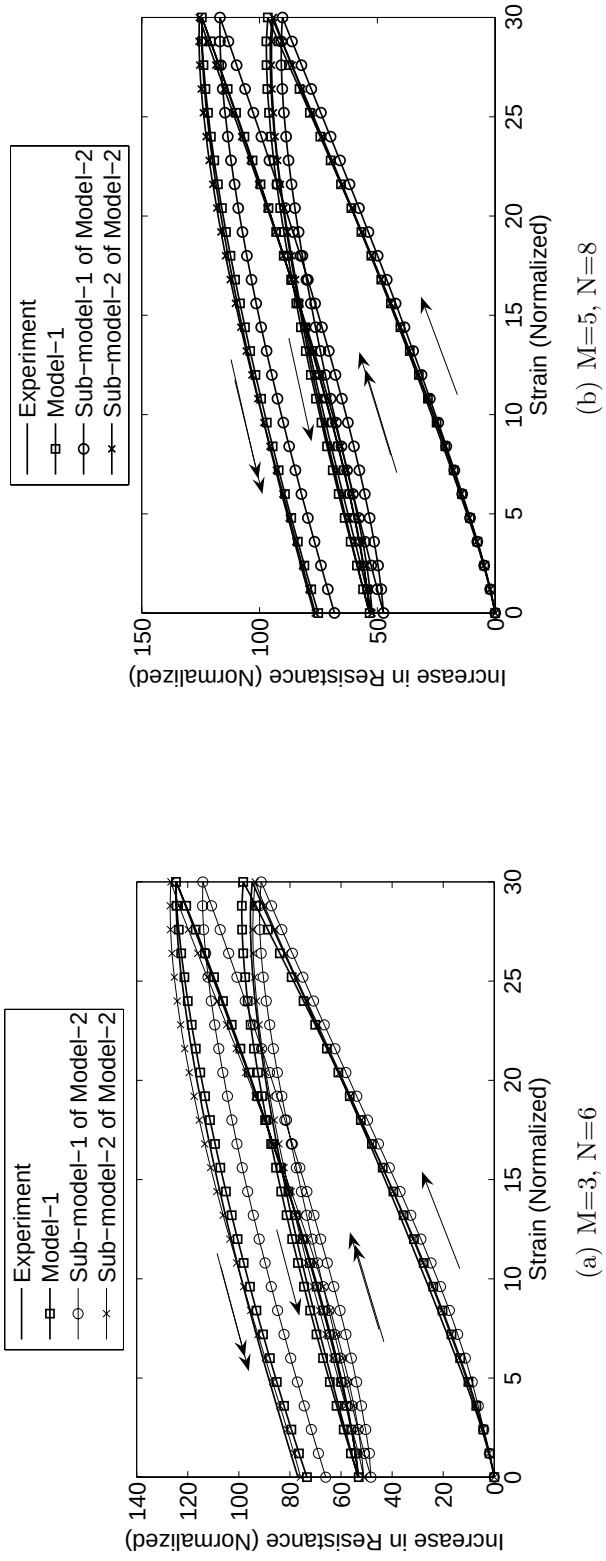

(a) M=3, N=6

(b) M=5, N=8

Figure 3.4: Resistance vs. Strain for Dataset-2

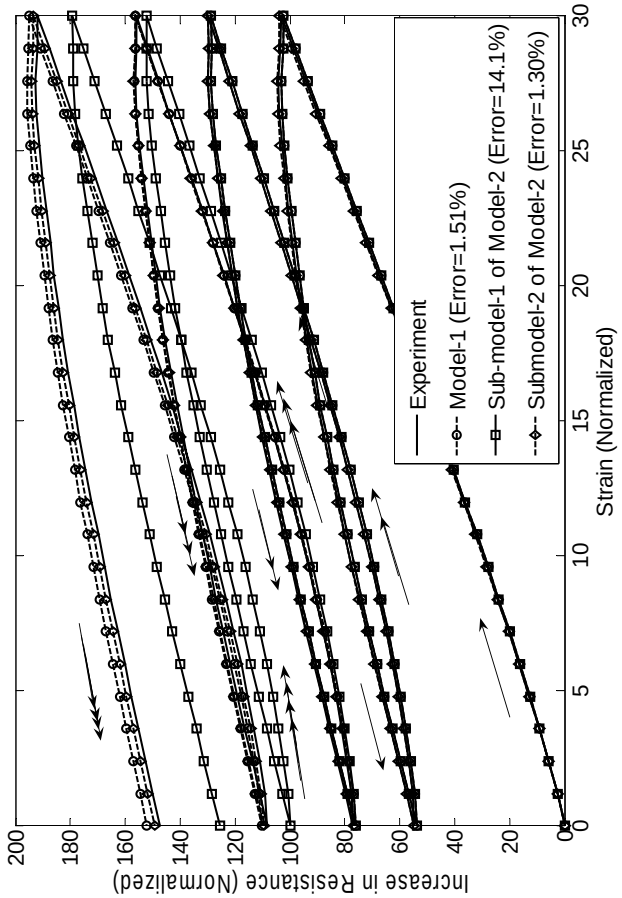

Figure 3.5: Resistance vs. Strain for Dataset-3

Table 3.1: Values of the Parameters and Errors in Different Models (N=3, M=6)

Model	Parameter	Value of the Parameter	Errors (Dataset-1,Dataset-2)
Model-1	$C_k(k=0,6)$	$\{-1000.0000, 662.5600, 419.5589, -221.7519,$ $1.6100, -1123.2110, 256.3312\}$	1.4539%, 5.1200%
	$a_k(k=1,3)$	$\{0.0501, 0.0499, 0.9800\}$	
	$b_k(k=1,3)$	$\{-0.1000, -0.1001, -1.9999\}$	
	$p_k(k=1,3)$	$\{0.0200, 10.000, 1.1211\}$	
	$q_k(k=1,3)$	$\{0.0001, 4.0001, 1.1000\}$	
Sub-model-1 of Model-2	$C_k(k=0,3)$	$\{-32.5047, 132.8861, 41.5930, 28.1075\}$	0.9970%, 19.1000%
	$a_k(k=1,3)$	$\{0.0001, 0.3930, 0.4102\}$	
Sub-model-2 of Model-2	$C_k(k=0,3)$	$\{21.9328, 9.3891, 15.4486, 100.4699,$	0.7121%, 4.1100%
	$a_k(k=1,3)$	$\{0.6229, 0.5804, 0.3577\}$	
	$b_k(k=1,3)$	$\{0.9999, -0.9999, 0.1812\}$	

Table 3.2: Values of the Parameters and Errors in Different Models (N=5, M=8)

Model	Parameter	Value of the Parameter	Errors (Dataset-1,Dataset-2)
Model-1	$C_k(k=0,8)$	$\{-756.9331, -301.9868, 590.4756, -258.7771,$ 624.0835, -78.0835 146.7035, 2.1827, -1.6600$\}$	1.0190%, 3.0141%
	$a_k(k=1,5)$	$\{0.0001, 0.0409, 0.9593, 0.0408,$ 0.0002$\}$	
	$b_k(k=1,5)$	$\{-0.0002, -0.0801, -1.9999, -0.0901,$ -0.0005$\}$	
	$p_k(k=1,3)$	$\{0.6269, 0.0176, 0.0177\}$	
	$q_k(k=1,3)$	$\{0.9716, 0.0045, 0.4755\}$	
Sub-model-1 of Model-2	$C_k(k=0,5)$	$\{5.0950, -61.3725, 253.7714, 97.4030,$ -46.0027, -66.1477$\}$	0.7110%, 17.0019%
	$a_k(k=1,5)$	$\{0.3820, 0.1626, 0.9342, 0.4429,$ 0.9999$\}$	
Sub-model-2 of Model-2	$C_k(k=0,5)$	$\{-136.1364, 61.8550, 44.8370, 132.1557,$ 139.4960, -84.1253$\}$	0.6101%, 3.0100%
	$a_k(k=1,5)$	$\{0.0001, 0.5992, 0.5161, 0.0002, 0.5906\}$	
	$b_k(k=1,5)$	$\{0.0195, -0.7070, 0.1644, 0.0175, -0.1589\}$	

the variation of electrical resistance with strain in conductive polymer nanocomposite materials have been presented. Efficiency of the models have been shown by comparison with experimental result. Another mathematical model developed using a modified Preisach approach will be presented in the next chapter.

Chapter 4

Preisach Model

The modified Preisach model has been developed by using a modified version of the Preisach hysteresis operator and a dynamic operator. At first the classical Preisach model has been described. Then, modifications on the classical Preisach operators have been explained. After that a new dynamic relaxation operator has been introduced. Next, the dynamic hysteresis model using the modified Preisach operator and the dynamic operator has been described. Comparison of the results obtained from the modified Preisach model with the experimental results have beam shown.

4.1 The Preisach Model

Preisach model considers the hysteresis loop to be a weighted combination of output from different independent hysteresis operators. Each independent operator $\gamma_{\alpha\beta}$ is a mechanical unit that up switches to a value +1 when the value of input u is α and is increasing and

downswitches to a value -1 when the value of input u is β and is decreasing. Variables α and β are called the upswitching and downswitching values respectively. It will be assumed subsequently that $\alpha \geq \beta$, which is quite natural from the physical point of view [33]. Figure 4.1 shows the behavior of $\gamma_{\alpha\beta}$. The ascending branch *abcde* is followed when the input increases monotonically and the descending branch *edfba* is followed when the input decreases monotonically. Each operator $\gamma_{\alpha\beta}$ has a weight $\mu(\alpha\beta)$ associated with it. According to the Preisach model output $f(t)$ is given by Eq. 4.1.

$$f\left(u(t)\right) = \int\limits_{T} \gamma_{\alpha\beta}\mu\left(\alpha,\beta\right) d\alpha d\beta = \int\limits_{T_1} \mu\left(\alpha,\beta\right) d\alpha d\beta - \int\limits_{T_2} \mu\left(\alpha,\beta\right) d\alpha d\beta \tag{4.1}$$

Figure 4.2 show the geometric interpretation of the Preisach model. The space spanned by α and β is called Preisach-Mayergoyz (PM) [after Preisach, 1935; Mayergoyz, 1985] space [68]. ΔABC is the region where $\alpha \geq \beta$. This is the feasible region of PM-space. The input protocol leads to a trajectory separating the PM-space into upswitched and downswitched regions as shown in Fig. 4.2. T_1 and T_2 refer to the regions where operators are in the upswitched and the downswitched states and T refers to the region containing all the operators. Depending on the input history, T_1 and T_2 change.

At the beginning of the cycle, all the operators are in the downswitched state as shown in Fig. 4.2a. The output f_1 at this stage can be calculated using Eq. 4.1. When input reaches a value u_2, output f_2 is given by Eq. 4.2. Figure 4.2b shows the regions where the operators are at the upswitched and the downswitched states. At the end of the first half of the cycle, all the operators come to the upswitched state. Equation 4.4 shows the value of output and Fig. 4.2c shows the PM space. Now, after the input starts decreasing monotonically and

reaches a value u again, the output reaches a value f_4 as shown in Eq. 4.5. Regions with the upswitched and the downswitched operators in the PM space are as shown in Fig. 4.2d. Comparison of Fig. 4.2b and Fig. 4.2d shows that when the input increases monotonically the operators in the region ABCD is in downswitched state at u and the operators in the same region remains in upswitched state at the same value of input when the input decreases monotonically. This creates a difference in output $f_4 - f_2$ as given in Eq. 4.6 and causes the hysteresis. At the end of the cycle all the operators go back to the downswitched state and in the original Preisach model the output returns to its initial value. Figure 4.3 shows the formation hysteresis in a complete cycle.

$$f_1 = \int_T -\mu(\alpha, \beta)\, d\alpha d\beta \tag{4.2}$$

$$f_2 = \int_{T_1} \mu(\alpha, \beta)\, d\alpha - \int_{T_2} \mu(\alpha, \beta)\, d\alpha d\beta \tag{4.3}$$

$$f_3 = \int_T \mu(\alpha, \beta)\, d\alpha d\beta \tag{4.4}$$

$$f_4 = \int_{T_3} \mu(\alpha, \beta)\, d\alpha - \int_{T_4} \mu(\alpha, \beta)\, d\alpha d\beta \tag{4.5}$$

$$f_4 - f_2 = 2 \int_{DEBF} \mu(\alpha, \beta d\alpha d\beta \tag{4.6}$$

The hysteresis operators described in the previous section give rise to a closed loop hysteresis

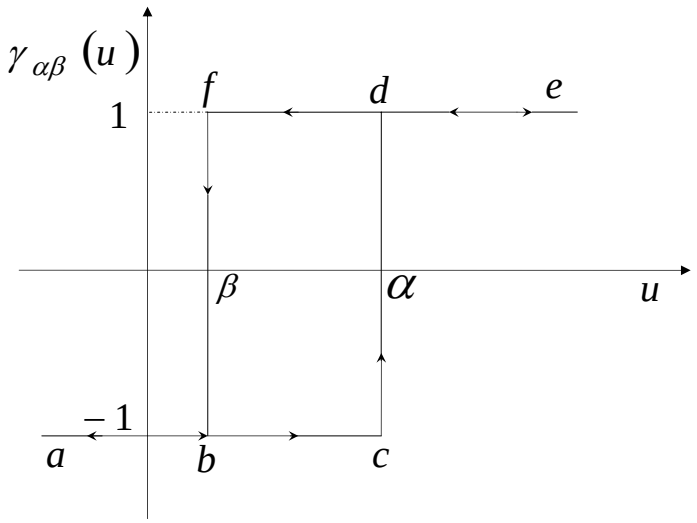

Figure 4.1: Hysteresis Operator ($\gamma_{\alpha,\beta}(u)$) in Preisach model

in a complete cycle and cannot model a relaxation of the output at a constant input. In our model, upward shifting of the hysteresis loop has been taken care of by a modification of the hysteresis operators and relaxation has been accounted for by the addition of a dynamic operator, to be defined subsequently. The part of the output obtained from the modified hysteresis operators is termed as static part of the output (f_s) and the other part of the output obtained from the dynamic operators is termed as dynamic part of the output (f_d). Total output from the system is the combination of f_s and f_d.

4.1.1 Modification of the Hysteresis Operator

For our problem, both the input strain and the output electrical resistance always remain positive. So, α, β and output from each operator $\gamma_{\alpha\beta}$ always remain positive. Hence, in the downswitched state, output from each operator is zero. The hysteresis operator considered in our model is shown in Fig. 4.4. Here, at α the operator upswitches by a value +1. But

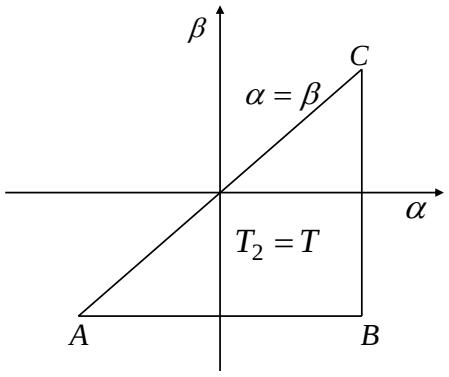

(a) At the beginning of the cycle

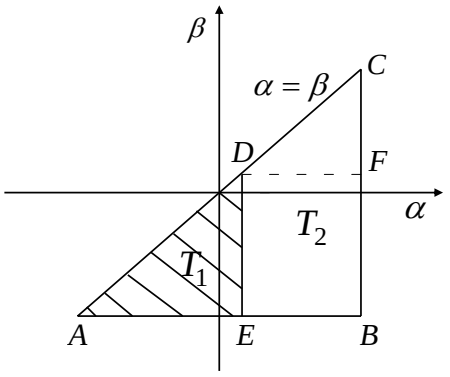

(b) During the first half of the cycle when input increases monotonically and reaches a value u

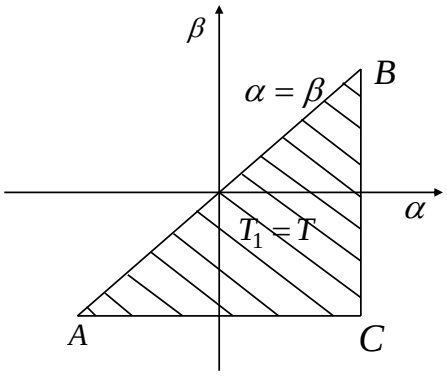

(c) At the end of the first half of the cycle

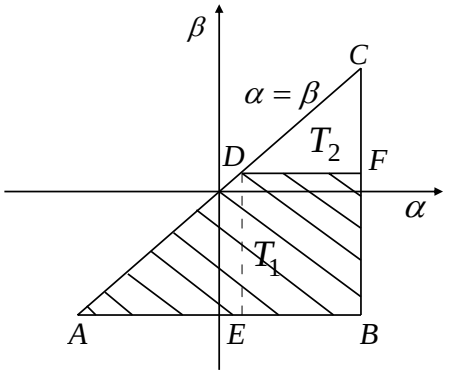

(d) During the second half of the cycle when input decreases monotonically and reaches a value u

Figure 4.2: Preisach-Mayergoyz Space at Different Stages of the First Cycle

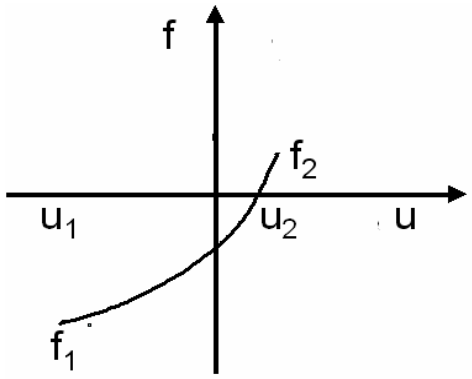

(a) During the first half of the cycle when input increases monotonically and reaches a value u_2

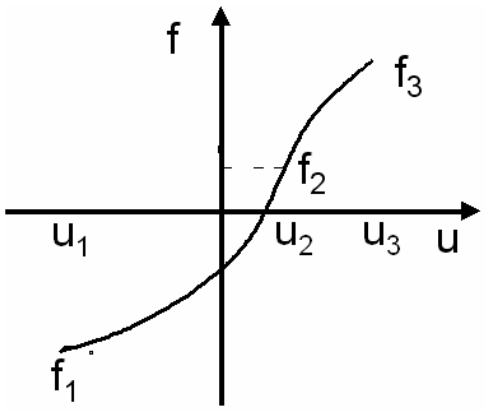

(b) At the end of the first half of the cycle

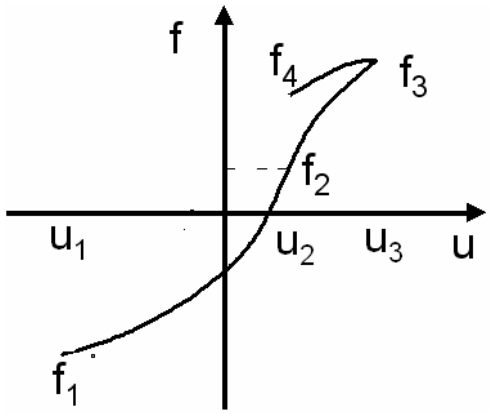

(c) During the second half of the cycle when input decreases monotonically and reaches a value u_2

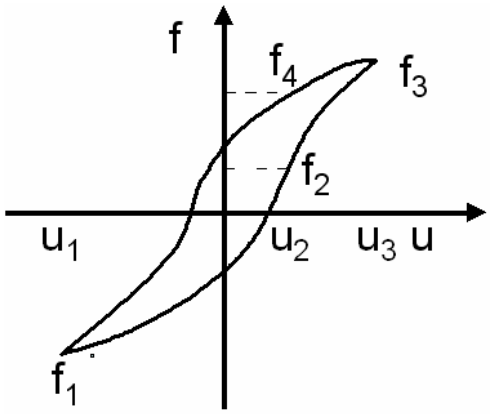

(d) At the end of the cycle

Figure 4.3: Variation of Output with Input at Different Stages of the First Cycle

at β it does not downswitch fully. It downswitches by a value η which is an additional parameter associated with each hysteresis operator and is being introduced in this study. Due to this partial downswitching at β, the loop keeps shifting upward with the number of cycles as shown in Fig. 4.4. If the value of η is more than 1 the loop will shift downward. As the operators do not downswitch fully, at any time instant, an operator can be either fully downswitched, upswitched or partially downswitched depending on the input history. A partially downswitched state refers to the state of the operator after it downswitches by η followed by any upswitching. It can also be called partially upswitched state. Output of an operator at partially downswitched state after n number of upswitchings and partial downswitchings will be $n(1-\eta)$ and of an operator at on stage after n number of upswitchings and partial downswitchings will be $n(1-\eta)+1$. Hence, static part of the output of the system at any time t can be written as:

$$f_s\left(u(t)\right) = \iint_{T_1} \left[n\left(\alpha,\beta\right)\left(1-\eta\left(\alpha,\beta\right)\right)+1\right]\mu\left(\alpha,\beta\right)d\alpha d\beta + \iint_{T_3} n\left(\alpha,\beta\right)\left(1-\eta\left(\alpha,\beta\right)\right)\mu\left(\alpha,\beta\right)d\alpha d\beta \tag{4.7}$$

where T_3 refers to the regions where all the operators are in partially downswitched state.

Figure 4.8 describes the states of the operators in the PM space during different stages of a cycle. Equations 4.8- 4.11 show the value of output at these stages. At the beginning of the first cycle, the output is zero, as all the operators are in the downswitched state. When the input increases monotonically and reaches a value u, the output is given by Eq. 4.8. States of different operators in PM space at this stage is shown in Fig. 4.8a. Figure 4.8b and Eq. 4.9 show the state of operators and the value of the output at the end of the first cycle.

When the input starts decreasing some operators start downswitching partially as shown in Fig. 4.8c. Equation 4.10 shows the value of the output at this stage. At the end of the cycle all the operators come to a partially downswitched state as shown in Fig. 4.8d. Output at this stage can be calculated using Eq. 4.11. Figure 4.5 shows the formation hysteresis in a complete cycle.

$$f_{s_2} = \int_{T_1} \mu(\alpha, \beta) d\alpha d\beta \tag{4.8}$$

$$f_{s_3} = \int_{T} \mu(\alpha, \beta) d\alpha d\beta \tag{4.9}$$

$$f_{s_4} = \int_{T_1} \mu(\alpha, \beta) d\alpha d\beta + \int_{T_3} (1 - n(\alpha, \beta))\, \mu(\alpha, \beta) d\alpha d\beta \tag{4.10}$$

$$f_{s_5} = \int_{T} (1 - n(\alpha, \beta))\, \mu(\alpha, \beta) d\alpha d\beta \tag{4.11}$$

In this way, a partial downswitching causes a difference between the outputs both at the end and the beginning of the cycle. Consequently, the hysteresis loop keeps shifting upward.

4.1.2 Addition of a Dynamic Operator

The dynamic part of the output has been assumed to be the result of dynamic relaxation operators. These operators have upswitching value ζ, but no downswitching value. When the input monotonically increases and reaches a value ζ, an operator h_ζ upswitches to a

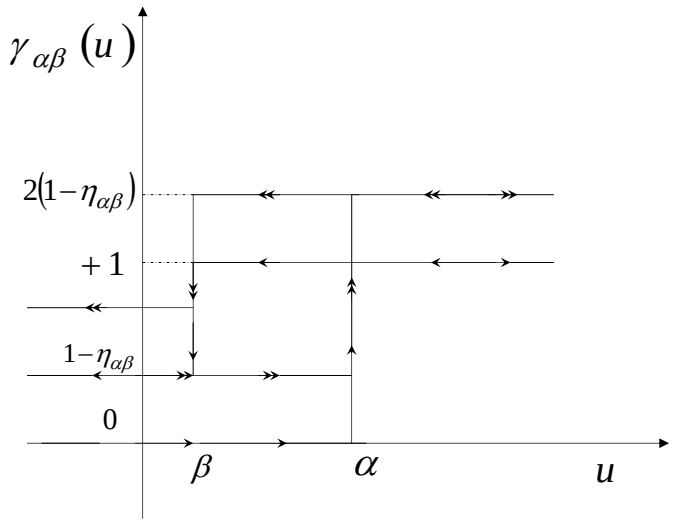

Figure 4.4: Proposed Modified Hysteresis Operator

value $\sum_{j=1}^{P} A_j$ and then decays exponentially as given in Eq. 4.12. Here $A_j(\zeta), b_j(\zeta), c_j(\zeta)$ $(j = 1, .., P)$ are unknown parameter associated with each dynamic operator. These need to be determined from experimental data. The dynamic relaxation operators lie on a one dimensional space spanned by ζ. Hence, for a given input history at time t, the dynamic part of the output will be given by Eq. 4.13.

$$h_\zeta(t) = \begin{cases} 0 & \text{if } t < t_0 \\ \sum_{j=1}^{P} A_j e^{-b_j (t-t_0)^{c_j}} & \text{if } t \geq t_0 \end{cases} \tag{4.12}$$

$$f_d(t) = \int_{T_d} \sum_{i=1}^{n_\alpha} \sum_{j=1}^{P} A_j e^{-b_j \left(t - t_{\zeta i}\right)^{c_j}} d\zeta \tag{4.13}$$

Here, T_d refers to the domain where the operators are in the upswitched state. The shape and size of T_d depends upon the input history. Here, n_ζ refers to the total number of times

h_ζ has been upswitched and $t_{\zeta i}$ refers to the time instant at which h_ζ was upswitched for the ith time. Total value of the output from the system is the combination of static and dynamic part of the output obtained from Eq. 4.7 and Eq. 4.13.

4.2 Identification of Parameters

The objective of the present research is to identify parameters in the model from the experimental data. In our case, strain $\epsilon(t)$ is the input $u(t)$ and electrical resistance $R(t)$ is the output $f(t)$. Unknown material parameters can be found out by minimizing the error of the output predicted by the mathematical model with respect to the experimental data. Before that, some assumptions have been made regarding parameters associated with the hysteresis and dynamic operators. For the hysteresis operators, PM space has been assumed to be consisting of different bins $(i, j)(i = 1, N; j = 1, i)$ as shown in Fig. 4.7. Area under each bin has the same values of μ and η. Bins of finer size improve the accuracy of the model. Value of μ and η in bin (i, j) have been assumed to be a combination of M numbers of different modal functions as shown in Eq. 4.14 and Eq. 4.15.

$$\mu\left(i,j\right) = \sum_{l=1}^{M} b_{\mu_l} \phi_{\mu_l}\left(i,j\right) \tag{4.14}$$

$$\eta\left(i,j\right) = \sum_{l=1}^{M} b_{\mu_l} \phi_{\eta_l}\left(i,j\right) \tag{4.15}$$

The lth modal functions ϕ_{μ_l} and ϕ_{η_l} are given by the following equations.

$$\phi_{\mu_l}(i,j) = Cos\left(\frac{\pi m_{\mu_l} i}{N}\right) Cos\left(\frac{\pi n_{\mu_l} j}{N}\right) + Cos\left(\frac{\pi n_{\mu_l} i}{N}\right) Cos\left(\frac{\pi m_{\mu_l} j}{N}\right) \tag{4.16}$$

$$\phi_{\eta_l}(i,j) = Cos\left(\frac{\pi m_{\eta_l} i}{N}\right) Cos\left(\frac{\pi n_{\eta_l} j}{N}\right) + Cos\left(\frac{\pi n_{\eta_l} i}{N}\right) Cos\left(\frac{\pi m_{\eta_l} j}{N}\right) \tag{4.17}$$

Hence, $\mu(\alpha,\beta)$ is a function of unknown parameters b_{μ_l}, m_l, n_l and $\eta(\alpha,\beta)$ is a function of unknown parameters b_{η_l}, m_l, n_l $(l = 1,..,M)$. Details of this modal function based identification procedure can be found in a paper by Gueyer et al.[68].

Parameter $A_j(\zeta)$ of the dynamic operators has been assumed to be of the form $A_j = a_j\zeta^{d_j} (j = 1,..,P)$ and $b_j(\zeta)$ and $c_j(\zeta)$ have been assumed to be same for all values of ζ. So, unknown parameters associated with the dynamic part of the model are $a_j(\zeta)$, $b_j(\zeta)$, $c_j(\zeta)$ and $d_j(\zeta)$ $(j = 1,..,P)$.

By using all these assumptions, electrical resistance can be written as a function of the parameters b_{μ_l}, m_{μ_l}, n_{μ_l}, b_{η_l}, m_{η_l}, n_{η_l}, a_j, b_j, c_j and d_j $(l = 1,..,M; j = 1,..,P)$. By finding out the values of these parameters, the material can be characterized.

Now an error function can be defined as:

$$E = \sum_{i=1}^{N} \left(R_e(i) - R_c(i)\right)^2 \tag{4.18}$$

Here, $R_e(i)$ is the electrical resistance obtained from the experiment and $R_c(i)$ is the electrical resistance obtained from Eq. 4.7 (using the assumptions described above) at the ith data point. By minimizing this error, the unknown parameters have been found out.

Table 4.1: Error and CPU Time Corresponding to Different Values of M and P

M	P	%Error (Dataset-1, Dataset2)	CPU Time for Error Minimization(Seconds)
3	3	2.47, 4.3	1320
5	5	1.97, 2.71	1840
7	7	1.18, 2.1	2790

4.3 Results and Discussion

Unknown parameters associated with different models have been estimated by minimizing the sum of the squares of errors E in the time interval [0,200] seconds (considering the cyclic variation of resistance with cyclic strain only) of Dataset-1. Parameter estimation was performed by assuming different values of M (number of modal functions for the distribution of $\mu(\alpha, \beta)$ and $\eta(\alpha, \beta)$ in the PM space) and P (number of exponential functions for the dynamic operators h_ζ) to observe the improvement of results with an increase in number of parameters. The error minimization has been carried out by using the function 'fmincon' in MATLAB using a personal computer (Dell Precision PWS690) with 2.66GHz processor speed and 2GB RAM. Using these parameters change in electrical resistance was found out in the time interval [0,400] seconds. Figures 4.8a, 4.8b show the change in electrical resistance with strain and time respectively for the type of strain input in Dataset-1. Corresponding errors and CPU times have been tabulated in Table 4.1. After that using the same parameters variation of electrical resistance for input in Dataset-2 was determined. Results are shown in Figs. 4.9a and 4.9b. Table 4.1 shows the corresponding errors. Comparison with experimental Dataset-1 shows that the model is appropriate enough to simulate the path dependent behavior of these materials for that strain rate. An increase in the number

of modal functions for the distribution of $\mu_0(\alpha, \beta)$, $\mu_1(\alpha, \beta)$ and $\eta(\alpha, \beta)$ in the PM space and number of exponential functions for the dynamic operators h_ζ results in an improvement of the results. Parameters determined by minimizing the error in the time interval [0,200] seconds of Dataset-1 predicts the relaxation in the time interval [200,400] seconds accurately as shown in Fig. 4.8b. Figure 4.9 showing the comparison with experimental Dataset 2 obtained by applying time dependent strain with higher strain rate shows that the model is robust enough to take care of input rate dependence. Figure 4.10 shows the variation of electrical resistance with strain in first four cycles obtained using the parameters determined by using the data for first two cycles. This further proves the predictive capability of the model.

In this chapter, description of the modified Preisach model and comparison of its result with the experimental result have been given. A comparison of Table 5.1 with Table 4.1 and Table 4.2 shows that the modifed Preisach model simulates the variation of electrical resistance with strain in conductive polymer nanocomposites with less error. We have developed a compensator using the modified Preisach model to remove the effects of hysteresis and relaxation from the output (electrical resistance) from conductive polymer nanocomposite sensor. The details of the compensator will be presented in the next chapter.

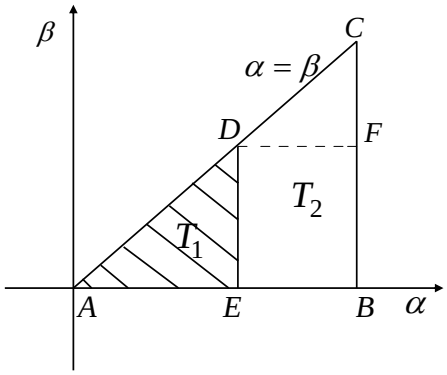

(a) During the first half of the cycle when input increases monotonically and reaches a value u

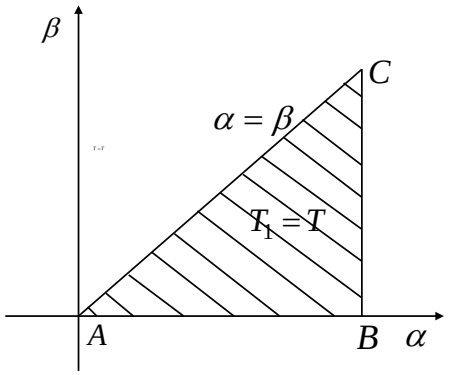

(b) At the end of the first half of the cycle

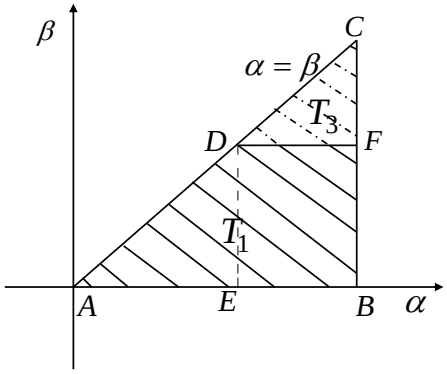

(c) During the second half of the cycle when input decreases monotonically and reaches a value u

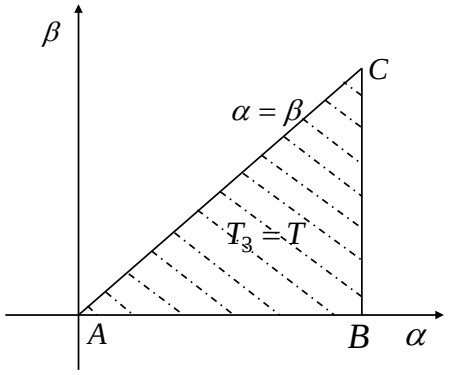

(d) At the end of the cycle

Figure 4.5: Preisach-Mayergoyz Space at Different Stages of the First Cycle

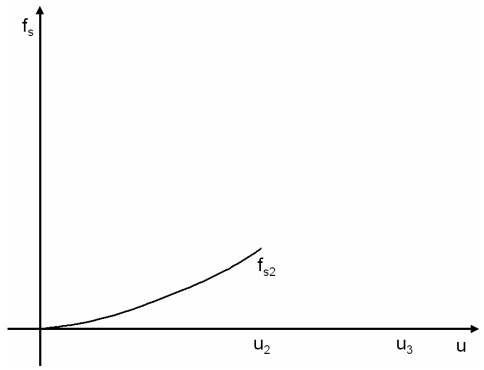

(a) During the first half of the cycle when input increases monotonically and reaches a value u_2

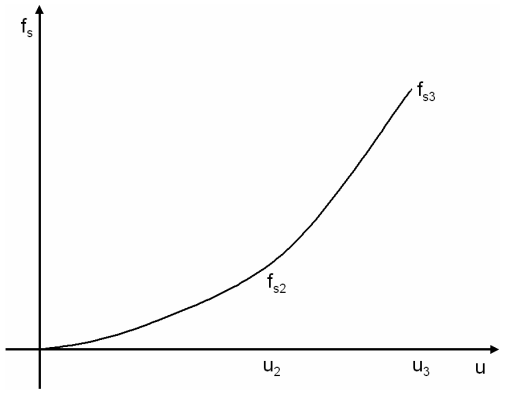

(b) At the end of the first half of the cycle

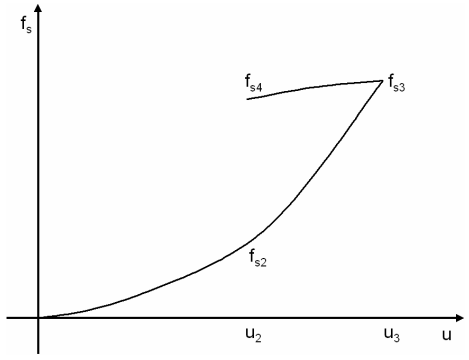

(c) During the second half of the cycle when input decreases monotonically and reaches a value u_2

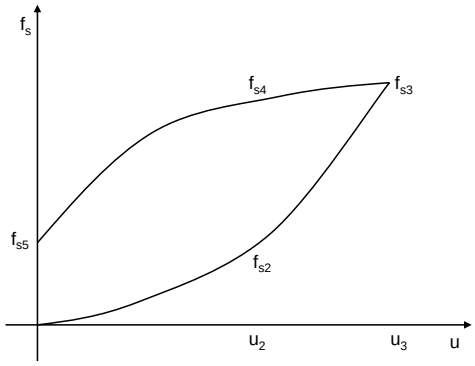

(d) At the end of the cycle

Figure 4.6: Variation of Output with Input at Different Stages of the First Cycle

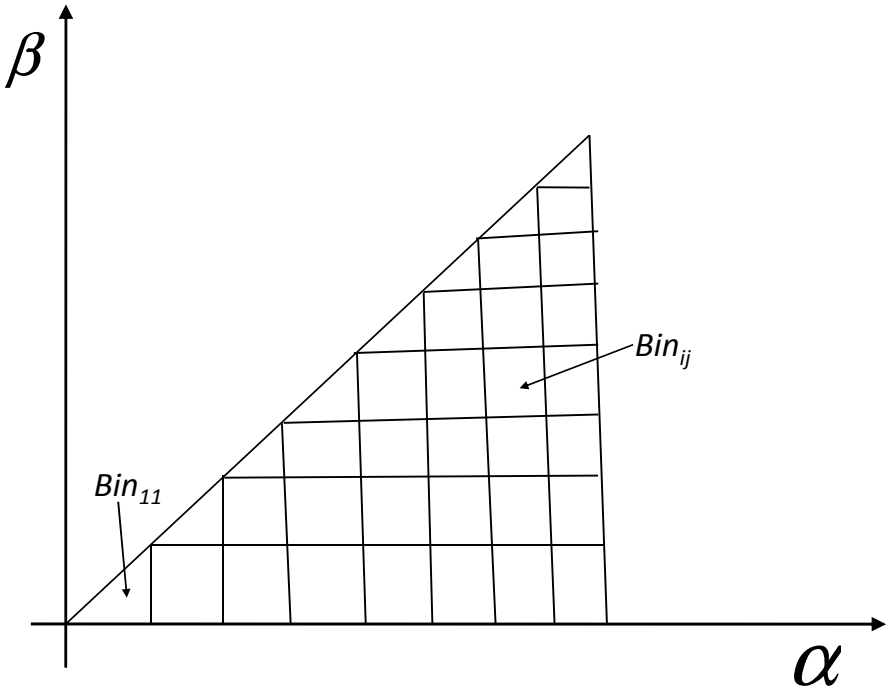

Figure 4.7: PM Space Divided into Bins

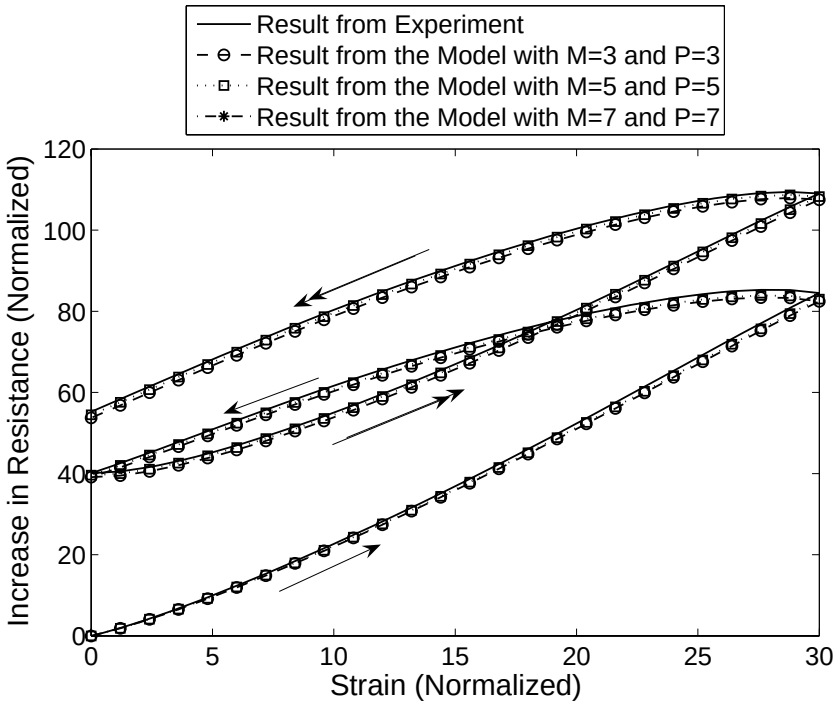

(a) Resistance vs. strain

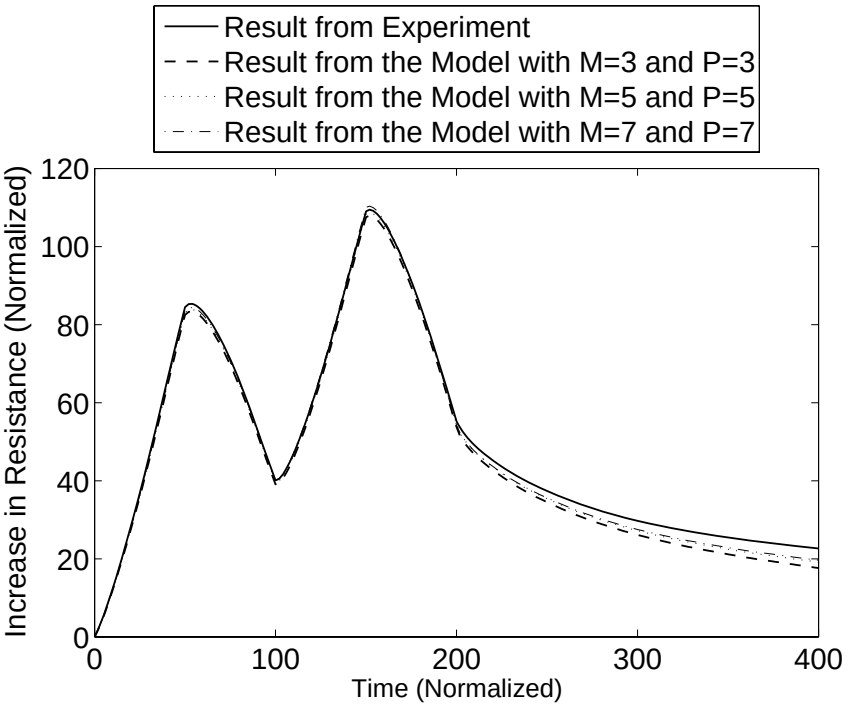

(b) Resistance vs. time

Figure 4.8: Comparison of the Results from the Model with the Experimental Result (Dataset-1)

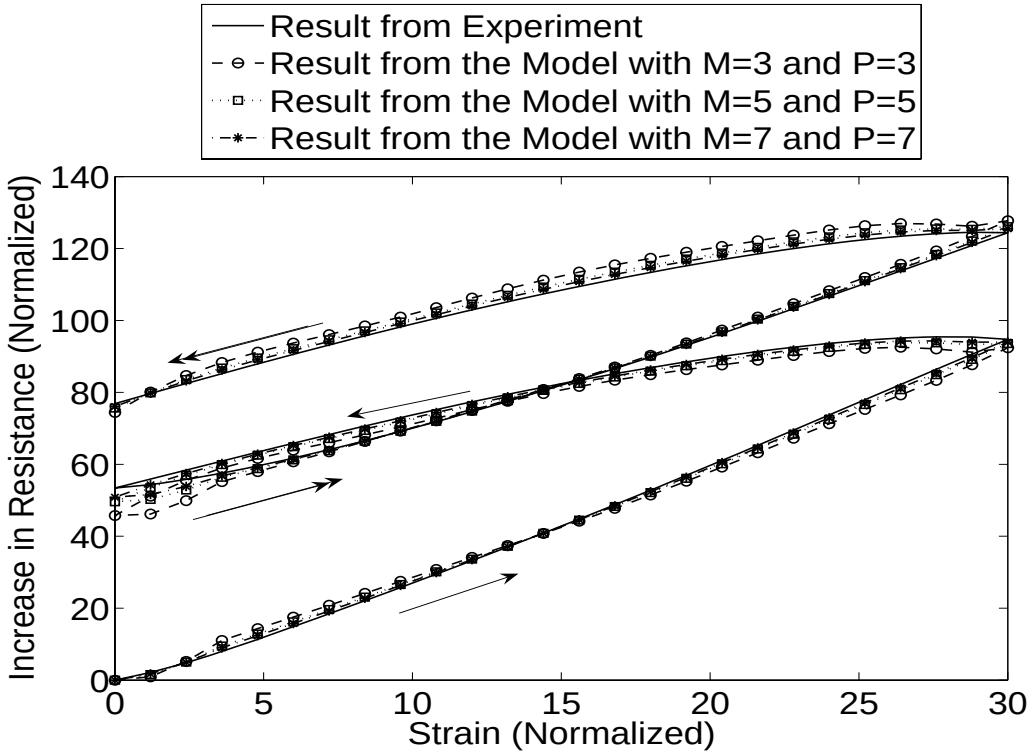

Figure 4.9: Comparison of the Results from the Model with the Experimental Result (Dataset-2)

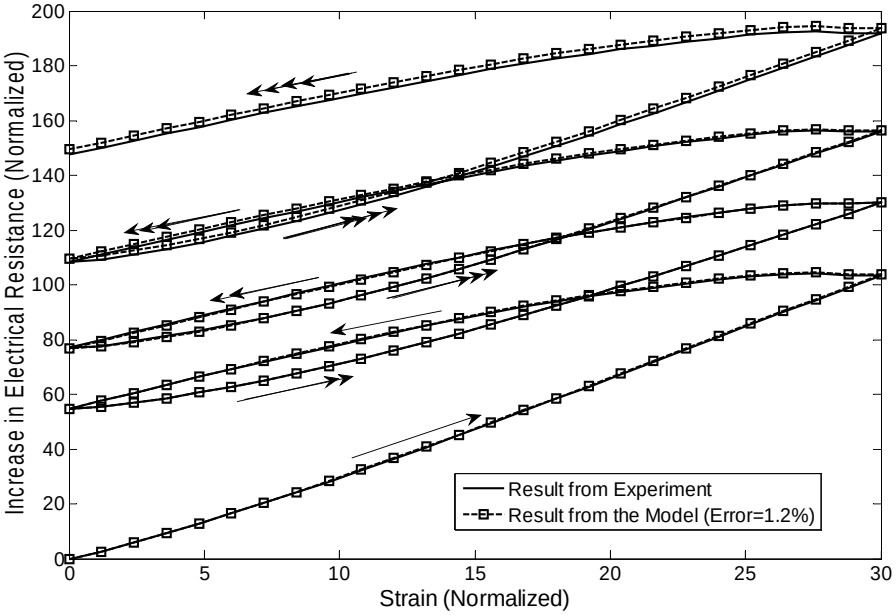

Figure 4.10: Comparison of the Results from the Model with the Experimental Result (Dataset-3)

Chapter 5

Compensator for Sensor Hysteresis and Relaxation

This chapter describes a compensator developed by using the modified dynamic Preisach model. At first, the concept of Everett integral and its use in calculation of output from a system with hysteresis using the classical Preisach model is described. After that a modified Everett integral for our modified Preisach model is proposed and calculation of the output using this modified Integral has been explained. Then a compensation algorithm using modified Everett integral has been described. Results of hysteresis compensation have been presented. Efficiency of the compensator has been discussed by comparison of the strain predicted by the compensator with the actual strain input.

5.1 Everett Integral and Everett Surface

Everett Integrals and Everett surfaces are used to facilitate the calculation of output at any time instant from the input history for a system with Preisach hysteresis. Preisach model considers the output at time instant to be a weighted combination of the outputs from all the hysteresis operators. Hence, calculation of output involves evaluation of 2-D integral over the P-M space as described in Chapter 5. By using the Everett surface, an evaluation of the 2-D integral over the PM space is avoided. Everett integral is used to calculate the change in the value of output when the value of input changes from an extremum to a different value. By plotting the Everett integral against current extreme value of input and a new input value, a surface is generated. This is called the Everett surface. Use of Everett surface in output calculations has been described in Section 5.3.

Everett Integral is defined as:

$$E\left(h_1, h_2\right) = f_{h_2} - f_{h_1} = \begin{cases} 2\displaystyle\int_{D_1} \mu(\alpha, \beta) d\alpha d\beta & \text{if } h_1 < h_2; \\ 2\displaystyle\int_{D_1} -\mu(\alpha, \beta) d\alpha d\beta & \text{if } h_1 > h_2. \end{cases}$$

D_1 refers to the domain in the PM space in which the hysteresis operators are upswitched or downswitched when the input changes from h_1 to h_2. Everett Integral $E(h_1, h_2)$ represents the difference in output when the input reaches a value h_2 from an extreme value h_1 and for different values of (h_1, h_2) are plotted as a surface. This surface is called Everett surface. For classical Preisach model, Everett surface is symmetric with respect to the line $h_1 = h_2$.

Let us suppose that starting from time t_0, the value of input changes as shown in Fig. 5.1. At time instant t_k, the current extreme value of input is 0 and the current value of input is u_k. The configuration of the PM space at time t_k is shown in Fig. 5.2a . In between the time instants t_0 to t_k, operators in the domain ΔOAB switches up. Hence, an increase in the value of the output from the time instant t_0 to the time instant t_k can be calculated by evaluating area integral over ΔOAB. This value termed $E(0, u_k)$ can be directly accessed from the Everett surface generated for this system as shown in Fig. 5.3. After time instant t_{n1}, the value of the input starts decreasing from u_{n1}. At time instant t_l, the current extreme value of the input is u_{n1} and the current value of the input is u_l. Configuration of the PM space at time instant t_l is shown in Fig. 5.2b. Hence, a decrease in the value of the output from time instant t_{n1} to t_l can be calculated by evaluating area integral over ΔCDE, which can be accessed from the Everett surface (Fig. 5.3).

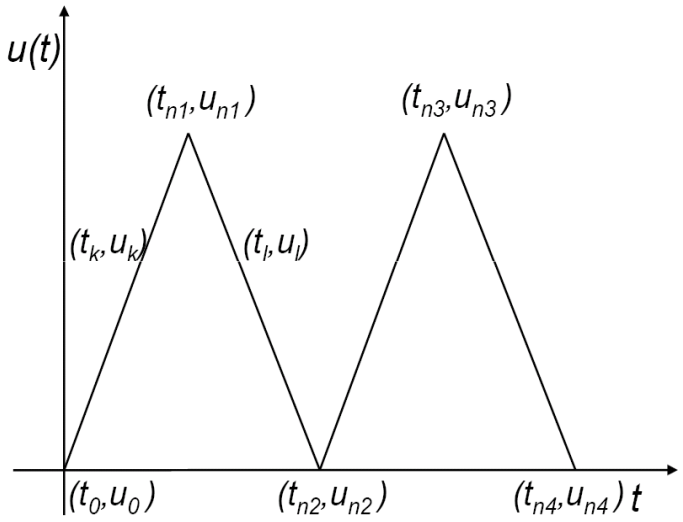

Figure 5.1: Variation of Input with Time

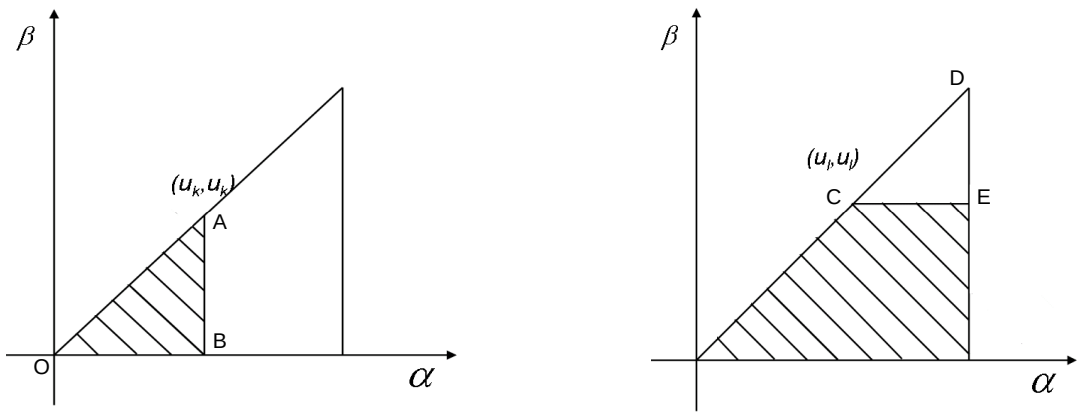

(a) At Time $t = t_k$ (b) At Time $t = t_l$

Figure 5.2: PM Space at Different Time Instants

5.2 Everett Surface Using Both Modified Presiach Hysteresis Operator and Dynamic Relaxation Operator

In case of the modified Preisach operator, we introduce a new Everett type integral that is given as:

$$F_s\left(h_1, h_2\right) = f_{h_2} - f_{h_1} = \begin{cases} \int\limits_{D_1} \mu(\alpha, \beta) d\alpha d\beta & \text{if } h_1 < h_2; \\ \int\limits_{D_1} -\eta(\alpha, \beta)\mu(\alpha, \beta) d\alpha d\beta & \text{if } h_1 > h_2. \end{cases}$$

The modified Everett integral has the same significance for the modified Preisach model as the classical definition has for the Classical Preisach model. However, due to the factor

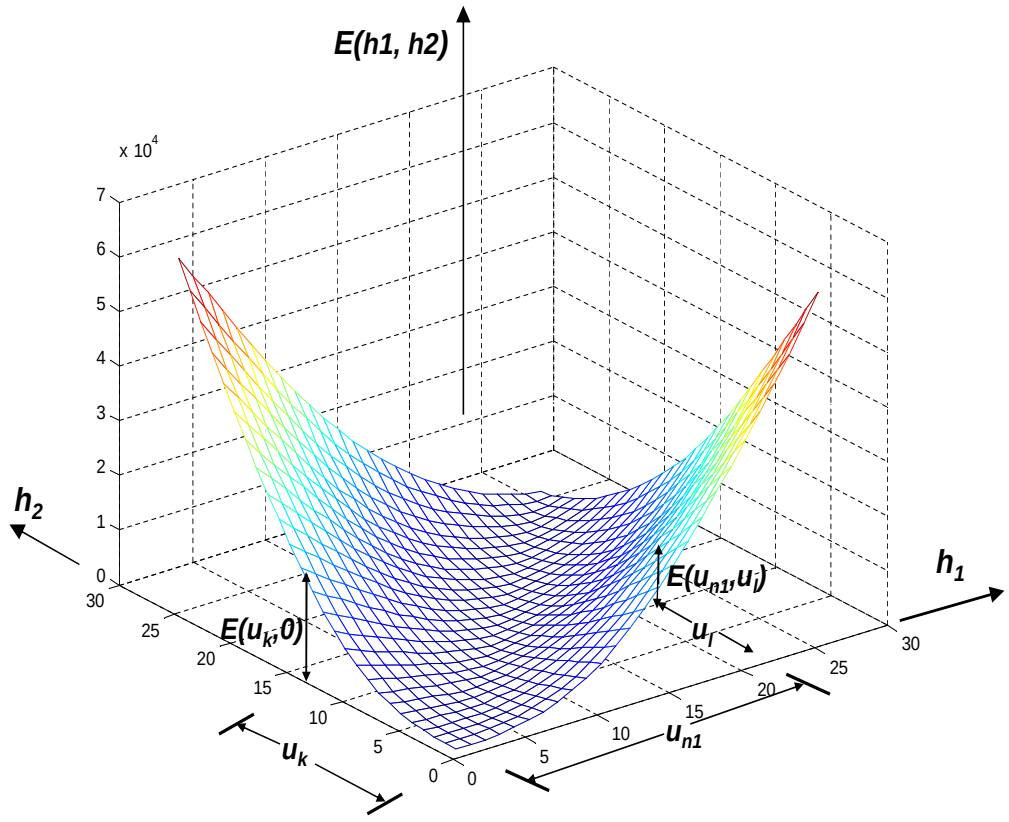

Figure 5.3: Everett Surface

$\eta(\alpha, \beta)$, Everett type surface is no longer symmetric with respect to the line $h_1 = h_2$ for the modified Preisach model developed in this study.

To solve the problem of the compensation of hysteresis and relaxation, we add yet one more term using the dynamic relaxation operators to the expression for the previously defined Everett type integral F_s. Suppose that the current extreme value of input is h_1. Then at time instant t_{k-1}, the value of input is h_{in}. After that, at time instant, t_k, the value of the input rises upto h_2. Using Eq. 4.10 contribution of the dynamic operators upswitched in the

interval $(t_{k-1}, t_k]$ can be written as $\int_{D_2} \sum_{i=1}^{n_\zeta} \sum_{j=1}^{P} a_j \zeta^{d_j} e^{-b_j \left(t - t_{\zeta i}\right)^{c_j}} d\zeta$, where D_2 refers to the region of the dynamic operators which are upswitched in the time interval $(t_{k-1}, t_k]$. If we assume that $\Delta t = t_k - t_{k-1}$ is very small then it can also be written as $\int_{D_2} \sum_{j=1}^{P} a_j \zeta^{d_j} d\zeta$. By adding this quantity to the previously defined Everett type integral, we defined a new quantity $E_1\left(h_1, h_2, h_{in}\right)$ for $h_1 > h_2$.

$$E_1\left(h_1, h_2, h_{in}\right) = f_{h_2} - f_{h_1} = \int\limits_{D_1} \mu(\alpha, \beta) d\alpha d\beta + \int\limits_{D_2} \left(\sum_{j=1}^{P} a_j \zeta^{d_j} \right) d\zeta \tag{5.3}$$

This quantity gives rise to a 3D surface. Input decreases monotonically when $h_1 < h_2$. In that case only the dynamic operators upswitched previously, relax. Apart from that, dynamic operators do not play any other role in this case. Hence, E_2 contains only the contribution from the hysteresis operators.

$$E_2\left(h_1, h_2\right) = f_{h_2} - f_{h_1} = -\int\limits_{D_1} \eta(\alpha, \beta) \mu(\alpha, \beta) d\alpha d\beta \tag{5.4}$$

5.3 Forward Calculation Using Everett Surface

Consider the cyclic input (strain) shown in Fig 5.4a. At time t_k, between t_0 and t_{n1}, the value of the output (electrical resistance) can be written as:

$$f u_i = f_{u_0} + E_1\left(u_0, u_k, u_{k-1}\right) + \int\limits_{T_d} \left(\sum_{i=1}^{n_\zeta} \sum_{j=1}^{P} a_j \zeta^{d_j} e^{-b_j \left(t_k - t_{\zeta i}\right)^{c_j}} \right) d\zeta \tag{5.5}$$

T_d refers to the region of the dynamic operators upswitched in the time interval $(t_0, t_k]$. The current extreme value of input and output are zero. In between times t_{n1} and t_{n2}, when the strain keeps decreasing, the current extreme value of input and output are u_{n1} and f_{n1} respectively. Output at any time t_l between t_{n1} and t_{n2} will be given by:

$$f_{u_l} = f_{u_{n1}} + F_2\left(u_{n1}, u_l\right) + \int\limits_{T_d} \left(\sum_{i=1}^{n_\zeta} \sum_{j=1}^{P} a_j \zeta^{d_j} e^{-b_j (t_l - t_{n1})^{c_j}} \right) d\zeta \tag{5.6}$$

T_d refers to the domain of the dynamic relaxation operators upswitched in $(t_0, t_l]$ and this domain is same as that of the operators upswitched in $(t_0, t_{n1}]$, as none of the dynamic relaxation operators are upswitched when the input decreases.

In this way, value of output can be calculated at any time step by using the surfaces formed by the quantities $F_1\left(h_1, h_2, h_{in}\right)$ and $F_2\left(h_1, h_2\right)$.

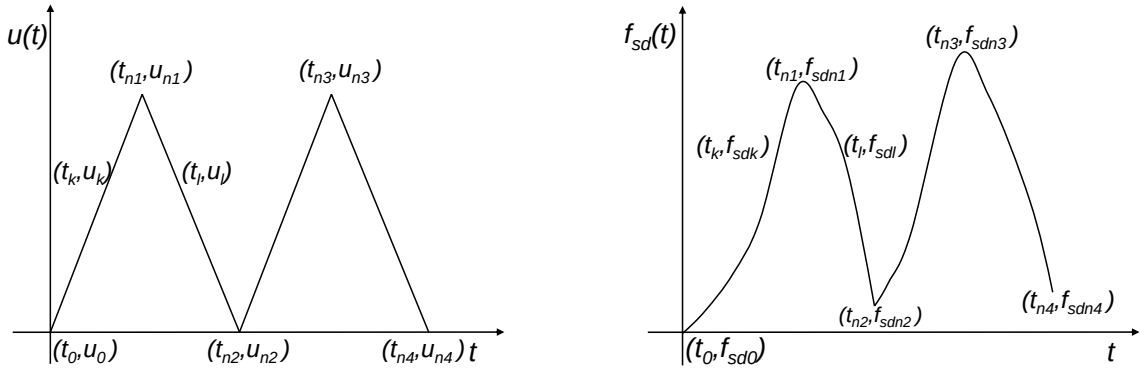

(a) Input Vs. Time

(b) Residual Output Vs. Time

Figure 5.4: Cyclic Input and Residual Part of Output After Compensating for the Relaxation

5.4 Compensation

The compensator works in two stages. At first, it removes the part of the output that results from the relaxation of the dynamic relaxation operators.

At time instant t_k, the contribution from the relaxation of the dynamic operators (upswitched in the interval $(t_0, t_{k-1}]$) to output can be written as:

$$f_{d1} = \int_{T_{d1}} \left(\sum_{i=1}^{n_\alpha} \sum_{j=1}^{P} a_j u^{d_j} e^{-b_j \left(t_k - t_{\zeta i}\right)^{c_j}} \right) d\alpha \tag{5.7}$$

Here, T_{d1} refers to the domain containing the operators upswitched in the interval $(t_0, t_{k-1}]$. This quantity f_{d1} is subtracted from output at each time instant.

The residual part of the output is the result of the static hysteresis and the contribution from the dynamic operators upswitched in $(t_{k-1}, t_k]$. Compensation for this residual part f_{sd} is done by inverse interpolation of the surfaces of $F_1\left(h_1, h_2, h_{in}\right)$ and $F_2\left(h_1, h_2\right)$. At time t_0, both input and output are zero. Input at time $t = t_1$ can be found by inverse interpolation on the surface E_1 by considering $h_1 = 0$, $h_2 = u_1$, $h_{in} = 0$ and $F_1 = f_{sd1} - f_{sd0} = f_{sd1}$. Similarly, at any time step t_k $(t_0 < t_k < t_{n1})$, input can be calculated by considering $h_1 = 0$, $h_2 = u_k$,$h_{in} = u_{k-1}$ and $E_1 = f_{sdk}$. After $t = t_{n1}$, the value of f_{sd} starts decreasing. That means the value of input starts decreasing. So, the current extreme value of input changes to u_{n1} and the surface F_2 needs to be considered for inverse interpolation. At any time step t_l $(t_{n1} < t_l < t_{n2})$, input can be calculated by considering $h_1 = u_{n1}$, $h_2 = u_l$ and $F_2 = f_{sdl} - f_{sdn1}$.

5.5 Results and Discussion

Figure 5.5a shows the comparison of the hysteresis curve obtained from the modified Preisach model with that obtained from experiment. The proposed compensation algorithm was applied to the output (change in electrical resistance) variation obtained from experiment to predict the input (applied strain). Comparison of the strain predicted by the compensator with the actual strain applied during experiment is in Fig. 5.5b. The difference between the applied strain and that obtained from using the compensator to the measured resistance was found to be 4%. The error was calculated by using the expression $\frac{\sum_{i=1}^{i=n}\left(\epsilon_p(t_i)-\epsilon_a(t_i)\right)^2}{\sum_{i=1}^{i=n}\epsilon_a(t_i)^2}$, where ϵ_p means predicted strain, ϵ_a means actual strain and n means number of data points. The comparison shows a good accuracy of the compensator model.

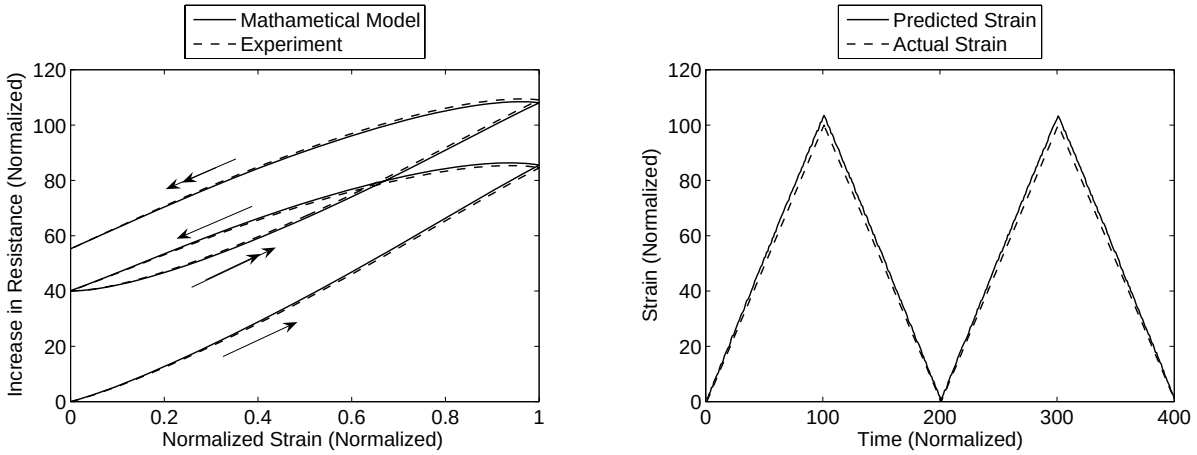

(a) Electrical Resistance Vs. Strain

(b) Strain Vs. Time

Figure 5.5: Comparison of the Results Obtained from Mathematical Model with the Experimental Data

A compensation algorithm for rate dependent dynamic hysteresis has been proposed. Comparison of the input predicted by the compensator with the actual input proves the efficiency of the compensator. Conductive polymer sensor with the proposed compensator put in series

after it can be used for large strain sensing.

Chapter 6

Neuro-fuzzy System

A neuro-fuzzy system is a type of fuzzy system that can be trained by a neural network learning algorithm. Fuzzy logic systems can reason with imprecise information and are good in explaining their decision. But they cannot automatically acquire the rules that they use to make the decisions. On the other hand, neural networks are very good in recognizing patterns although they are not good in explaining how they reach their decisions. Neuro-fuzzy system formed by hybridizing neural network with fuzzy system makes use of the advantages of neural network and fuzzy system. It has the structure of a neural network where different unknown parameters associated with the fuzzy rules are adjusted by adjusting the weights and biases in the neural network using a neural network training algorithm.

6.1 Fuzzy Logic System

A multi-input multi-output (MIMO) fuzzy system does a mapping from a set of input to a set of output using some rules. For the application in structural health monitoring, a damage feature index derived from the response of the structure to an external excitation applied to the system are related to the damage status of the structure using the fuzzy rules.

6.1.1 Fuzzy Set

A fuzzy set is a set containing elements having varying degrees of membership (zero to one) in the set. In a classical or crisp set, the transition for an element between membership and non membership in a given set is abrupt and well-defined. The transition for an element in a universe of discourse containing fuzzy sets can be gradual. Figure 6.1 shows fuzzy sets V_1, V_2, V_3 and V_4 in a universe of discourse X.

6.1.2 Membership Function

Each fuzzy set is associated with a membership function. The membership functions determine the membership values of the elements in each set. Mostly triangular, rectangular, piecewise linear, sigmoidal and Gaussian functions are used as membership functions. Fuzzy logic supports overlapping of membership functions. Triangular functions in Fig. 6.1, are the membership functions.

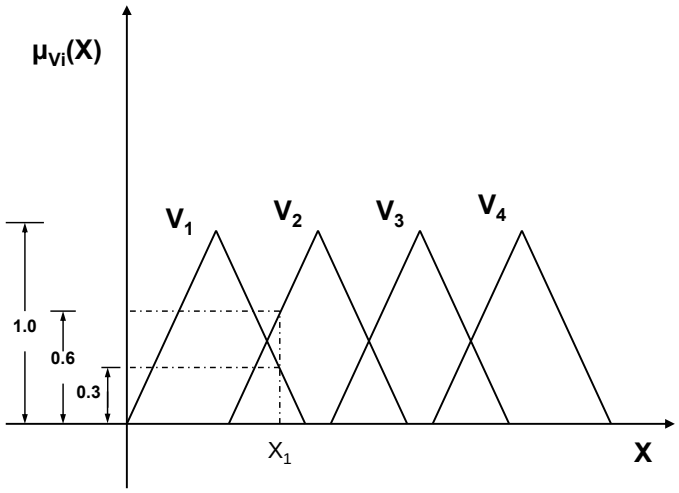

Figure 6.1: Fuzzy Sets and Membership Functions

6.1.3 Fuzzy Rules

Fuzzy rules can be based on relation between different input components or can be based on the similarity with inputs whose outputs are known. For a fuzzy system with m input components (I_1, I_2,..,I_m), a fuzzy rule can be 'IF I_1 is V_1 AND I_2 IS V_2 AND... ANDI_m IS V_m, O IS C_1'. V_1, V_2,..,V_m are fuzzy sets in the universes of discourse of inputs and C_1 is a fuzzy set in the universe of discourse of output. In this way, several rules can be defined to map I_1,I_2,..,I_m to O. The first part of the rule ('IF I_1 is V_1 AND I_2 IS V_2 AND... ANDI_m IS V_m') is called antecedent and the last part of the rule ('O IS C_1') is called the consequent. Mathematically 'AND' operation is denoted by $min(\mu_{F_1}(I_1)\mu_{F_2}(I_2)..\mu_{F_m}(Im))$ and 'OR' operation is denoted by $max(\mu_{F_1}(I_1)\mu_{F_2}(I_2)..\mu_{F_m}(I_m))$, where $\mu_{F_i}(I_i)$ are the membership functions corresponding to sets F_i. The consequence of the rule gives the degree of membership of O in C_i.

The concept of similarity is also often used in fuzzy logic system to define the rules. Here, the similarity of the components of an input with the components of an input in a known input-output set is measured. Henceforth, the sets of known input and output used for similarity measurement will be termed as the reference sets. This measurement of similarity indicates how close the input is with the input in a reference set. In this way, similarities of an input with inputs in different known input-output sets are measured to predict the output from the system. There are several measures of similarity, such as distance based similarity measure, non α cut based similarity measure, α cut based similarity measure, and Koczy's similarity measure. Distance based similarly is mostly used for system identification problems. Detailed discussion on different similarity measures can be found in [69]. Distance of an input I from an input X_i can be defined as:

$$D_i = \sum_{k=1}^{m} w_k \left(I_k - X_{ik}\right)^2 \tag{6.1}$$

Based upon this similarity measurement, a fuzzy set can be defined. The membership value S_i in this set indicates the similarity of I with X_i. Definition of S_i using linear and log-sigmoidal functions are shown in Eqs. 6.2 and 6.3. If the output Y_i, corresponding to the input X_i, lies in the fuzzy set C_1, then corresponding fuzzy rule can be 'IF I IS SIMILAR TO X_i, THEN O is C_1. The value of membership of O in C_1 depends upon the degree of similarity of I with X_i.

$$S_i = \begin{cases} \frac{D_i}{D_{imax}} & \text{if } D_i < D_{imax}; \\ 0 & \text{if } D_i > D_{imax}. \end{cases}$$

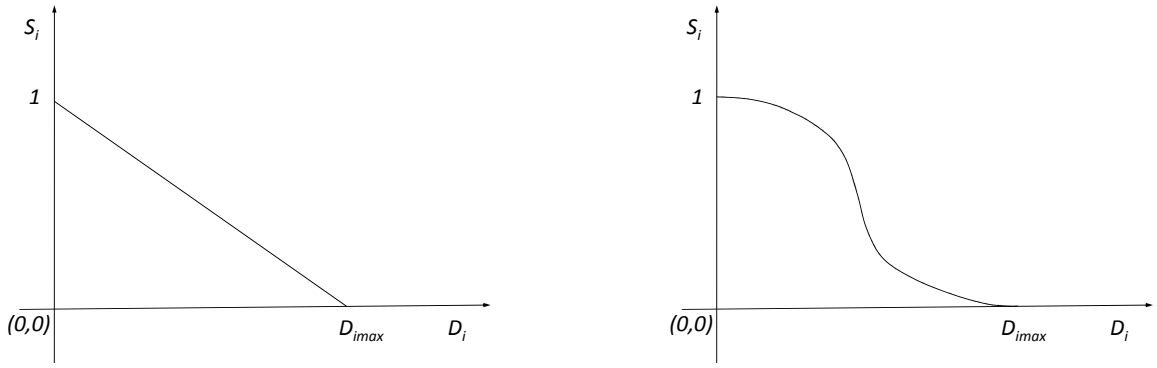

(a) Linear Membership Function (b) Log-Sigmoidal Membership Function

Figure 6.2: Degree of Similarity Vs. Distance

$$S_i = \frac{1}{1 + e^{(-m_1 D_{imax} - m_2 D_i)}} = \frac{1}{1 + e^{(-m_1 D_{imax} - \sqrt{\sum_{k=1}^{n} m_2^2 w_k (I_k - X_{ik})^2})}} \tag{6.3}$$

6.1.4 Defuzzification

Defuzzification is the technique of determining the crisp value of any variable from the degrees of membership of the variable in different fuzzy sets. The crisp value of a variable belonging to n numbers of fuzzy sets is given by

$$u = \frac{\sum_{i=1}^{n} \mu_{V_i} u_{0i}}{\sum_{i=1}^{n} \mu_{V_i}} \tag{6.4}$$

Here, u_{0i} is the value at which the variable can have the maximum degree of membership at fuzzy set V_i. This method is called the centroidal matching method. Among other methods of defuzzification are MOM, SOM and LOM which stand for middle, smallest and largest of

maximum respectively. These maxima based methods consider the fuzzy set in which the variable u has the highest degree of membership. If more than one fuzzy set satisfy this criteria, then among those fuzzy sets the one with middle, smallest or largest value of u_{0i} is chosen and corresponding u_{0i} is taken as the crisp value of the variable. If the variable has the maximum degree of membership at only one set, then u_{0i} for that set is taken as the crisp value of the variable. In that case, MOM, SOM and LOM methods give the same result.

6.1.5 Structure of a Fuzzy Logic System

A fuzzy logic system has four components: 1) Fuzzifier, 2) Inference Engine, 3) Rule Base and 4) Defuzzifier. Structure of a fuzzy logic system is shown in Fig. 6.3. The fuzzifier fuzzifies the input i.e, determines the membership value of each input in each fuzzy set. For example, input X_1 will have membership value 0.3 for small, 0.4 for medium and 1 for large sets according to Fig. 6.3. The rule base contains all the rules. These rules are applied to the inputs by fuzzy inference engine and the degree of activation of the consequence of each rule is calculated. From this, membership values of the output at each of the output fuzzy sets are calculated. The defuzzifier determines the crisp value of the output from these degrees of memberships.

6.2 Artificial Neural Networks

An artificial neural networks (ANN) is a soft computing system based on the operation of biological neurons. It is mostly used for pattern recognition, classification etc. because of

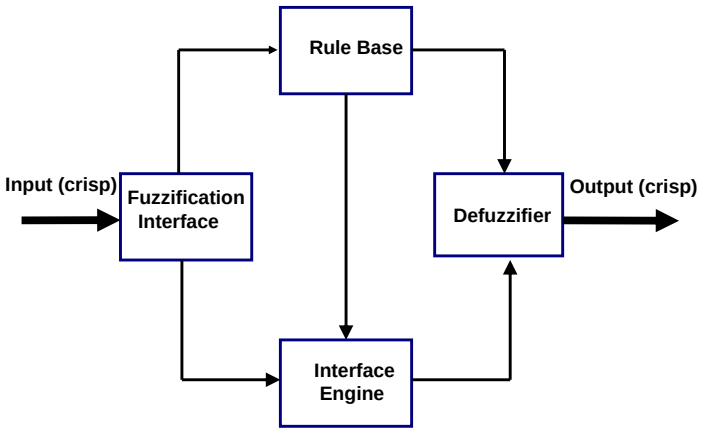

Figure 6.3: Structure of a Fuzzy Logic System

its ability to capture and represent complex input/output relationships. An ANN consists of a number of interconnected processing elements which are called neurons. Like biological neural networks, artificial neural networks acquires knowledge through learning and store knowledge within inter-neuron connection strengths known as synaptic weights. The main advantages associated with ANN are that: i) it can learn from example and perform the required task, ii)it can create its own organization or representation of the information provided to it, iii) it can retain some of its capabilities even with major network damage. An ANN consists of different neurons arranged in layers. The values of connections (weights) between different neurons are adjusted to enable the neuron to perform a specific task.

6.2.1 Structure of a Neural Network

Figure 6.4 shows the structure of a neural network with one layer of neurons. The input layer takes the input $a_j(j = 1, .., 4)$. Each element of the input layer is connected to the

neurons in layer-1. Each connection between an input element p_j and the ith neuron is associated with a weight w_{ij}. Apart from that, the ith neuron may have a bias b_i. Output c_i from the ith neuron is the sum total of weighted inputs and bias ($\sum_{j=1}^{m} w_{ij}p_j + b_i$). Finally, an activation function f_i controls the output from the ith neuron. An activation function can be linear function, step function, sigmoid function etc. Output from each neuron can be written as:

$$O = f_i(\sum_{j=1}^{m} w_{ij}p_j + b_i) \tag{6.5}$$

A neural network can have single or multiple layers. Depending on the pattern of connections between different layers neural networks can be of two types - feedforward networks and recurrent networks. In the feedforward networks, the data flows from input to the output layers, but there is no feedback connection i.e. there is no flow of data from output to the input layer. Recurrent networks have feedback connections. In some cases, they have dynamic properties i.e. the activations undergo relaxation and evolves to a stable state.

6.2.2 Training of Neural Network

Training of neural network involves adjustment of weights and biases so that a given set of input produces a desired set of output. Training procedures can be categorized as supervised training or unsupervised training. In supervised or associative training, a neural network is provided with a set of input-output pairs. In unsupervised or self organization training, a neural network is trained to respond to cluster of patterns within the input. There is no *apriori* set of categories into which the patterns are to be classified; rather the system must

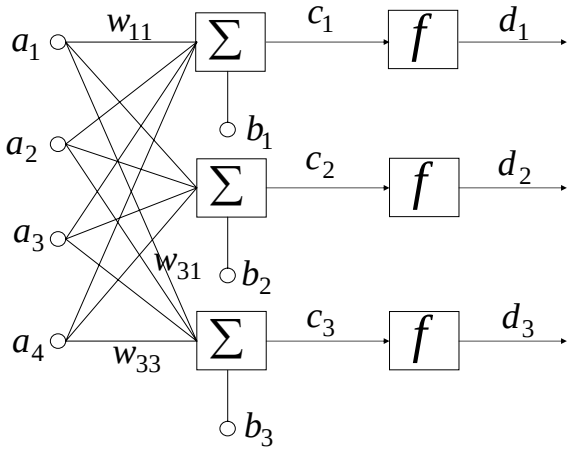

Figure 6.4: Structure of a Single Layered Neural Network

develop its own representation of the input stimuli. Basically, all the training algorithms involving adjustments of weights are variants of the Hebbian learning rule suggested by Hebb in his classic book, *Organization of Behavior* [70]. If the ith neuron in the current layer receives an input x_j from the jth neuron in the previous layer and outputs x_i, then according to the Hebbian rule, the weight of the connection w_{ij} has to be modified by adding Δw_{ij} to it, where Δw_{ij} is given by the following equation

$$\Delta w_{ij} = \gamma x_i x_j \tag{6.6}$$

γ is called the learning rate. In an another rule difference between the actual and desired activation are used as the objective function to be minimized for adjusting the weights.

$$\Delta w_{ij} = \gamma \left(y_i - x_i \right) x_j \tag{6.7}$$

Here, y_i is the desired activation. This is called Widrow-Hoff rule or the Delta rule. In a network consisting of single layer of neurons with linear transfer functions, the objective function is a linear function of the weights and biases. So, the derivatives of the objective function with respect to the weights and biases can be easily calculated. In a network with multiple layers of neurons with non linear transfer functions, calculations of the derivatives of the objective function with the weights and biases become complex. Back propagation algorithm of learning makes the calculation of these derivatives easier. Detailed discussions on the different learning rules can be found in [71, 72, 73].

6.3 Neuro-fuzzy System

In a fuzzy logic system, the input characteristics are mapped into membership functions, membership functions are mapped into output membership functions and output membership functions are mapped into single valued output or decision related to output represented by linguistic variable. If similarity based rules are used then the input characteristics are mapped into degrees of similarity as discussed in subsection 6.1.3. The degrees of similarities are mapped into output. We used similarity based fuzzy rules for our damage detection problem. Here, weights w_k defined in Eq. 6.1 and the parameters associated with definition of degree of similarity D_{imax}, m_1, m_2 defined in Eqs. 6.2 and 6.3 are the unknown values to be determined to define our similarity based fuzzy logic system. These values are determined from a number of sets of known input and output called the training sets. For this purpose, a neuro-fuzzy system has been defined by hybridizing the fuzzy logic system with a neural network so that these unknown parameters can be determined by neural network

training algorithms using the training sets. A generalized structure of a neuro-fuzzy system based on similarity based fuzzy rules is shown in Fig. 6.5.

The neuro fuzzy system accepts input with m components. Its output has one component. The input layer accepts input components $I_i(i = 1, .., m)$ as input. The neuro fuzzy system uses n number of reference sets for similarity measurement. In layer-1, the square of the difference of each component from the corresponding components of the input in ith reference set is calculated. Here, $A_{ij} = (X_{ij} - I_j)^2$. The weighted sums of the squares are calculated in the next layer. Here, $D_i = \sum_{j=1}^{m} w_{1ij} A_{ij}$ is the distance of I from X_i. Now, $D_i(i = 1, .., m)$ is added to bias $b_i(i = 1, .., m)$ and operated by the transfer function which results in degree of similarity S_i of I with ith reference set X_i in the next layer. Choice of the transfer function f depends upon the definition of similarity used (subsection 7.1.3). For example, if the similarity S_i is defined using log-sigmoidal membership function, then log-sigmoidal transfer function will be the best choice. Hence, the weight W_{1ij} in the ith neuron will correspond to the value of $m_2^2 w_j$ and bias b_i will correspond to the values of $m_1 d_{imax}$ in the definition of the similarity given by Eq. 6.3. Thus, by adjusting the weights W_{1ij} and biases $b_i(i = 1, .., n; j = 1, .., m)$ using a neural network training algorithm, the various parameters associated with the fuzzy logic system will be tuned. The output layer has p number of neurons. The ith neuron in the output layer gives the membership value OB_i of the output at the ith fuzzy set in the universe of discourse of output. OB_i is the weighted combination of degrees of similarities calculated in the previous layer. OB_i can be calculated as $OB_i = \sum_{j=1}^{p} w_{2ij} S_j$.

From the available actual output, membership value of each output component in each fuzzy set can be calculated. Let us term the membership value of the actual output in ith fuzzy

set as OB_i^T. Now, this network is trained.

During training $OB_i^T (i = 1, ..., p)$ (p =number of fuzzy sets for output) are considered as the target output. Weights and biases in the layer-1 and the output layer are adjusted by the training process and that completes the definition of the rules. By using this trained network $OB_i (i = 1, ..., p)$ for any input $I (i = 1, .., n)$ can be calculated and then by defuzzifying $OB_i (i = 1, ..., p)$, the output of the system can be determined.

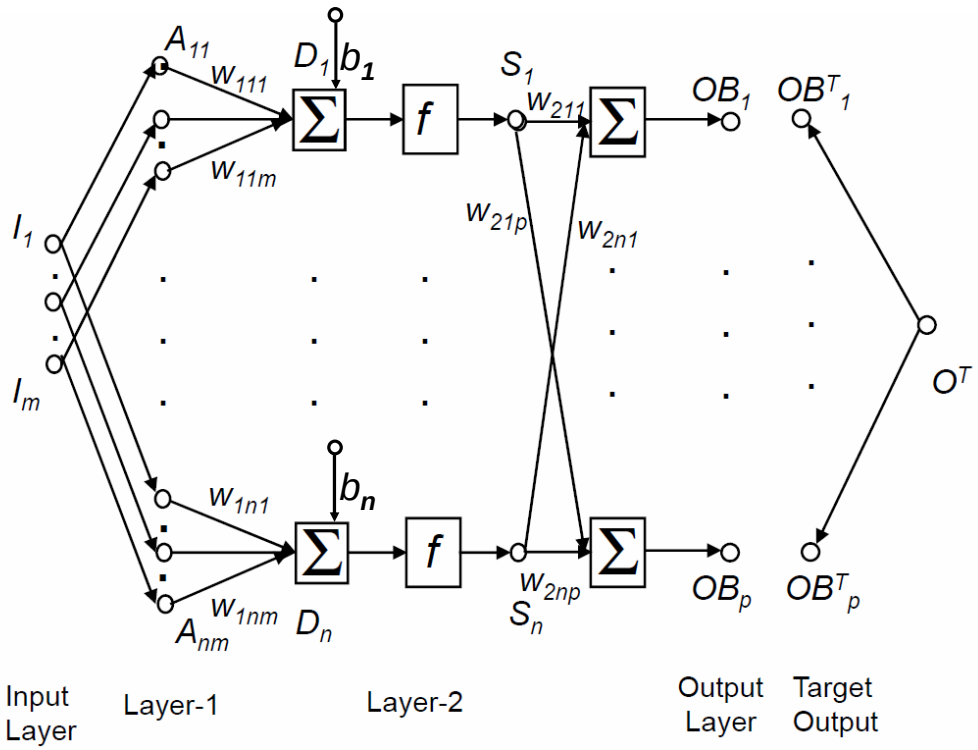

Figure 6.5: Neurofuzzy System

The structure, components and working principle of a neurofuzzy system have all been described. In the next chapter, use of this system for the structural health monitoring will

be shown.

Chapter 7

Damage Detection in a Prestressed Membrane Using a Neuro-Fuzzy System

In this chapter, a neuro-fuzzy based damage detection system has been developed. A prestressed square membrane is taken as our example structure. Damages at the different parts of the structure have been modeled as reduced stiffness. The structure undergoes transverse vibration under the action of a transverse dynamic pressure. The neuro-fuzzy system accepts a wavelet based damage feature index vector as input and gives the damage status of the structure as the output. The wavelet-based damage feature index vector is determined by decomposing the vibration response of the structure using wavelet analysis.

7.1 Description of the Structure

Figure 7.1 shows the square membrane under study. The membrane is made of a linearly homogeneous elastic isotropic material. Its four edges undergo specified amount of initial in plane displacement, Δ. This keeps the membrane under prestress. All the displacement components at all of the four edges of the prestressed membrane are locked. A transverse pressure varying sinusoidally with time is applied to the membrane. The pressure is applied uniformly over the surface of the membrane. The membrane was divided into 16 zones as shown in Fig. 7.12. Each zone can have a certain damage status. Damage in the membrane is modeled as reduced modulus of elasticity. Hence, $P\%$ damage in a certain zone means that the value of the modulus of elasticity E in that zone is $(1 - 0.00P)E_{un}$, where E_{un} means the modululs at the undamaged state. At the undamaged state, all of the 16 zones have the same value of E_{un}.

7.2 Finite Element Analysis of the Structure

Finite element analysis of the prestressed membrane under the transverse dynamic pressure was carried out using ABAQUS. 'ABAQUS CAE' was used for the preprocessing and 'ABAQUS Standard' was used for the solution.

At first, a square membrane section was defined. Using the partition tool, the membrane was divided into 16 zones of equal size. This allows us to define different material properties at different zones. Next, the membrane was discretized into a set of finite elements as shown in Fig. 7.3. Each of the element has four nodes. Displacements along the three directions

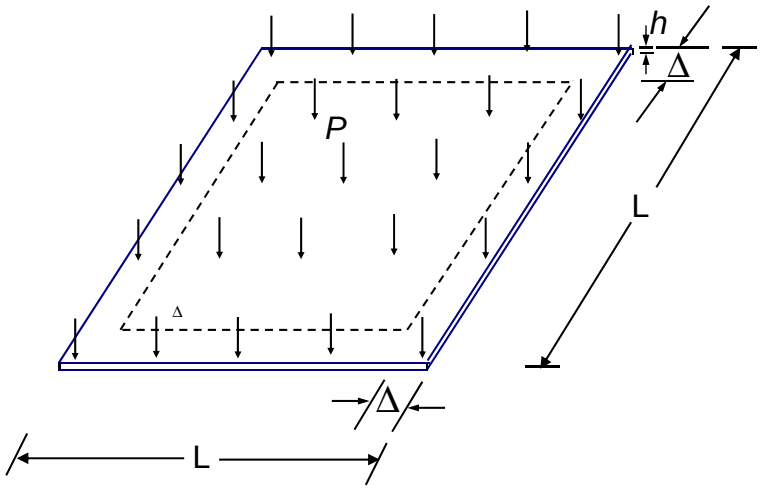

Figure 7.1: Prestressed Membrane Under Study

are taken as the degrees of freedom at each node in the elements. Membrane element 'M3D4' available in the ABAQUS element library was used for that.

Analysis was done in two steps. The first step involved a static analysis. In this step, displacement $\Delta = 0.006m$ at the edges (Fig. 7.1) was prescribed as the boundary conditions. After this step, the length of the edges of the membrane becomes 0.6m and the membrane becomes prestressed. In the next step, a time dependent uniform transverse pressure $P(t)$ was prescribed. This step calculates the time dependent response of the membrane to the time dependent pressure using the implicit time integration scheme. In both the steps, nonlinear strain-displacement relationships were considered.

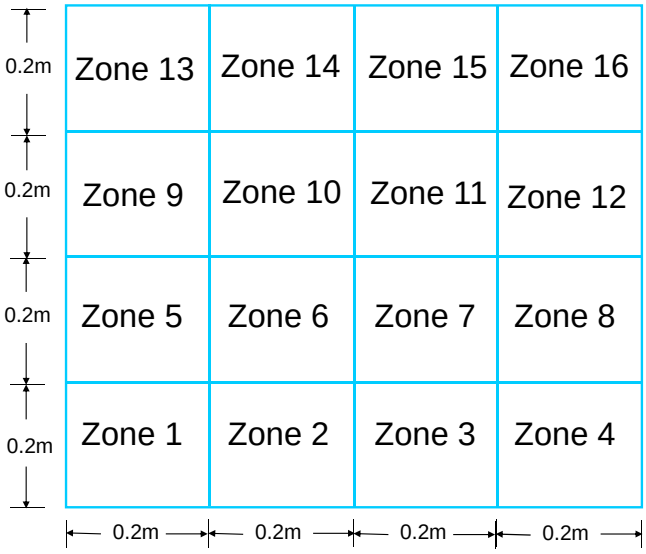

Figure 7.2: 16 Zones in the Prestressed Membrane

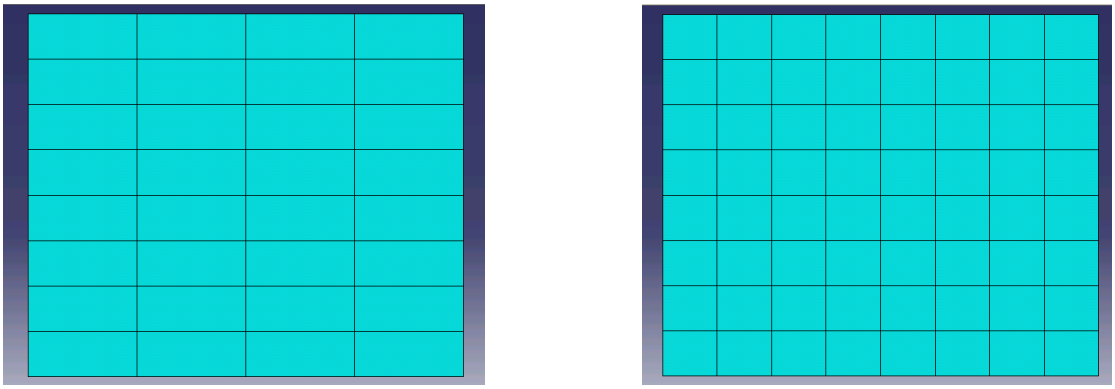

(a) No. of Elements=32

(b) No. of Elements=64

Figure 7.3: Finite Element Meshes for the Prestressed Membrane

7.3 Results of the Finite Element Analysis

Values of different parameters considered in the analysis were as follows:

$L = 0.588\text{m}$

$h = 0.001\text{m}$

$\Delta = 0.006\text{m}$

$P = 10Sin(15.8\pi t)\text{kN/m}^2$

$E = E_{un} = 10\text{MPa}$

$\nu = 0.33$

$\rho = 1100\text{Kg/m}^3$

Here, L is the length of the membrane before prestressing, h is the thickness of the membrane, Δ is the amount displacement at the edges, P is the applied uniform transverse pressure, E is the modulus of elasticity, E_{un} is the modulus of elasticity at the undamaged state, ν is the Poisson's ratio. At first, the simulation was run for a damaged membrane. We assumed a 40% damage in zone 1 (Fig. 7.12). Hence, the value of the modulus of elasticty at zone 2 was considered to be 6 MPa. Rest of the zones were assumed to be undamaged.

The simulation was run thrice using different numbers of elements and different values of the time steps for the implicit numerical integration. Figures 7.4 and 7.5 show the variation of the transverse displacement and normal strain along the Y direction with time at the point (0.2m, 0.2m) in the damaged membrane. In the figures, n means the total number of elements and Δt means the value of the time step used in the finite element analysis. The errors are calculated using the relation $Error = \sum_{i=1}^{N}(S_{ji} - S_{3i})^2/S_{3i}^2$. Here, S_{ji} is the values

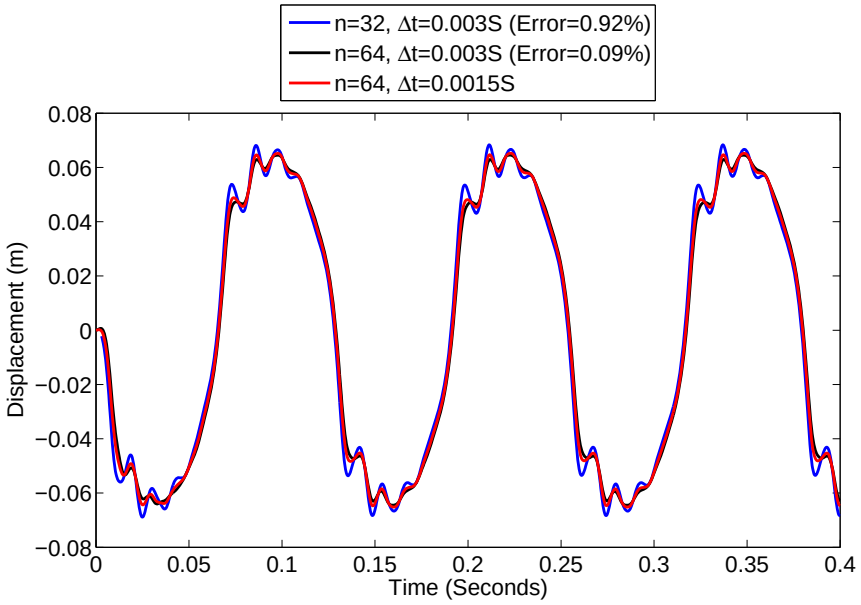

Figure 7.4: Variation of the Transverse Displacement at (0.3m, 0.3m) in the Membrane with 40% Damage at Zone-1

of the quantities (displacement and strain) at the ith data point in the jth data and N is the total number of data points in a data. We can observe little difference in results for the dynamic analysis run using $n = 32$ and $\Delta = 0.0003$; $n = 64$ and $\Delta = 0.0003$ and $n = 64$ and $\Delta = 0.00015$. This proves the convergence of the finite element solution obtained using ABAQUS. Now, the simulation was run for different damage levels at various locations using $n = 32$ and $\Delta = 0.0003$. Figure 7.6 shows the variation of the normal strain along the Y direction at the point (0.2m, 0.2m) in the undamaged membrane.

7.4 Wavelet Based Damage Feature Index

Structural damage enhances and suppresses some components of the vibration response. This results in an energy increase or energy decrease in different components corresponding

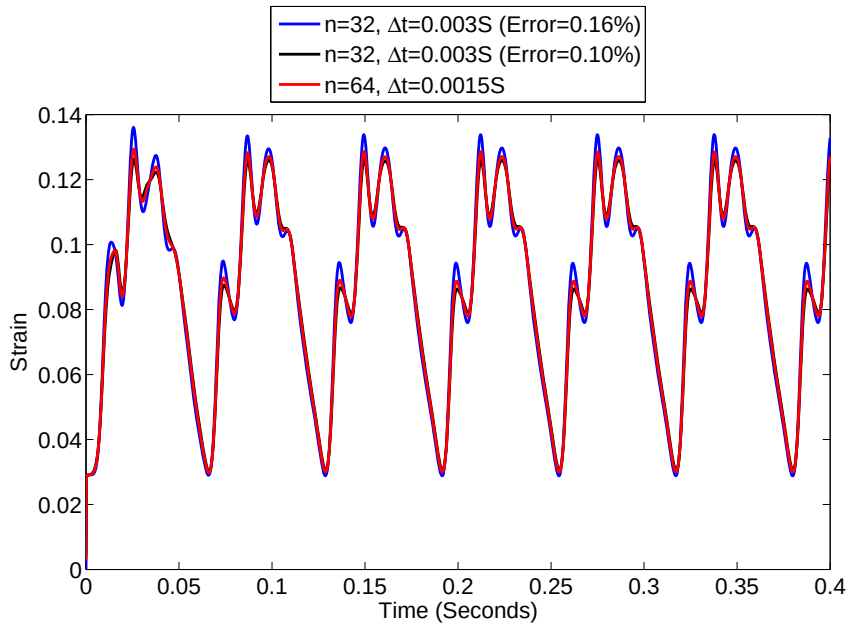

Figure 7.5: Variation of the Transverse Displacement at (0.3m, 0.3m) in the Membrane with 40% Damage at Zone-1

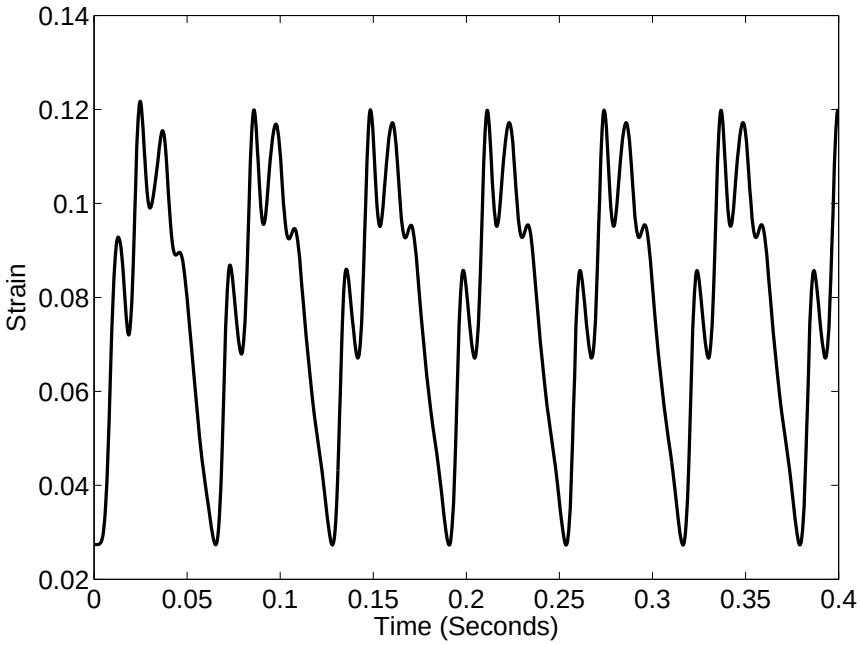

Figure 7.6: Variation of the Normal Strain Along the Y Direction at (0.3m, 0.3m) in the Undamaged Membrane

to different frequency bands of the response. Based on this observation, vibration response of the structure (strain history at the sensor locations) has been decomposed into a few components with different frequency bands and a damage feature index vector has been defined. Components of this array indicate the energy increase or decrease in different components of the vibration response. Wavelet analysis has been used to decompose the vibration response into different components. A detailed description of this can be found in [74, 54]

7.4.1 Wavelets

The kernel or the prototype function used in the wavelet transform is called wavelet. Haar wavelet, Daubechies wavelet, Meyer wavelet, Morlet wavelet etc. are examples of different wavelets. Wavelets show some common properties which are discussed below.

i) Wavelets are compactly supported in both time and frequency domain. ii) Energy content of a wavelet, i.e. its L_2 norm is finite.

$$E = \int_{-\infty}^{\infty} |\psi(t)|^2 dt = \frac{1}{2\pi} \int_{-\infty}^{\infty} |\hat{\psi}(\omega)|^2 d\omega < \infty$$

iii)Wavelets have zero L_1 norm.

$$E = \int_{-\infty}^{\infty} |\psi(t)| dt = 0$$

7.4.2 Continuous wavelet transform

Continuous wavelet transform $W_x(a,b)$ of a signal $x(t)$ can be defined as:

$$W_x(a,b) = \int_{t_1}^{t_2} x(t)\,\psi^*\left(\frac{t-b}{a}\right)dt \tag{7.1}$$

Here a, and b are dilation and translation parameters, respectively. $W_x(a,b)$ are the wavelet coefficients for different values of a and b, and $\psi^*\left(\frac{t-b}{a}\right)$ is the complex conjugate of the translated and dilated version of the mother wavelet $\psi(t)$. The original signal $x(t)$ can be recomposed from the wavelet coefficients using the following equation

$$x(t) = \frac{1}{C_\psi}\int_{-\infty}^{\infty}\int_{-\infty}^{\infty} W_x(a,b)\,\psi\left(\frac{t-b}{a}\right)dadb \tag{7.2}$$

where, $C_\psi = 2\pi\int_0^\infty(|\psi(r)|)^2 dr/r < \infty$ [74, 54].

7.4.3 Wavelet Packet Analysis

One of the main drawbacks associated with the continuous wavelet transform is redundancy in the sampling of a and b. This problem is solved by sampling (a,b) in such a way that the set of discrete wavelets are complete in the space $L^2(R)$, but not redundant. For example, if the sampling lattice is $a = a_0^m, b = nb_0a_0^m$, where m,n, then the scaled and translated version of the wavelet can be written as: $\psi_{mn}(t) = a_0^{-m/2}\psi\left(a_0^{-m}t - nb_0\right)$

If this set is complete in $L^2(R)$ for some choice of $\psi(t), a$, and b, then $\{\psi_{mn}\}$ are called affine

wavelets [74]. A sampling with $a_0 = 2$ and $b_0 = 0.5$ is called the dyadic sampling which is mostly used in the wavelet packet analysis.

The details of wavelet packet analysis (WPA) algorithm can be found in [54, 74]. In wavelet packet analysis, multiresolution analysis of the signal $x(t)$ is performed using wavelets. For that, depending on the wavelet function, a scaling function $\phi(t)$ is defined. The scaled and translated version of the scaling function is defined as:

$\phi_{mn}(t) = a_0^{-m/2}\phi\left(a_0^{-m}t - nb_0\right)$

Now, the signal $x(t)$ can be decomposed into an approximation $Ax(t)$ and a detail $Dx(t)$.

Approximation $Ax(t)$ and the details $Dx(t)$ are the combinations of the translated versions of the scaling function and the wavelet respectively with $m = 1$.

$$Ax(t) = \sum_n A_{1n}\phi_{1n}(t) \tag{7.3}$$

$$Dx(t) = \sum_n D_{1n}\psi_{1n}(t) \tag{7.4}$$

Approximation coefficients A_{1n} and the detail coefficients D_{1n} are obtained by transforming $x(t)$ using the scaling function and the wavelet respectively.

$$A_{1n}(t) = \int_{t_1}^{t_2} x\,(t)\,\phi_{1n}^* dt \tag{7.5}$$

$$D_{1n}(t) = \int_{t_1}^{t_2} x(t)\, \psi_{1n}^{*} dt \tag{7.6}$$

Approximation $Ax(t)$ and detail $Dx(t)$ can further be decomposed into their approximations ($AAx(t)$ and $ADx(t)$) and details ($ADx(t)$ and $DDx(t)$), by following the same procedure using $m = 2$. Multi resolution analysis using wavelet packet transformation can be shown by a binary tree structure (Fig. 7.7). Thus, jth level decomposition of the function $x(t)$ gives rise to 2^j sub-signals.

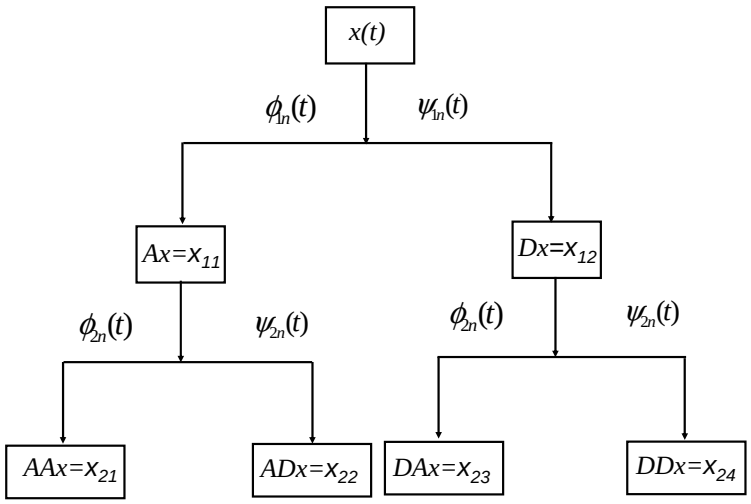

Figure 7.7: Wavelet Packet Tree

7.4.4 Definition of a Damage Feature Index

Let us assume that the vibration response of the structure $x_i(t)$ at the ith measurement location is decomposed into $x_{L,j}^{i}(t)\left(j = 1, 2, ..., 2^{L-1}\right)$, where L is the selected layer number

in the wavelet tree, then the original signal $x(t) = x^i_{0,0}(t)$ can be expressed as:

$$x^i_{0,0}(t) = \sum_{j=1}^{2^{L-1}} x^i_{L,j}(t) \tag{7.7}$$

The energy of the jth sub-signals $x^i_{L,j}(t)$ in the time-interval $[t_1, t_2]$ can be expressed as

$$U_{L,j} = \int_{t_1}^{t_2} |x^i_{L,j}(t)|^2 dt \tag{7.8}$$

Assuming that the energy of the jth order sub-signals of the intact and the damaged structures are $U^0_{L,j}$ and $U^d_{L,j}$ respectively, a non-dimensional damage feature index can be composed as

$$V_d = \{v_1, v_2, ..., v_{2^{L-1}}\}^T \tag{7.9}$$

Here, $v_j = \frac{U^d_{L,j}}{U^0_{L,j}}$.

Generally, different structural damage type, location and severity will match one by one with different damage feature index vectors. Therefore, the element values of different damage feature proxy vector V_d not only indicate the differences between the intact and damaged structures, but also imply the changes in the various states of different structural damages.

7.5 Input and Output

The structure has strain sensors placed at four locations (Fig. 7.12). Wavelet packet analysis up to level-2 is performed on the history of normal strain along Y direction obtained from each sensor and damage feature indices are calculated. Hence, we get four numbers of damage feature indices from the data obtained from each sensor. Combining all the damage feature indices from the four sensors, we get a damage feature index vector with 16 components. This damage feature index vector is taken as the input by our NFS. We used 'Haar' wavelet for our damage detection problem. Figure 7.8 and 7.9 show the scaled and translated versions of the Haar wavelet and the corresponding scaling functions respectively. The four subsignals obtained after the WPA up to level-2 of the strain history (Fig. 7.5) at the sensor location-1 (0.2m, 0.2m) of the prestressed membrane with 40% damage at Zone-1 are shown in Fig. 7.10. Figure 7.11 shows the subsignals obtained after the WPA on the history (Fig. 7.11) at the sensor location-1 of the undamaged prestressed membrane. The damage index vector corresponding to the sensor location-1 for this damaged membrane was $\{1.2038, 0.8491, 0.9788, 3.124\}$. Following this procedure, the damage index vectors were obtained by analyzing the response from all the four sensors locations for membranes with different levels of damage at different locations.

The structure is divided into 16 zones (Fig. 7.12). We formed 16 neuro-fuzzy networks to determine damage in 16 zones. A zone can be undamaged, moderately damaged or highly damaged (Fig. 7.13). These three damage levels are the three fuzzy sets in the universe of discourse of damage level. Output of the NFS has three components. Each component refers to membership value of the damage in the corresponding location in a specific fuzzy set of damage.

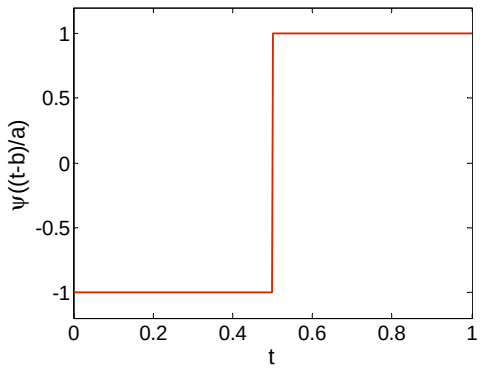

(a) $a = 1, b = 0$

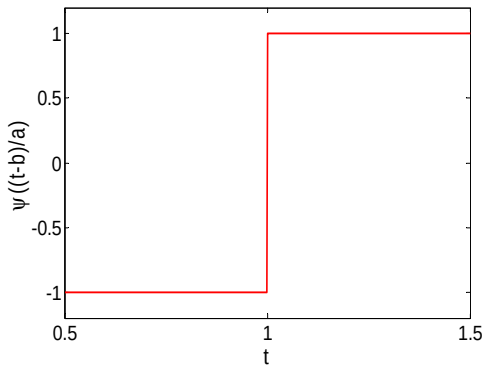

(b) $a = 1, b = 0.5$

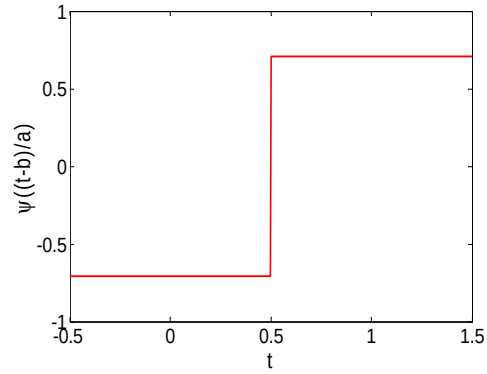

(c) $a = 2, b = 0$

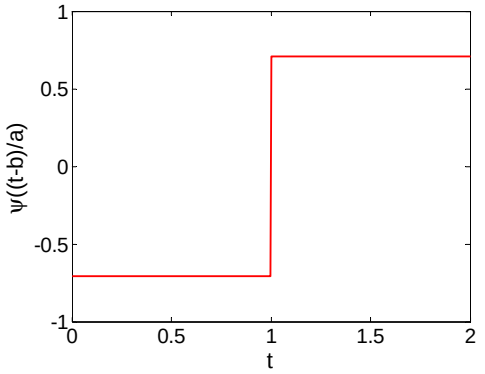

(d) $a = 2, b = 0.5$

Figure 7.8: Haar Wavelet

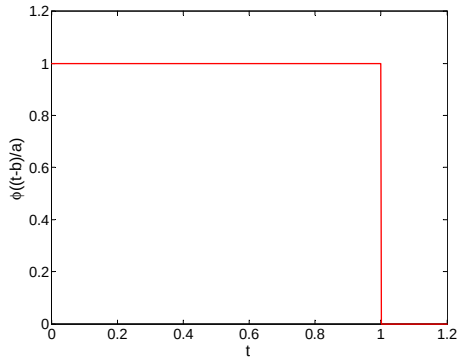

(a) $a = 1, b = 0$

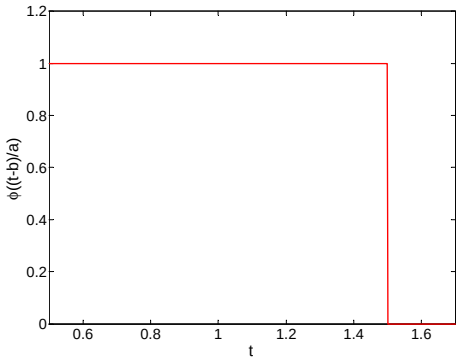

(b) $a = 1, b = 0.5$

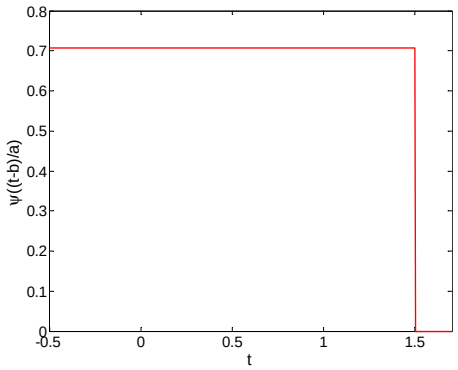

(c) $a = 2, b = 0$

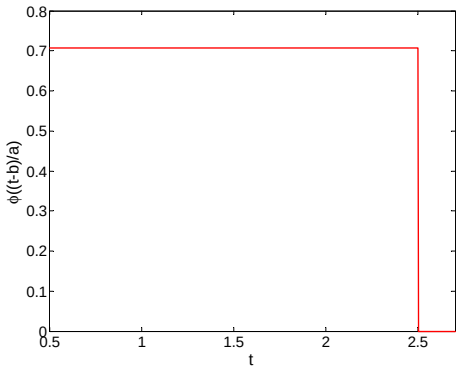

(d) $a = 2, b = 0.5$

Figure 7.9: Scaling function for the 'Haar' Wavelet

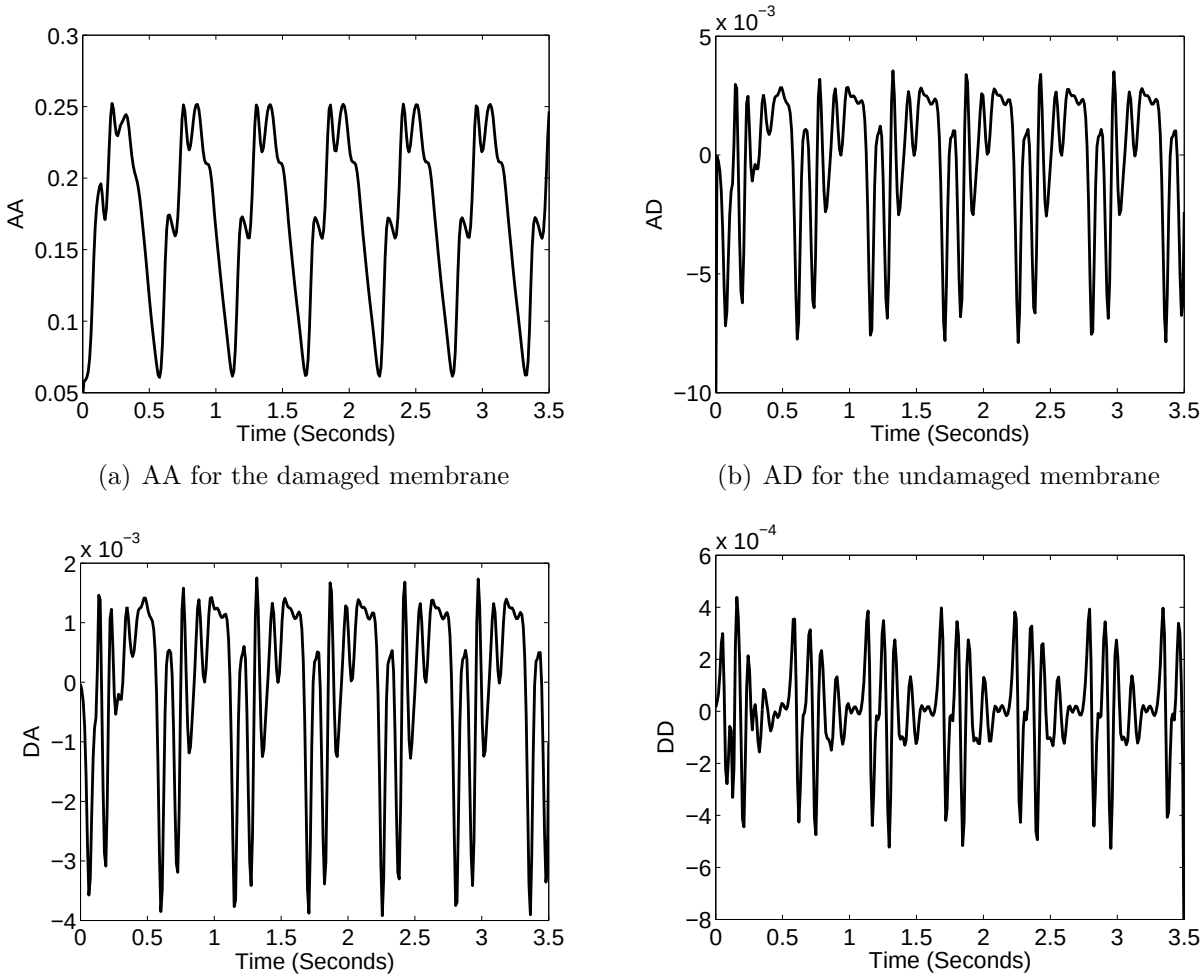

(a) AA for the damaged membrane

(b) AD for the undamaged membrane

(c) DA for the damaged membrane

(d) DD for the undamaged membrane

Figure 7.10: Multiresolution Analysis of the Strain History at (0.2m, 0.2m) in the Damaged Membrane

7.6 Implementation of the Neuro-fuzzy System

We defined 16 neuro-fuzzy systems for damage detection. Each of the neuro-fuzzy system is used to detect damage in one of the 16 zones (Fig. 7.12) in the membrane. Each of the neuro-fuzzy system has the same structure as shown in Fig 6.5. The network was constructed using the 'Neural Network Toolbox' in MATLAB. In the input layer, the neuro-fuzzy system accepts damage feature indices obtained from four sensor locations as input. Each input

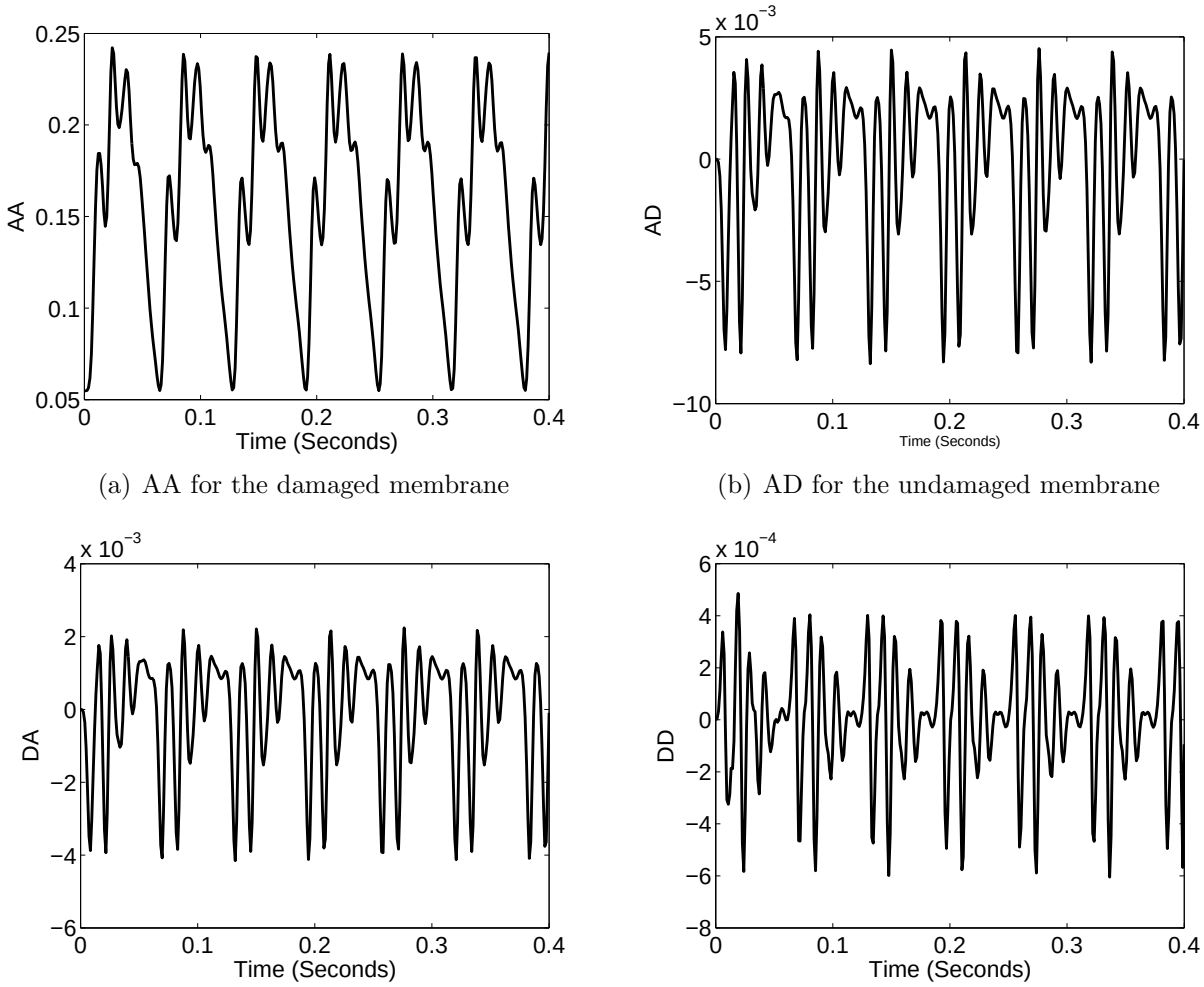

(a) AA for the damaged membrane

(b) AD for the undamaged membrane

(c) DA for the damaged membrane

(d) DD for the undamaged membrane

Figure 7.11: Multiresolution Analysis of the Strain History at (0.2m, 0.2m) in the Undamaged Membrane

I has 16 components. Following the same procedure described in section 7.3, degree of similarity of the input with the inputs in reference sets are obtained in layer-2. In layer-2, 'logsigmoid' transverse function available in the 'Neural Network Toolbox' in MATLAB has been used for all the neurons. The output layer gives the membership values of damage in each fuzzy set of damage status. By centroidal matching technique of defuzzification defined in section 7.1.3, damage status is obtained from the output. In this way, by using 16 neuro-

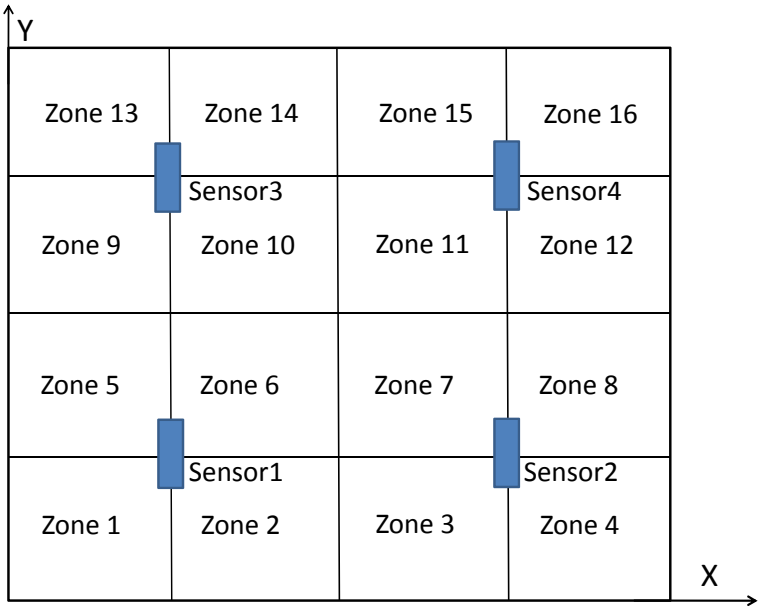

Figure 7.12: Sensor Locations and Damage Zones in the Membrane

fuzzy systems damages at 16 locations are quantified from the strain history obtained at four sensor locations.

7.7 Results and Discussion

At first, we assumed that the membrane can have only one damaged zone at a time. Data for damage status of 0%, 20% and 40% at each zone was taken as both the reference and the training sets to train the neuro-fuzzy network. Rest of the data from simulation was taken as the testing set. Figure 7.15 and Table 7.1 show the comparison of the damage status obtained from the neuro-fuzzy network with the actual damage status. There are two entries for each case in each zone. The upper entry is the actual damage status and the

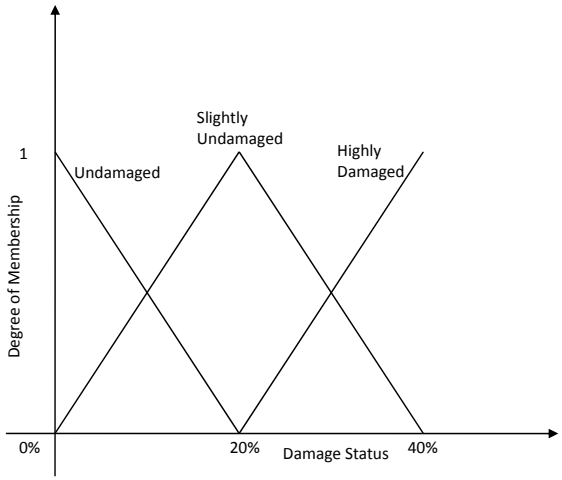

Figure 7.13: Fuzzy Sets for Damage

lower entry is the predicted damage status. It can be observed from Fig. 7.15 and Table 7.1 that the trained neuro-fuzzy can predict damage status for single damage cases properly. But, in case of multiple damage cases its accuracy reduces. This is because of the networks, not being trained with data for multiple damage. Next, an artificial noise was added to the input, i.e. the strain history obtained for different damage cases using the random number generating function 'rand' in MATLAB. Noisy strain history is the summation of the actual history and the random number (in the range [0:0.02]) generated by MATLAB for each time instant. The neuro-fuzzy networks were trained using the noisy data. Figure 7.16 and Table 7.2 show the damage status predicted by the neuro-fuzzy network for noisy data. After this, the networks were trained for multiple damage cases. Table 7.3 shows some of the damage cases in the reference sets. The network was trained using the reference sets. Figure 7.17 and table 7.4 show the damage status predicted when the trained networks were simulated using testing cases for multiple damages. Next, artificial noise was added to strain histories

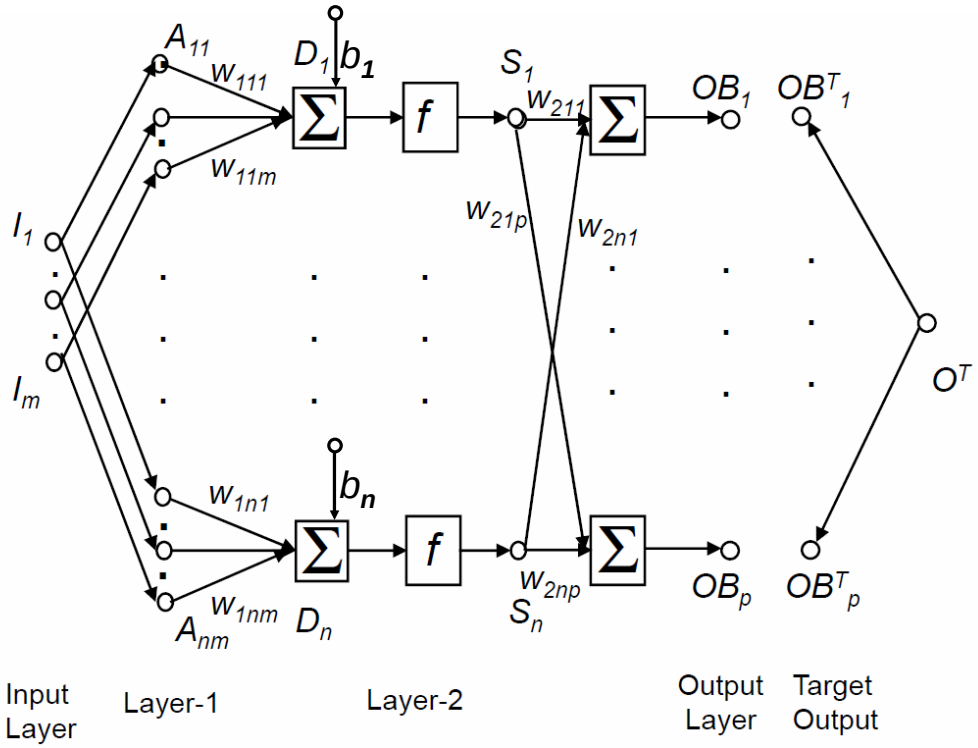

Figure 7.14: A Neurofuzzy System

for both training and testing sets for multiple damage. Figure 7.18 and Table 7.5 show the result from the testing cases for noisy multiple damage data.

From the above results, it can be concluded that the proposed neuro-fuzzy scheme is capable enough to detect damage from vibration response. Fuzzy logic makes it effective in accounting for noise.

0.00 0.01	0.00 0.00	0.00 0.00	0.00 0.00
0.00 0.00	0.00 0.00	0.00 0.03	0.00 0.00
0.00 0.00	0.00 0.03	0.00 0.01	0.00 0.00
20.00 20.00	0.00 0.02	0.00 0.00	0.00 0.02

0.00 0.01	0.00 0.00	0.00 0.04	0.00 0.00
0.00 0.00	0.00 0.02	0.00 0.00	0.00 0.00
0.00 0.00	0.00 0.03	0.00 0.00	0.00 0.06
40.00 39.00	0.00 0.00	0.00 0.00	0.00 0.00

0.00 0.01	0.00 0.25	0.00 0.50	0.00 0.00
0.00 0.00	0.00 0.09	0.00 0.00	0.00 0.01
0.00 0.10	0.00 0.00	0.00 0.20	0.00 0.00
0.00 0.02	20.00 20.00	0.00 0.00	0.00 1.10

0.00 0.01	0.00 0.00	0.00 0.00	0.00 0.00
0.00 0.00	0.00 0.00	0.00 1.20	0.00 0.00
0.00 0.00	0.00 0.00	0.00 0.00	0.00 0.10
0.00 0.00	40.00 40.01	0.00 0.20	0.00 0.02

0.00 0.00	0.00 0.80	0.00 0.00	0.00 0.90
0.00 0.00	0.00 5.28	30.00 28.10	0.00 0.05
0.00 10.23	0.00 0.00	0.00 1.20	0.00 0.00
20.00 16.11	0.00 0.01	40.00 45.10	0.00 1.01

40.00 65.34	0.00 0.444	0.00 2.13	0.00 0.45
0.00 0.00	0.00 6.32	0.00 1.12	0.00 5.65
0.00 0.04	0.00 0.98	0.00 0.67	0.00 7.01
30.00 25.69	0.00 0.01	0.00 0.01	30.00 24.12

Figure 7.15: Comparison of Predicted Damage with Actual Damage Obtained After First Training Without Noise

0.00 1.09	0.00 0.01	0.00 1.90	0.00 0.01
0.00 0.10	0.00 0.90	0.00 0.00	0.00 2.01
0.00 0.21	0.00 3.02	0.00 1.10	0.00 0.59
20.00 20.90	0.00 0.34	0.00 0.00	0.00 0.35

0.00 0.98	0.00 0.03	0.00 0.20	0.00 0.09
0.00 2.01	0.00 0.02	0.00 0.10	0.00 0.09
0.00 0.38	0.00 0.43	0.00 0.01	0.00 0.35
40.00 40.10	0.00 0.01	0.00 0.06	0.00 0.03

0.00 0.84	0.00 0.09	0.00 0.34	0.00 1.09
0.00 1.33	0.00 1.34	0.00 0.05	0.00 1.82
0.00 1.23	0.00 0.05	0.00 0.32	0.00 0.05
0.00 1.00	20.00 18.32	0.00 0.04	0.00 0.56

0.00 0.03	0.00 0.40	0.00 1.00	0.00 0.10
0.00 0.04	0.00 0.40	0.00 1.04	0.00 0.06
0.00 0.02	0.00 0.00	0.00 0.08	0.00 1.43
0.00 0.02	40.00 38.02	0.00 2.09	0.00 0.22

0.00 0.00	0.00 0.00	0.00 3.00	0.00 0.00
0.00 0.00	0.00 0.00	30.00 34.10	0.00 4.00
0.00 11.00	0.00 2.00	0.00 0.00	0.00 6.12
20.00 14.22	0.00 0.20	40.00 34.11	0.00 0.02

40.00 67.93	0.00 0.00	0.00 2.11	0.00 0.00
0.00 0.00	0.00 5.54	0.00 0.44	0.00 3.02
0.00 0.55	0.00 0.43	0.00 2.01	0.00 0.00
30.00 34.17	0.00 0.05	0.00 0.21	30.00 23.15

Figure 7.16: Comparison of Predicted Damage with Actual Damage Obtained After First Training With Noise

0.00 0.00	0.00 0.00	0.00 0.00	0.00 0.00
10.00 11.21	0.00 0.01	0.00 0.00	0.00 0.00
20.00 18.99	0.00 0.01	0.00 0.20	0.00 0.00
40.00 40.01	0.00 0.40	0.00 0.00	0.00 0.00

0.00 0.00	0.00 0.00	0.00 0.00	0.00 0.00
0.00 0.00	0.00 0.00	0.00 0.01	0.00 0.00
10.00 11.21	0.00 0.00	0.00 0.00	20.00 19.21
0.00 0.02	20.00 19.21	0.00 0.01	0.00 0.00

30.00 29.23	0.00 0.01	0.00 0.11	0.00 0.02
0.00 0.02	0.00 0.03	0.00 0.21	40.00 43.11
0.00 0.12	0.00 1.00	0.00 0.00	20.00 19.11
0.00 0.00	0.00 0.11	0.00 0.00	0.00 0.21

0.00 0.02	0.00 0.03	0.00 0.20	0.00 0.00
0.00 0.21	0.00 0.01	0.00 1.01	30.00 28.99
0.00 0.22	0.00 1.23	0.00 0.02	20.00 21.09
0.00 0.00	40.00 38.91	0.00 0.11	0.00 0.01

0.00 0.00	0.00 0.23	0.00 0.00	0.00 0.00
0.00 0.04	37.00 38.12	0.00 0.12	0.00 0.00
15.00 16.13	0.00 1.09	0.00 0.07	0.00 0.04
0.00 1.43	0.00 0.33	20.00 19.32	0.00 0.21

0.00 0.00	0.00 1.11	0.00 1.32	0.00 0.00
0.00 0.20	0.00 0.00	0.00 0.00	10.00 12.32
0.00 0.23	0.00 1.32	20.00 18.23	0.00 0.32
0.00 0.00	20.00 21.23	0.00 0.32	0.00 0.12

Figure 7.17: Comparison of Predicted Damage with Actual Damage Obtained After Second Training Without Noise

0.00 0.12	0.00 0.01	0.00 0.02	0.00 0.00
10.00 8.23	0.00 0.01	0.00 0.00	0.00 0.00
20.00 18.32	0.00 0.65	0.00 1.23	0.00 0.11
40.00 38.62	0.00 0.07	0.00 0.89	0.00 0.00

0.00 0.11	0.00 0.00	0.00 2.21	0.00 0.00
0.00 0.02	0.00 2.12	0.00 0.01	0.00 1.04
10.00 8.14	0.00 0.23	0.00 2.00	20.00 17.99
0.00 0.02	20.00 19.11	0.00 2.12	0.00 0.01

30.00 27.12	0.00 0.13	0.00 0.01	0.00 1. 21
0.00 0.21	0.00 0.22	0.00 0.00	40.00 43.01
0.00 0.56	0.00 0.34	0.00 0.00	20.00 18.01
0.00 0.00	0.00 0.23	0.00 1.78	0.00 1.45

0.00 0.32	0.00 1.21	0.00 0.00	0.00 0.00
0.00 0.22	0.00 0.00	0.00 1.21	30.00 31.45
0.00 0.45	0.00 1.23	0.00 1.04	20.00 22.12
0.00 0.00	40.00 37.21	0.00 0.31	0.00 0.12

0.00 1.09	0.00 0.01	0.00 0.00	0.00 0.00
0.00 0.82	37.00 38.62	0.00 1.19	0.00 0.02
15.00 14.13	0.00 1.41	0.00 0.71	0.00 1.62
0.00 2.00	0.00 0.26	20.00 19.01	0.00 0.31

0.00 0.1	0.00 1.00	0.00 0.00	0.00 2.01
0.00 0.00	0.00 0.00	0.00 0.21	10.00 9.00
0.00 2.01	0.00 0.00	20.00 22.65	0.00 0.11
0.00 0.02	20.00 19.01	0.00 0.31	0.00 0.00

Figure 7.18: Comparison of Predicted Damage with Actual Damage Obtained After Second Training With Noise

Table 7.1: Comparison of Predicted Damage with Actual Damage Obtained After First Training Without Noise

Damage Case No.	Zone1	Zone2	Zone3	Zone4	Zone5	Zone6	Zone7	Zone8	Zone9	Zone10	Zone11	Zone12	Zone13	Zone14	Zone15	Zone16
1.	0.00	0.00	0.00	0.00	0.00	0.00	0.00	0.00	0.00	0.00	0.00	0.00	0.00	0.00	0.00	0.00
	0.00	0.00	0.00	0.00	0.00	0.00	0.00	0.00	0.00	0.00	0.00	0.00	0.00	0.00	0.00	0.00
2.	20.00	0.00	0.00	0.00	0.00	0.00	0.00	0.00	0.00	0.00	0.00	0.00	0.00	0.00	0.00	0.00
	20.00	0.02	0.00	0.02	0.00	0.03	0.01	0.00	0.00	0.00	0.30	0.00	0.01	0.00	0.00	0.00
3.	40.00	0.00	0.00	0.00	0.00	0.00	0.00	0.00	0.00	0.00	0.00	0.00	0.00	0.00	0.00	0.00
	39.00	0.00	0.00	0.00	0.00	0.03	0.00	0.06	0.00	0.02	0.00	0.00	0.00	0.00	0.04	0.00
4.	0.00	20.00	0.00	0.00	0.00	0.00	0.00	0.00	0.00	0.00	0.00	0.00	0.00	0.00	0.00	0.00
	0.02	20.00	0.00	1.10	0.10	0.00	0.20	0.00	0.00	0.09	0.00	0.01	0.00	0.25	0.50	0.00
5.	0.00	40.00	0.00	0.00	0.00	0.00	0.00	0.00	0.00	0.00	0.00	0.00	0.00	0.00	0.00	0.00
	0.00	40.01	0.20	0.02	0.00	0.00	0.00	0.10	0.00	0.00	1.20	0.00	0.01	0.00	0.00	0.00
6.	0.00	0.00	20.00	0.00	0.00	0.00	0.00	0.00	0.00	0.00	0.00	0.00	0.00	0.00	0.00	0.00
	0.00	0.00	20.10	0.02	1.01	0.00	0.00	0.10	0.01	0.20	0.01	0.00	0.01	0.00	0.02	0.00
7.	0.00	0.00	40.00	0.00	0.00	0.00	0.00	0.00	0.00	0.00	0.00	0.00	0.00	0.00	0.00	0.00
	0.00	0.00	39.96	0.00	0.01	0.02	1.00	0.00	0.00	0.09	0.00	0.00	0.00	0.09	0.00	0.00
8.	10.00	0.00	0.00	0.00	0.00	0.00	0.00	0.00	0.00	0.00	0.00	0.00	0.00	0.00	0.00	0.00
	10.11	0.00	0.00	0.20	0.01	0.00	0.00	1.09	0.00	0.03	0.00	0.00	0.00	0.00	0.80	0.00
9.	30.00	0.00	0.00	0.00	0.00	0.00	0.00	0.00	0.00	0.00	0.00	0.00	0.00	0.00	0.00	0.00
	30.10	0.00	0.00	0.02	0.00	0.01	0.00	0.00	0.00	0.00	0.01	0.00	0.00	0.02	0.00	0.00
10.	0.00	9.00	0.00	0.00	0.00	0.00	0.00	0.00	0.00	0.00	0.00	0.00	0.00	0.00	0.00	0.00
	0.00	8.98	0.00	0.00	0.00	0.00	0.00	1.09	0.00	0.00	0.00	0.01	0.00	0.22	0.00	0.00
11.	0.00	35.00	0.00	0.00	0.00	0.00	0.00	0.00	0.00	0.00	0.00	0.00	0.00	0.00	0.00	0.00
	0.00	35.05	0.00	1.03	0.00	1.00	0.00	0.04	0.00	0.00	0.00	1.08	0.00	0.06	0.00	0.00
12.	0.00	0.00	23.00	0.00	0.00	0.00	0.00	0.00	0.00	0.00	0.00	0.00	0.00	0.00	0.00	0.00
	0.00	0.00	24.14	1.00	0.00	0.00	0.00	0.00	0.00	0.01	0.00	0.00	0.00	0.00	0.00	0.00
13.	0.00	0.00	18.00	0.00	0.00	0.00	0.00	0.00	0.00	0.00	0.00	0.00	0.00	0.00	0.00	0.00
	0.00	0.00	18.12	0.00	0.00	0.00	1.03	0.00	0.10	0.00	0.00	0.40	0.00	0.20	0.00	0.20
14.	0.00	0.00	36.00	0.00	0.00	0.00	0.00	0.00	0.00	0.00	0.00	0.00	0.00	0.00	0.00	0.00
	0.00	0.00	35.91	0.01	0.00	0.23	0.05	0.00	0.03	0.00	0.00	0.00	2.02	0.00	0.00	0.00
15.	10.00	0.00	10.00	0.00	0.00	0.00	0.00	0.00	0.00	40.00	0.00	0.00	0.00	0.00	0.00	0.00
	9.75	0.00	4.60	0.00	0.12	0.00	0.00	0.00	0.00	34.29	0.00	9.00	0.00	0.04	2.00	6.00
16.	20.00	0.00	40.00	0.00	0.00	0.00	0.00	0.00	0.00	0.00	30.00	0.00	0.00	0.00	0.00	0.00
	16.11	0.01	45.10	1.01	10.23	0.00	1.20	0.00	0.00	5.28	28.10	0.05	0.00	0.80	0.00	0.90
17.	30.00	0.00	0.00	30.00	0.00	0.00	0.00	0.00	0.00	0.00	0.00	0.00	40.00	0.00	0.00	0.00
	25.69	0.01	0.01	24.12	0.04	0.98	0.67	7.01	0.00	6.32	1.12	5.65	65.34	0.44	2.13	0.45

Table 7.2: Comparison of Predicted Damage with Actual Damage Obtained After First Training With Noise

Damage Case No.	Zone1	Zone2	Zone3	Zone4	Zone5	Zone6	Zone7	Zone8	Zone9	Zone10	Zone11	Zone12	Zone13	Zone14	Zone15	Zone16
1.	0.00	0.00	0.00	0.00	0.00	0.00	0.00	0.00	0.00	0.00	0.00	0.00	0.00	0.00	0.00	0.00
	0.00	0.00	0.00	0.00	0.00	0.00	0.00	0.00	0.00	0.00	0.00	0.00	0.00	0.00	0.00	0.00
2.	20.00	0.00	0.00	0.00	0.00	0.00	0.00	0.00	0.00	0.00	0.00	0.00	0.00	0.00	0.00	0.00
	20.90	0.34	0.00	0.35	0.21	3.02	1.10	0.59	0.10	0.90	0.00	2.01	1.09	0.01	1.90	0.01
3.	40.00	0.00	0.00	0.00	0.00	0.00	0.00	0.00	0.00	0.00	0.00	0.00	0.00	0.00	0.00	0.00
	40.10	1.01	0.61	0.03	0.38	0.43	0.01	0.35	0.01	0.02	0.10	0.00	0.98	0.00	0.20	0.09
4.	0.00	20.00	0.00	0.00	0.00	0.00	0.00	0.00	0.00	0.00	0.00	0.00	0.00	0.00	0.00	0.00
	1.00	18.32	0.04	0.56	1.23	0.05	0.32	0.05	1.33	1.34	0.05	1.82	0.84	0.09	0.34	1.09
5.	0.00	40.00	0.00	0.00	0.00	0.00	0.00	0.00	0.00	0.00	0.00	0.00	0.00	0.00	0.00	0.00
	0.02	38.02	2.09	0.22	0.02	0.00	0.08	1.43	0.04	0.40	1.04	0.06	0.03	0.40	1.00	0.10
6.	0.00	0.00	20.00	0.00	0.00	0.00	0.00	0.00	0.00	0.00	0.00	0.00	0.00	0.00	0.00	0.00
	0.05	0.30	21.02	0.09	1.03	0.32	0.43	0.76	0.10	0.09	0.02	0.97	0.94	0.20	0.20	2.00
7.	0.00	0.00	40.00	0.00	0.00	0.00	0.00	0.00	0.00	0.00	0.00	0.00	0.00	0.00	0.00	0.00
	0.00	0.04	41.95	0.03	0.56	0.23	2.91	5.00	1.01	2.11	0.00	0020	1.00	0.00	2.09	0.00
8.	10.00	0.00	0.00	0.00	0.00	0.00	0.00	0.00	0.00	0.00	0.00	0.00	0.00	0.00	0.00	0.00
	9.12	0.32	3.98	0.55	0.01	0.70	0.03	0.52	0.56	2.09	0.65	0.01	0.00	3.02	2.54	0.00
9.	30.00	0.00	0.00	0.00	0.00	0.00	0.00	0.00	0.00	0.00	0.00	0.00	0.00	0.00	0.00	0.00
	31.12	0.93	0.43	2.43	0.45	0.20	0.45	0.00	0.00	1.09	0.00	1.45	0.02	0.04	0.21	2.04
10.	0.00	9.00	0.00	0.00	0.00	0.00	0.00	0.00	0.00	0.00	0.00	0.00	0.00	0.00	0.00	0.00
	0.54	10.01	0.97	0.06	0.30	0.23	0.11	2.06	0.00	0.02	0.00	3.43	0.34	2.11	0.00	0.00
11.	0.00	35.00	0.00	0.00	0.00	0.00	0.00	0.00	0.00	0.00	0.00	0.00	0.00	0.00	0.00	0.00
	0.00	34.34	0.34	0.98	0.43	8.08	1.09	1.43	0.98	0.45	1.00	2.01	0.45	3.09	0.33	2.98
12.	0.00	0.00	23.00	0.00	0.00	0.00	0.00	0.00	0.00	0.00	0.00	0.00	0.00	0.00	0.00	0.00
	0.02	0.44	21.54	0.45	0.34	2.12	0.09	0.04	0.00	2.00	0.22	1.00	0.03	0.20	0.60	0.02
13.	0.00	0.00	18.00	0.00	0.00	0.00	0.00	0.00	0.00	0.00	0.00	0.00	0.00	0.00	0.00	0.00
	0.00	0.00	18.01	2.01	0.03	0.07	2.98	0.45	3.98	0.45	0.02	0.50	0.90	0.45	0.44	0.67
14.	0.00	0.00	36.00	0.00	0.00	0.00	0.00	0.00	0.00	0.00	0.00	0.00	0.00	0.00	0.00	0.00
	0.00	0.04	37.13	0.70	0.78	0.20	1.04	0.00	3.00	0.50	0.16	0.00	0.65	2.00	1.65	0.45
15.	10.00	0.00	10.00	0.00	0.00	0.00	0.00	0.00	0.00	40.00	0.00	0.00	0.00	0.00	0.00	0.00
	11.34	0.30	8.13	0.54	0.22	0.00	0.01	0.00	0.21	37.22	0.01	6.98	0.10	0.02	7.99	0.00
16.	20.00	0.00	40.00	0.00	0.00	0.00	0.00	0.00	0.00	0.00	30.00	0.00	0.00	0.00	0.00	0.00
	14.22	0.20	34.11	0.02	11.00	2.00	0.00	6.12	0.00	0.00	34.10	4.00	0.00	0.00	3.00	0.00
17.	30.00	0.00	0.00	30.00	0.00	0.00	0.00	0.00	0.00	0.00	0.00	0.00	40.00	0.00	0.00	0.00
	34.17	0.05	0.21	23.15	0.55	0.43	2.01	0.00	0.00	5.54	0.44	3.02	67.93	0.00	2.11	0.00

Table 7.3: Damage Cases in the Reference Set for Second Training

Damage Case No.	Zone1	Zone2	Zone3	Zone4	Zone5	Zone6	Zone7	Zone8	Zone9	Zone10	Zone11	Zone12	Zone13	Zone14	Zone15	Zone16
1.	0.00	0.00	0.00	0.00	0.00	0.00	0.00	0.00	0.00	0.00	0.00	0.00	0.00	0.00	0.00	0.00
2.	20.00	0.00	0.00	0.00	0.00	0.00	0.00	0.00	0.00	0.00	0.00	0.00	0.00	0.00	0.00	0.00
3.	40.00	0.00	0.00	0.00	0.00	0.00	0.00	0.00	0.00	0.00	0.00	0.00	0.00	0.00	0.00	0.00
4.	0.00	20.00	0.00	0.00	0.00	0.00	0.00	0.00	0.00	0.00	0.00	0.00	0.00	0.00	0.00	0.00
5.	0.00	20.00	0.00	0.00	0.00	0.00	0.00	0.00	0.00	0.00	0.00	1.06	0.00	0.09	0.00	0.00
6.	0.00	40.00	0.00	0.00	0.00	0.00	0.00	0.00	0.00	0.00	0.00	0.00	0.00	0.00	0.00	0.00
7.	0.00	0.00	20.00	0.00	0.00	0.00	0.00	0.00	0.00	0.00	0.00	0.00	0.00	0.00	0.00	0.00
8.	0.00	0.00	40.00	0.00	0.00	0.00	0.00	0.00	0.00	0.00	0.00	0.00	0.00	0.00	0.00	0.00
9.	20.00	0.00	40.00	0.00	20.00	0.00	0.00	0.00	0.00	0.00	0.00	0.00	0.00	0.00	0.00	0.00
10.	40.00	0.00	20.00	0.00	40.00	0.00	0.00	0.00	0.00	0.00	0.00	0.00	0.00	0.00	0.00	0.00
11.	20.00	20.00	0.00	0.00	0.00	0.00	0.00	0.00	0.00	40.00	0.00	0.00	0.00	0.00	0.00	0.00
12.	10.00	0.00	20.00	0.00	0.00	0.00	0.00	0.00	40.00	0.00	0.00	0.00	0.00	0.00	0.00	0.00
13.	0.00	10.00	40.00	0.00	0.00	0.00	0.00	20.00	0.00	0.00	0.00	40.00	0.00	0.00	0.00	0.00
14.	20.00	0.00	40.00	0.00	30.00	0.00	0.00	0.00	30.00	0.00	0.00	40.00	0.00	0.00	0.00	0.00
15.	40.00	0.00	40.00	0.00	40.00	0.00	0.00	0.00	0.00	0.00	0.00	0.00	0.00	0.00	0.00	0.00
16.	20.00	20.00	0.00	30.00	0.00	0.00	0.00	0.00	0.00	40.00	0.00	0.00	0.00	0.00	0.00	0.00

Table 7.4: Comparison of Predicted Damage with Actual Damage Obtained After Second Training Without Noise

Damage Case No.	Zone1	Zone2	Zone3	Zone4	Zone5	Zone6	Zone7	Zone8	Zone9	Zone10	Zone11	Zone12	Zone13	Zone14	Zone15	Zone16
1.	40.00	0.00	0.00	0.00	20.00	0.00	0.00	0.00	10.00	0.00	0.00	0.00	0.00	0.00	0.00	0.00
	40.01	0.40	0.00	0.00	18.99	0.01	0.20	0.00	11.21	0.01	0.00	0.00	0.00	0.00	0.00	0.00
2.	0.00	20.00	0.00	0.00	10.00	0.00	0.00	20.00	0.00	0.00	0.00	0.00	0.00	0.00	0.00	0.00
	0.02	19.21	0.01	0.00	11.21	0.00	0.00	19.21	0.00	0.00	0.01	0.00	0.00	0.00	0.00	0.00
3.	0.00	0.00	0.00	0.00	0.00	0.00	0.00	20.00	0.00	0.00	0.00	40.00	30.00	0.00	0.00	0.00
	0.00	0.11	0.00	0.21	0.12	1.00	0.00	19.11	0.02	0.03	0.21	43.11	29.23	0.01	0.11	0.02
4.	0.00	40.00	0.00	0.00	0.00	0.00	0.00	20.00	0.00	0.00	0.00	30.00	0.00	0.00	0.00	0.00
	0.00	38.91	0.11	0.01	0.22	1.23	0.02	21.09	0.21	0.01	1.01	28.99	0.02	0.03	0.20	0.00
5.	0.00	0.00	20.00	0.00	15.00	0.00	0.00	0.00	0.00	37.00	0.00	0.00	0.00	0.00	0.00	0.00
	1.43	0.33	19.32	0.21	16.13	1.09	0.07	0.04	0.04	38.12	0.12	0.00	0.00	0.23	0.00	0.00
6.	0.00	20.00	0.00	0.00	0.00	0.00	20.00	0.00	0.00	0.00	0.00	10.00	0.00	0.00	0.00	0.00
	0.00	21.23	0.32	0.12	0.23	1.32	18.23	0.32	0.20	0.00	0.00	12.32	0.00	1.11	1.32	0.00
7.	20.00	0.00	40.00	0.00	20.00	0.00	0.00	0.00	0.00	0.00	0.00	0.00	0.00	0.00	0.00	0.00
	19.22	0.22	39.32	0.02	21.09	0.79	0.12	0.09	1.32	0.32	0.01	1.43	0.43	1.08	0.06	0.98
8.	40.00	0.00	20.00	0.00	40.00	0.00	0.00	0.00	0.00	40.00	0.00	0.00	0.00	0.00	0.00	0.00
	40.11	0.33	19.12	0.22	36.98	0.32	1.32	0.01	1.02	37.90	0.00	1.09	0.00	91.00	0.00	1.09

Table 7.5: Comparison of Predicted Damage with Actual Damage Obtained After Second Training With Noise

Damage Case No.	Zone1	Zone2	Zone3	Zone4	Zone5	Zone6	Zone7	Zone8	Zone9	Zone10	Zone11	Zone12	Zone13	Zone14	Zone15	Zone16
1.	40.00	0.00	0.00	0.00	20.00	0.00	0.00	0.00	10.00	0.00	0.00	0.00	0.00	0.00	0.00	0.00
	38.62	0.07	0.89	0.00	18.32	0.65	1.23	0.11	8.23	0.01	0.00	0.00	0.12	0.01	0.02	0.00
2.	0.00	20.00	0.00	0.00	10.00	0.00	0.00	20.00	0.00	0.00	0.00	0.00	0.00	0.00	0.00	0.00
	0.00	19.11	2.12	0.01	8.14	0.23	2.00	17.99	0.02	2.12	0.01	1.04	0.11	0.00	2.21	0.00
3.	0.00	0.00	0.00	0.00	0.00	0.00	0.00	20.00	0.00	0.00	0.00	40.00	30.00	0.00	0.00	0.00
	0.00	0.23	1.78	1.45	0.56	0.34	0.00	18.01	0.21	0.22	0.00	43.01	27.12	0.13	0.01	1.21
4.	0.00	40.00	0.00	0.00	0.00	0.00	0.00	20.00	0.00	0.00	0.00	30.00	0.00	0.00	0.00	0.00
	0.00	37.21	0.31	0.12	0.45	1.23	1.04	22.12	0.22	0.00	1.21	31.45	0.32	1.21	0.00	0.00
5.	0.00	0.00	20.00	0.00	15.00	0.00	0.00	0.00	0.00	37.00	0.00	0.00	0.00	0.00	0.00	0.00
	2.00	0.26	19.01	0.31	14.13	1.41	0.71	1.62	0.82	38.62	1.19	0.02	1.09	0.01	0.00	0.00
6.	0.00	20.00	0.00	0.00	0.00	0.00	20.00	0.00	0.00	0.00	0.00	10.00	0.00	0.00	0.00	0.00
	0.02	19.01	0.31	0.00	2.01	0.00	22.65	0.11	0.00	0.00	0.21	9.00	0.1	1.00	0.00	2.01
7.	20.00	0.00	40.00	0.00	20.00	0.00	0.00	0.00	0.00	0.00	0.00	0.00	0.00	0.00	0.00	0.00
	22.43	0.11	42.23	0.11	19.12	0.33	0.90	0.01	1.42	0.00	0.00	0.00	0.00	0.00	0.00	2.01
8.	40.00	0.00	20.00	0.00	40.00	0.00	0.00	0.00	0.00	40.00	0.00	0.00	0.00	0.00	0.00	0.00
	39.01	0.21	18.02	1.23	38.01	2.21	0.00	3.00	0.01	38.02	0.0	1.01	0.00	0.01	0.00	0.00

Chapter 8

Summary and Conclusions

1. Experiments have been carried out on conductive polymer to investigate its feasibility for using it as a large strain sensor. Phenomena of hysteresis and relaxation have been observed in the variation of electrical resistance with strain in conductive polymer.

2. Two mathematical models based on some modifications on fractional calculus and Preisach approaches have been developed to model the change in the electrical resistance due to applied time dependent strain in the conductive polymer. Numerical results show a good agreement between the results obtained from the mathematical model and the experimental result.

3. A compensator based on the modified Preisach model has been developed to compensate the effect of hysteresis and relaxation. The efficiency of the compensator has been discussed by comparison with experimental results.

4. Finite element simulation using ABAUS has been run to find out the response of a prestressed membrane with different damage levels at different locations.

4. A damage detection algorithm has been developed using artificial neural network and fuzzy logic. Using the simulated data obtained from the finite element analysis, the neuro-fuzzy system has been trained. It has been shown that the trained neuro-fuzzy system can detect damage from the dynamic response of the structure and can account for noise to a great extent.

The large strain sensor with compensator, mathematical model of the structure and the neurofuzzy system can be used to develop an integrated structural health monitoring system for gossamer structures.

Bibliography

[1] Jenkins, C. H. M., "Gossamer spacecraft: membrane and inflatable structures technology for space applications", *Edited by Christopher H. M. Jenkins*, 2002.

[2] Moffitt, R. D., Bland, S. C., Sunny, M. R., and Kapania, R. K., "Sensor technologies for direct health monitoring of tires", *Encyclopedia of Structural Health Monitoring, John Wiley Sons, Ltd., ISBN: 978-0-470-05822-0*, 2008.

[3] Hammerand, D. C., and Kapania, R. K., "Thermo-viscoelastic analysis of composite structures using a triangular flat shell element", *AIAA Journal,* **37**(2), 1999, pp. 238–247.

[4] Hammerand, D. C., and Kapania, R. K., "Geometrically nonlinear shell element for hygrothermorheologically simple linear viscoelastic composites", *AIAA Journal,* **38**(12), 2000, pp. 2305–2319.

[5] Heymans, N., "Constitutive equations for polymer viscoelasticity derived from hierarchical models in cases of failure of time-temperature superposition", *Signal Processing,* **83**(11), November, 2003, pp. 2345–2357 .

[6] Flandin, L., Brechet, Y., and Cavaille, J., -Y., "Electrically conductive polymer

nanocomposites as deformation sensors", *Composites Science and Technology,* **61**, July, 2000, pp. 895–901 .

[7] Knite, M., Teteris, V., Kiploka, A., and Kaupuzs, J., "Polyisoprene-carbon black nanocomposites as tensile strain and pressure sensor materials", *Sensors and Actuators A:Physical,* **110**,(1-3), February, 2004, pp. 142–149 .

[8] Rekhviashvili, S., "Non-steady-state electrical conduction of polymers in the model with fractional integro-differentiation", *Physics of the Solid State,* **49**(8), August, 2007, pp. 1598–1602.

[9] Viswamurthy, S. R., and Ganguli, R., "Modeling and compensation of piezoceramic actuator hysteresis for helicopter vibration control", *Sensors and Actuators A: Physical,* **135**(2), April, 2007, pp. 801–810.

[10] Oldham, K. B., and Spanier, J., "The Fractional Calculus", *Academic New York Presss,* **86** 10, October, 1974, pp. 2592–2601.

[11] Chang, T., "Seismic response of structures with added viscoelastic dampers", PhD Thesis, Virginia Polytechnic Institute and State University, Blacksburg, VA, September, 2003. See also URL `http://scholar.lib.vt.edu.`

[12] Euler, L., "De progressionibus transcendentibus, sev quarum termini generales algebraice dari nequent", *Commentarii Academiae Scientiarum Imperialis Scientiarum Petropolitanae,* **5**, 1738, pp. 38–57.

[13] Lacroix, S. L., "Traite du calcul dierentiel et du calcul integral", *2nd ed., Courcier, Paris,* 1819, pp. 409–410.

[14] Hardy, G. H., "On some properties of integrals of fractional order", *Messenger Math,* **47**, 1917, pp. 145–150.

[15] Osler, T. J., "Leibniz rule for fractional derivatives generalized and an application to infinite series", *SIAM Journal of Applied Mathematics,* **18**(3), 1970, pp. 658–674.

[16] Nutting, P. G., "A new general law of deformation", *Journal of the Franklin Institute,* **191**, 1921, pp. 679–685.

[17] Bagley, R. L., and Torvik, P. J., "A theoretical basis for the application of fractional calculus to viscoelasticity", *Journal of Rheology,* **27(3)**, 1983, pp. 201–210.

[18] Gemant, A., "A method of analyzing experimental results obtained from elasto-viscous bodies", *Physics,* **7**(8), 1936, pp. 311–317.

[19] Scott-Blair, G. W., and Reiner, M., "The rheological law underlying the Nutting equation", *Applied Science Research,* **A2**, 1950, pp. 225–234.

[20] Belavine, V. A., Nigmatullin, R. S., Miroshnikov, A. I., and Lutskaya, N. K., "Fractional differentiation of oscillographic polarograms by means of an electrochemical two-terminal network", *Kazan. Aviation Institute. Transactions,* **5**, 1964, pp. 144–145.

[21] Bagley, R. L., and Torvik, P. J., "Fractional calculus - a different approach to the analysis of viscoelastically damped structures", *AIAA Journal,* **21**(5), 1983, May, pp. 2305–2319.

[22] Bagley, R. L., and Torvik, P. J., "On the fractional calculus model of viscoelastic behavior", *Journal of Rheology,* **30**, February, 1986, pp. 133–155.

[23] de Espindola, J. J., da Silva Neto, J. M., and Lopes, E. M. O., "A generalised fractional derivative approach to viscoelastic material properties measurement", *Applied Mathematics and Computation,* **164**(2), 2005, pp. 493–506.

[24] Horr, A. M., and Schmidt, L. C., "A fractional-spectral method for vibration of damped space structures", *Engineering Structures,,* **18**, December, 1996, pp. 947–956.

[25] Davis, G., Kohandel, M., Sivaloganathan, S., and Tenti, G., "The constitutive properties of the brain paraenchyma: Part 2. fractional derivative approach", *Medical Engineering Physics,* **28**, June, 2006, pp. 455–459.

[26] Preisach, F. Z., "Uber die magnetische nachwirkung", *Z. Phys.,* **94**, 1935, pp. 277–302.

[27] Everett, D. H., and Whitton, W. I., "A general approach to hysteresis", *Transactions of the Faraday Society,* **48**, 1952, pp. 749-757.

[28] Cornejo, D. R., and Missell, F. P., "Application of the Preisach model to nanocrystalline magnets", *Journal of Magnetism and Magnetic Materials,* **203**, 1999, pp. 41–45.

[29] Roshko, R. M., and Huo, D. L., "A Preisach characterization of the barkhausen spectrum of a canonical ferromagnet $SrRuO3$", *Physica B,* **306**(1), December, 2001, pp. 246–250.

[30] Vandenbossche, L., Dupr, L., and Melkebeek, J., "Preisach-based magnetic evaluation of fatigue damage progression", *Journal of Magnetism and Magnetic Materials*, April, 2005, pp. 486–489.

[31] Schiffer, A., and Ivanyi, A., "Preisach distribution function approximation with

wavelet interpolation technique", *Physica B: Condensed Matter,* **372**(1), February, 2006, pp. 101–105.

[32] Yunhe, Y., Xhengchu, X., En-Bing, L., and Nagi, N., "Analytic and experimental studies of a wavelet identification of Preisach model of hysteresis", *Journal of Magnetism and Magnetic Materials,* **208**, January, 2000, pp. 255–263.

[33] Mayergoyz, I., "Mathematical models of hysteresis and their applications", *Elsevier Series in Electromagnetism,* **208**, January, 2003, pp. 255–263.

[34] Natalea, C., Velardib, F., and Visonec, C., "Identification and compensation of Preisach hysteresis models for magnetostrictive actuators", *Physica B.,* **306**, 2001, pp. 161–165.

[35] Venkataraman R., Krishnaprasad, P., S., and Visonec, C., "A novel algorithm for the inversion of the Preisach operator", *Proceedings of SPIE ,* **3984**, 2003, pp. 5281–5293.

[36] Davino, D., Natale, C., Pirozzi, S., and Visone, C., "A fast compensation algorithm for real-time control of magnetostrictive actuators", *Journal of Magnetism and Magnetic Materials,* **290-291**(2), 2005, pp. 1351–1354.

[37] Cavallo, A., Davino, D., Maria, G., D., Natale, C., Pirozzi, S., and Visone, C. "Hysteresis compensation of smart actuators under variable stress conditions", *Physica B: Condensed Matter,* **403**(2-3), February, 2008, pp. 261–265.

[38] Galinaitis, W., S., and Rogers, R., C., "Compensation for hysteresis using bivariate Preisach models", *Proceedings of SPIE - Smart Structures and Materials,* **3039**, 1997, pp. 538–547.

[39] Tan, X., Venkataraman, R., and Krishnaprasad, P., S., "Control of hysteresis: theory and experimental results", *Proceedings of SPIE - Smart Structures and Materials: Modeling, Signal Processing and Control in Smart Structures,* **4326**, 2001, pp. 101–112.

[40] Janocha, H., and Kuhnen, K., "Real-time compensation of hysteresis and creep in piezoelectric actuators", *Sensors and actuators A: Physical,* **79**, 2000, pp. 83–89.

[41] Changhai, R., and Lining, S., "Hysteresis and creep compensation for piezoelectric actuator in open-loop operation", *Sensors and actuators A: Physical,* **122**, 2005, pp. 124–130.

[42] Law, S. S., Li, X. Y., Zhu, X. Q., and Chan, S. L., "Structural damage detection from wavelet packet sensitivity ", *Engineering Structures,* **27**(9), 2005, pp. 1339–1348.

[43] Pandey, A. K., Biswas, M., and Samman, M. M., "Damage detection from changes in curvature mode shapes ", *3rd Slovakian-Hungarian Joint Symposium on Applied Machine Intelligence, Herl'any, Slovakia,* January, 1991, pp. 256–276, 1991.

[44] Hamey, C. K., Qiao, P., and Song, G., "Experimental damage identification of carbon/epoxy composite beams using curvature mode shapes", *Structural Health Monitoring,* **3**(4), December, 2004, pp. 333–353.

[45] Unger, J. F., Teughels, A., and Roeck, G. D., "System identification and damage detection of a prestressed concrete beam", *Journal of Structural Engineering ,* **132**(11), March, 1995, pp. 1691–1698.

[46] Farrar, C. R., and Jauregui, D. A., "Comparative study of damage identification

algorithms applied to a bridge. I. Experiment", *Smart Materials and Structures* , **7**, 1995, pp. 704–719.

[47] Farrar, C. R., and Jauregui, D. A., "Comparative study of damage identification algorithms applied to a bridge: II. Numerical study", *Smart Materials and Structures* , **7**, 1995, pp. 720–731.

[48] Sun, Z., and Chang, C. C., "Structural damage assessment based on wavelet packet transform", *Journal of Structural Engineering* , **128**(10), March, 2002, pp. 1354–1361.

[49] Loewke, K., Meyer, D., Starr, A., and Nemat-Nasser, S., "Structural Health Monitoring Using FFT ", *Smart Structures and Materials: Sensor and Smart Structures Technology for Civil, Mechanical and Aerospace Systems. Proceedings of SPIE,* **5765**, 2005, pp. 931–935.

[50] Raghavan, A., and Cesnik, C. E. S., "Finite-dimensional Piezoelectric transducer modeling for guided wave based structural health monitroing ", *Smart Materials and Structures,* **14**, 2005, pp. 1448–1461.

[51] Pawar, P. M., Reddy, K. V., and Ganguli, R., "Damage detection in beams using spatial Fourier analysis and neural networks", *Smart Materials and Structures,* **18**, 2007, pp. 347–369.

[52] Kim, H., and Melhem, H., "Damage detection of structures by wavelet analysis ", *Engineering Structures,* **26**(3), 2004, pp. 347–362.

[53] Turkoglu, I., Arslan, A., and Ilkay, E., "An intelligent system for diagnosis of the heart

valve diseases with wavelet packet neural networks", *Engineering Structures,* **33**(4), 2003, pp. 319–331.

[54] Yam, L. H., Yan, Y. J., and Jiang, J. S., "Vibration-based damage detection for composite structures using wavelet transform and neural network identification", *Composite Structures,* **60**(4), 2003, pp. 403–412.

[55] Kim, Y. Y., and Kapania, R. K., "Neural networks for inverse problems in damage identification and optical imaging using orthogonal arrays and principal component analysis", *AIAA Journal,* **44**(7), 2006, pp. 1628–1634, 2004.

[56] Chakraborty, D., "Artificial neural network based delamination prediction in laminated composites", *Materials and Design,* **26**(1), January, 2005, pp. 1–7.

[57] Mahapatra, D. R., Suresh, S., Omkar, S. N., and Gopalakrishnan, S., "Estimation of degraded laminate composite properties using acoustic wave propagation model and a reduction-prediction network", *Engineering Computations,* **22**(7-8), 2005, pp. 849–876.

[58] Oberholster, A. J., and Heyns, P. S., "On-line fan blade damage detection using neural networks", *Mechanical Systems and Signal Processing,* **20**(1), 2006, pp. 78–93.

[59] Liang, Y. C., and Hwu, C., "On-line identification of holes/cracks in composite structures", *Smart Materials and Structures,* **10**(4), 2001, pp. 599–609.

[60] Rao, M. A., Srinivas, J., and Murthy, B. S. N., "Damage detection in vibrating bodies using genetic algorithms", *Computers and Structures,* **82**(11-12), 2004, pp. 963–968.

[61] Nag, A., Mahapatra, D., R., and Gopalakrishnan, S., "Identification of delamination in

composite beams using spectral estimation and a genetic algorithm", *Smart Materials and Structures,* **11**(6), 2002, pp. 899–908.

[62] Yang, Z. L., Liu, G. R., and Lam, K. Y., "An inverse procedure for crack detection using integral strain measured by optical fibers", *Smart Materials and Structures,* **11**(1), 2002, pp. 72–78.

[63] Sawyer, J.P., and Rao, S.S., "Structural damage detection and identification using fuzzy logic", *AIAA Journal,* **38**(12), 2000, pp. 2328–35.

[64] Soh, C. K., and Bhalla, S., "Calibration of piezo-impedance transducers for strength prediction and damage assessment of concrete", *Smart Materials and Structures,* **14**, 2005, pp. 671–684.

[65] Ramu, S. A., and Johnson, V. T., "Damage assessment of composite structures using fuzzy logic integrated neural-network approach", *Computers and Structures,* **57**(3), 1995, pp. 491–502.

[66] Pawar, P., M., and Ganguli, R., "Genetic fuzzy system for damage detection in beams and helicopter rotor blades ", *Computer Methods in Applied Mechanics and Engineering,* **192**(16-18), 2003, pp. 2031–2057.

[67] Schmidt, A., and Gaul, L., "On the numerical evaluation of frational derivatives in multi-degree-of-freedom systems", *Signal Processing,* **86**(10), October, 2006, pp. 2592–2601.

[68] Guyer, R. A., McCall, K., R., Boitnott, G., M., Hilbcrt Jr., L., B., and Plona, T., J.,

"Quantitative implementation of Preisach-Mayergoyz space to find static and dynamic moduli of rock", *Journal of Geophysical Research,* **102** (B3), January, 1997, pp. 255–263.

[69] Johanyak, Z., C., and Kovacs, S., "Distance based similarity measures of fuzzy sets", *3rd Slovakian-Hungarian Joint Symposium on Applied Machine Intelligence, Herl'any, Slovakia,* January 21-22, pp. 256–276, 2005.

[70] Hebb, D., O., "The organization of behavior : a neuropsychological theory", *Mahwah, N.J.: L. Erlbaum Associates.*, 2002.

[71] Hagan, M. T., Demuth,H. B., and Beale, M., "Neural network design", *PWS Publishing Company*, 1996.

[72] Livingstone, D. J., "Artificial neural networks : methods and applications", *Totowa; New Jersey: Humana Press*, 2008.

[73] Galushkin, A. I., "Neural networks theory", *Berlin ; New York: Springer*, 2007.

[74] Mallat, S., G., "A wavelet tour of signal processing", *San Diego: Academic Press*, 1999.